

Department of Physics and Astronomy

Heidelberg University

Master thesis

in Physics

submitted by

Sebastian Dittmeier

born in Aschaffenburg

2013

Development of a Test Setup for a 60 GHz Wireless Transceiver for the ATLAS Tracker Readout

This Master thesis has been carried out by Sebastian Dittmeier

at the

Physikalisches Institut Heidelberg

under the supervision of

Prof. Dr. André Schöning

Entwicklung eines Testaufbaus für einen kabellosen 60 GHz Sende-Empfänger zur Auslese des ATLAS Spurdetektors:

Das geplante Upgrade des Large Hadron Collider (LHC) zum High-Luminosity-LHC (HL-LHC) wird dazu führen, dass die Ereignisrate und die Zahl der sich überlagernden Ereignisse weiter ansteigen. Um wichtige und relevante Ereignisse herauszufiltern soll der Silizium-Streifendetektor zur ersten Stufe der Trigger-Entscheidung des ATLAS Experiments beitragen. Dafür ist ein Auslesesystem erforderlich, welches insgesamt bis zu 100 Tbps übertragen kann. Die kabellose Datenübertragung bei 60 GHz stellt eine neue Technologie dar, die die benötigte Datenrate von 5 Gbps pro Link bietet und dabei sparsam ist in Bezug auf Material und Leistungsaufnahme.

Ein strahlenharter Prototyp eines 60 GHz Sendeempfängers ist derzeit in Entwicklung. In dieser Arbeit wurde ein Referenzsystem aufgebaut, das aus einem Bitfehlertest mit einem kommerziellen 60 GHz-Chip besteht. Dabei wurden Fehlerraten kleiner als 10^{-14} bei 1.76 Gbps erzielt. Die Qualität der Datenübertragung wurde für verschiedene Datenraten getestet. Ein großes Problem bei der kabellosen Übertragung innerhalb des Detektors könnte das Übersprechen darstellen. In dieser Arbeit werden Ansätze zu dessen Reduzierung vorgestellt. Dabei wurden unter anderem richtende Hornantennen aus aluminisierter Kapton-Folie, Reflektionen dämpfender Graphit-Schaum, linear polarisierte Wellen sowie die parallele Übertragung auf unterschiedlichen Kanälen untersucht. Durch eine Kombination dieser Hilfsmittel lässt sich das Übersprechen deutlich unterdrücken, sodass eine stabile kabellose Datenübertragung im Detektor realisierbar erscheint.

Development of a Test Setup for a 60 GHz Wireless Transceiver for the ATLAS Tracker Readout:

The planned upgrade of the Large Hadron Collider (LHC) to the High Luminosity - LHC (HL-LHC) will lead to a further increase of the event rate and pile-up events. In order to filter out important and relevant events the silicon strip detector should be part of the first level trigger decision of the ATLAS experiment. To accomplish this a readout system is necessary which can transfer up to 100 Tbps. Wireless data transfer at 60 GHz is a new technology that can handle the needed bandwidth of 5 Gbps per link. Besides, it has low material budget and power consumption.

Currently a prototype of a radiation-hard 60 GHz transceiver is under development. In this work a reference system has been developed which consists of a bit error rate test using a commercial 60 GHz chipset. Bit error rates smaller than 10^{-14} at 1.76 Gbps were achieved. The quality of the data transfer was analysed for different data rates. Crosstalk induced by the wireless data transfer inside the detector might be a big issue. This thesis presents several approaches that address the reduction of crosstalk. In doing so, directing horn antennas made from aluminised Kapton foil, graphite foam to attenuate reflections, linearly polarised waves as well as the parallel communication through different frequency channels has been investigated. A combination of these tools can reduce crosstalk clearly such that a stable wireless data transfer inside the detector seems feasible.

Contents

1	Introduction	1
2	Basics	5
2.1	Electromagnetic Waves	5
2.1.1	Maxwell's Equations	5
2.1.2	Plane Waves	6
2.1.3	Reflection and Transmission at Plane Surfaces	7
2.1.4	Absorption and Transmission Through a Layer of Finite Thickness	8
2.2	Properties of Antennas	9
2.3	The Decibel Unit System	10
2.4	Data Transmission and Modulation Schemes	11
2.4.1	On-Off-Keying	12
2.4.2	IQ Modulation	12
2.4.3	Minimum Shift Keying	13
3	Wireless Readout at 60 GHz for the ATLAS Tracker Upgrade	15
3.1	The ATLAS Detector	15
3.2	The Phase-II Upgrade of the ATLAS Detector	17
3.3	Wireless Data Transfer at 60 GHz	18
3.4	A Wireless Tracker Readout System	18
3.5	A New 60 GHz Transceiver	19
3.5.1	Functional Design	20
3.5.2	Technology	21
4	The Reference Transceivers	23
4.1	Gotmic 60 GHz Transmitter and Receiver	23
4.2	Hittite 60 GHz Transceiver Evaluation Kit	26
5	Crosstalk Suppression	29
5.1	Characterisation of Antennas	29
5.1.1	Near Field Effects	31
5.1.2	Polar Pattern Simulation of Horn Antennas	32
5.1.3	Directivity Measurements	35
5.1.4	Analysis of Polarisation	38
5.2	Microwave Properties of Detector Material	42
5.2.1	Reflectivity and Transmittance of Aluminised Kapton and Silicon	44
5.2.2	Reflectivity and Transmittance of Graphite Foam	49
5.2.3	Insertion Loss and Inhomogeneity of Graphite Foam	53
5.3	Crosstalk Measurements	55

5.3.1	Direct Crosstalk from Neighbouring Transmitter	55
5.3.2	Multi-Path Crosstalk Between Reflecting Layers	57
5.3.3	Signal to Noise at the Output of the Receiver	61
6	Wireless Data Transfer	65
6.1	Bit Error Rate Test	65
6.1.1	Implementation	65
6.1.2	Setup	68
6.1.3	Measurements and Results	71
6.2	Analysing Fast Data Links with Eye Diagrams	72
6.2.1	Eye Diagram Basics	72
6.2.2	Eye Diagram Measurements	74
6.2.3	Jitter, Noise and Bit Error Rate Analysis	77
6.3	Direct Crosstalk Measurements	83
6.3.1	Symbol Error Rates with Antennas and Foam	83
6.3.2	Symbol Error Rates with Channeling	85
7	Discussion and Outlook	89
	Appendix	93
A	BERT running on Stratix V FPGA	93
B	Monitoring of Power Supplies	97
C	Lists	99
C.1	List of Figures	99
C.2	List of Tables	102
	Bibliography	103
	Acknowledgments	107

1 Introduction

Most of the recent discoveries in particle physics have been made at large accelerator facilities. Collider experiments like the LHC¹ at CERN² provide extremely high collision rates that allow for studies of very rare particle physics' processes. Large particle detectors are used to measure the final state of these events. Signals caused by the particles are converted into data that allow for reconstruction and further analysis. To achieve a precise event reconstruction the detector experiments offer high spatial, timing, momentum and energy resolution. Different sub-detectors are necessary to provide all of the desired information. In order to filter relevant events from the background a trigger system is necessary. It typically combines information from different sub-detectors and consists of several levels implemented in hard- and software. The high event rate and the high resolution result in high data rates produced by the detectors. A limiting factor for the amount of data that can be transferred from a detector is the bandwidth of the individual readout links.

ATLAS is one of the big multi-purpose detector experiments at the LHC. It consists of the inner detector, the calorimeters and the muon spectrometer. Currently only the latter two contribute to the Level-1 hardware trigger decision [1]. The inner detector is formed by a silicon pixel detector, a silicon microstrip tracker and a transition radiation detector. The strip tracker features a high spatial resolution of 17 μm perpendicular to the strips per layer [2]. It produces data at high rates which are transferred via more than 8000 optical links at 40 Mbps each [3]. So far, information from the tracker is not included in the first level trigger decision of the ATLAS experiment. But this might change in the future after the upgrade of the LHC to the HL-LHC³ which is targeted to take place between 2022 and 2023 [4]. The detectors have to be upgraded to meet the challenges of increased event rate and pile-up induced by an increasing luminosity by a factor of 10. For this upgrade, which is called the Phase-II upgrade of the ATLAS experiment, the inner detector is intended to be replaced by an all-silicon detector [5]. Moreover a new Level-0/Level-1 hardware trigger architecture is proposed. Because of the expected high track density the tracking detector should be included in the hardware trigger decision forming a Level-1 track trigger. Like that the selectivity of the trigger decision could be increased. The baseline design proposes a region of interest (RoI) based approach [5], though a self-seeded design is another option for the track trigger. Both options require a new fast readout system for the tracker whereas the latter would need more bandwidth.

¹LHC = Large Hadron Collider

²CERN = Conseil Européen pour la Recherche Nucléaire (fr.) - European Organization for Nuclear Research

³HL-LHC = High Luminosity Large Hadron Collider

The upgrades of accelerator and detector will result in higher data rates. Up to now particle detectors are readout using either optical or wired links. However, in the last few years a new wireless technology operating at 60 GHz has been developed which offers a large bandwidth, small form factor and a high integration level [6]. Data rates of several Gbps can be transferred with a single link [6]. As Brenner et al. suggested in [7] the 60 GHz wireless might be an opportunity to implement a fast readout system for the ATLAS tracking detector that can facilitate the implementation of a track trigger. For this application a new 60 GHz wireless transceiver ASIC⁴ is under development at Heidelberg University. The first prototype aims at a data rate of 3.5 Gbps and uses the 130 nm SiGe HBT BiCMOS 8HP technology [8].

The aim of the work described here is the generation of a test bench for the chip under development. Different aspects of wireless data transmission are examined. In addition crosstalk has been analysed because this might be a major issue for a wireless readout system in tracking detectors [7].

Chapter 2 presents the basics for this work. It covers electromagnetic waves that are the foundation of wireless data transmission. Properties of antennas and the decibel unit system are presented. Moreover an introduction into data transmission and modulation schemes is given. Chapter 3 introduces the ATLAS tracking detector and the Phase-II upgrade. The idea of a wireless readout implementation is presented. The functional design of the transceiver prototype under development as well as the chosen technology are presented.

Afterwards the performed experiments are described in detail. Chapter 4 presents the commercially available 60 GHz transmitter and receiver chipsets that were used for the verification of the test setup and for the performed experiments. Chapter 5 addresses the problem of crosstalk in a wireless tracking detector readout. Different approaches to this problem are given. First, measurements of the directivity of a small size horn antenna made from aluminised Kapton⁵ foil are presented. Antennas are a very promising candidate to suppress crosstalk in the first place by focusing the radio beam. Secondly, the separation of orthogonally, linearly polarised waves is investigated. Taking advantage of linearly polarised waves could relax the requirements to the directivity of the antennas.

Moreover, materials that are typically used in tracking detectors are analysed with respect to their reflectivity and transmittance in the 60 GHz frequency band. To reduce crosstalk induced by reflections the applicability of graphite foam is investigated. It could be used to cover the layers or shield the links from each other. This material is commonly used in microwave applications, though its properties in the 60 GHz frequency band have not yet been determined sufficiently. Therefore, the reflectivity, transmittance and absorbance of graphite foam have been measured. The chapter ends with measurements conducted to quantify the expected crosstalk in a tracking detector and how the aforementioned approaches can address this problem.

⁴ASIC = Application Specific Integrated Circuit

⁵polyimide film developed by DuPont™

Chapter 6 presents the bit error rate test which is used for the reference system and can be applied for testing the upcoming chip prototype. The chapter summarises the implementation and results achieved with the transceiver at disposal. Moreover, the quality of the data transferred wirelessly has been analysed with a digital serial analyser. Tests of the data transmission including crosstalk between two wireless links have been performed and the results are presented. At the end of this thesis the experimental results are discussed and an outlook to the next steps towards an implementation of a wireless tracker readout system at 60 GHz is given.

2 Basics

This chapter summarises the basics of wireless data transmission. It starts with a summary of classical electrodynamics including Maxwell's equations and the Fresnel equations. A short introduction to antennas is given which is followed by a passage about the decibel unit system. The basics of data transmission are discussed. In this context the modulation schemes are presented that play a role in the subsequent chapters.

2.1 Electromagnetic Waves

The most important parts and formulae of classical electrodynamics are presented in this section which are necessary to understand electromagnetic waves and their propagation. It starts with Maxwell's equations and the uniform plane wave solutions, where polarisation is introduced. Afterwards, the Fresnel equations are presented which describe reflection and transmission of waves at a plane boundary between two dielectrics. Together with the Lambert-Beer law a simple model is developed to describe the transmission through a material layer of finite thickness.

2.1.1 Maxwell's Equations

The four fundamental equations which are the foundation for classical electrodynamics are Maxwell's equations [9]

$$\vec{\nabla} \cdot \vec{D} = \rho, \quad (2.1)$$

$$\vec{\nabla} \times \vec{H} - \frac{\partial \vec{D}}{\partial t} = \vec{j}, \quad (2.2)$$

$$\vec{\nabla} \times \vec{E} + \frac{\partial \vec{B}}{\partial t} = 0, \quad (2.3)$$

$$\vec{\nabla} \cdot \vec{B} = 0, \quad (2.4)$$

given in SI units, where \vec{E} and \vec{B} represent the electric and magnetic field, \vec{D} is the electric displacement and \vec{H} the magnetising field. The charge and current density are denoted by ρ and \vec{j} , respectively. The following relations exist between the fields:

$$\vec{D} = \varepsilon_r \varepsilon_0 \vec{E}, \quad (2.5)$$

$$\vec{B} = \mu_r \mu_0 \vec{H}, \quad (2.6)$$

where ε_0 and μ_0 are the vacuum permittivity and permeability, ε_r and μ_r are the relative permittivity and permeability of a medium, which are generally frequency dependent and complex.

2.1.2 Plane Waves

In the case of a linear and homogeneous, nonconducting medium without sources, i.e. $\rho = 0$ and $\vec{j} = 0$, one can derive from equations 2.2 and 2.3 the wave equation [10]

$$\Delta \vec{E} = \varepsilon \mu \frac{\partial^2 \vec{E}}{\partial t^2}, \quad (2.7)$$

where $\mu = \mu_r \mu_0$ and $\varepsilon = \varepsilon_r \varepsilon_0$. The simplest solutions of Equation 2.7, which also satisfy the remaining two Maxwell equations, are plane transverse waves

$$\vec{E}(\vec{x}, t) = (\vec{\epsilon}_1 E_1 + \vec{\epsilon}_2 E_2) e^{i\vec{k}\vec{x} - i\omega t}, \quad (2.8)$$

which are harmonic functions in time with frequency ω and consist of two transverse ($\vec{k} \cdot \vec{\epsilon} = 0$) and in general complex polarisation components, according to [9]. If there is no phase difference between the polarisation components the waves are linearly polarised. Otherwise, the waves are elliptically polarised. If E_1 and E_2 have the same magnitude and a phase difference of exactly 90° , these waves are circularly polarised.

As only the real part of the electric field is a measurable quantity, the observable electric field of a linearly polarised wave travelling in z-direction turns out to be

$$\vec{E} = \vec{E}_0 \cdot \cos(\omega t - kz), \quad (2.9)$$

where $E_z = 0$ holds from the transversality condition [10].

As the Maxwell equations are linear in \vec{E} and \vec{B} , any linear combination of solutions is a solution as well. This is called the superposition principle and leads to interference as the amplitudes of different waves are coherently added up

$$\vec{E}_{tot}(\vec{x}, t) = \sum_n \vec{E}_n(\vec{x}, t). \quad (2.10)$$

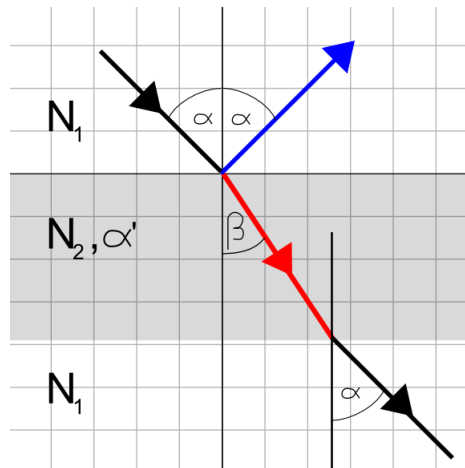


Figure 2.1: Reflection, refraction and transmission at an interface of finite thickness.

2.1.3 Reflection and Transmission at Plane Surfaces

At a plane interface between two dielectrics electromagnetic waves are partially reflected and transmitted, whereas the angle of reflection equals the incident angle. The transmitted wave gets refracted. The angle of the transmitted wave follows from Snell's law with the indices of refraction N of both media [10]

$$N_1 \sin \alpha = N_2 \sin \beta, \quad (2.11)$$

$$N = \sqrt{\mu_r \epsilon_r}, \quad (2.12)$$

where N is in general complex $N = n - i\kappa$ as it is defined by Equation 2.12. Its real part n equals the ratio of the speed of light in vacuum and in the medium, whereas its imaginary part $\kappa \neq 0$ yields absorption of the electromagnetic waves in the medium. The described situation is illustrated by the upper boundary in Figure 2.1.

The amplitudes of the reflected and transmitted waves can be derived from Maxwell's equations by using the continuity conditions for all four fields. The amplitude ratios depend on the polarisation of the incident wave. One denotes the component parallel to the incident plane spanned by the wave vector \vec{k} and the normal of the interface with p . The component perpendicular to this plane is indicated with s ¹.

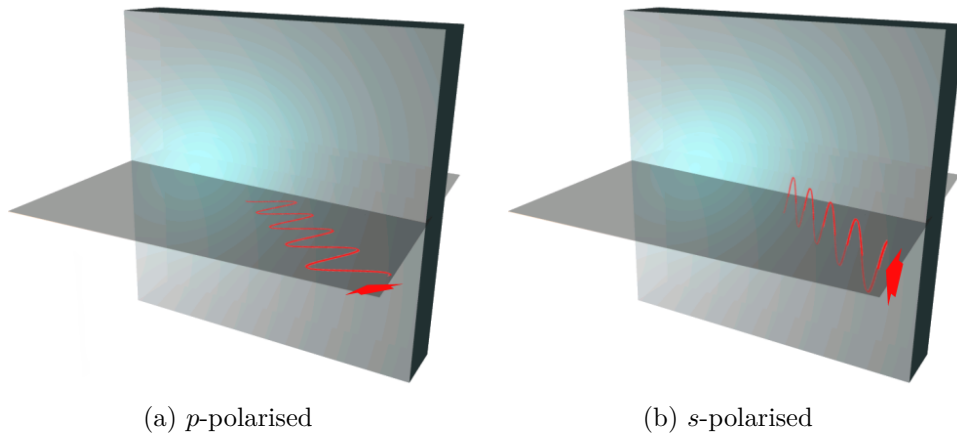


Figure 2.2: Waves with (a) parallel polarisation (p -polarised) and (b) perpendicular polarisation (s -polarised) with respect to the incident plane spanned by the wavevector and the normal of the surface. Images taken from [11].

In the following r and t represent the amplitude ratios of the reflected or transmitted and the incident wave, respectively. The equations below are the Fresnel equations for both polarisations under the assumption that both media have the same magnetic permeability μ [11]. In case of ideal dielectrics the absorption coefficient $\kappa \rightarrow 0$ and so $N \rightarrow n$ becomes a real number, which simplifies Equations 2.13 - 2.16 [10]. From Equation 2.15 one can see that for ideal dielectrics $r_p \rightarrow 0$ for $\alpha + \beta = 90^\circ$. This angle

¹from german "senkrecht"

α_B is the so called Brewster angle under which no parallel polarised waves are reflected.

$$r_s = \frac{N_1 \cos \alpha - N_2 \cos \beta}{N_1 \cos \alpha + N_2 \cos \beta} \xrightarrow{\kappa=0} -\frac{\sin(\alpha - \beta)}{\sin(\alpha + \beta)} \quad (2.13)$$

$$t_s = \frac{2N_1 \cos \alpha}{N_1 \cos \alpha + N_2 \cos \beta} \xrightarrow{\kappa=0} \frac{2 \sin \beta \cos \alpha}{\sin(\alpha + \beta)} \quad (2.14)$$

$$r_p = \frac{N_2 \cos \alpha - N_1 \cos \beta}{N_2 \cos \alpha + N_1 \cos \beta} \xrightarrow{\kappa=0} \frac{\tan(\alpha - \beta)}{\tan(\alpha + \beta)} \quad (2.15)$$

$$t_p = \frac{2N_1 \cos \alpha}{N_2 \cos \alpha + N_1 \cos \beta} \xrightarrow{\kappa=0} \frac{2 \sin \beta \cos \alpha}{\sin(\alpha + \beta) \cos(\alpha + \beta)} \quad (2.16)$$

Because the amplitude of the electric field is not directly measurable unlike the intensity of the waves, one has to take the squared absolute value of the the amplitude ratios. Since the refracted angle is not equal to the incident angle, one has to take the different cross section of the beam into account in order to fulfill energy conservation. The intensity ratios R and T hold for both polarisations.

$$R = |r|^2 \quad (2.17)$$

$$T = \left| \frac{N_2 \cos \beta}{N_1 \cos \alpha} \right| \cdot |t|^2 \quad (2.18)$$

2.1.4 Absorption and Transmission Through a Layer of Finite Thickness

Now consider an example as it is depicted in Figure 2.1 where an electromagnetic wave travelling in air ($N_1 \approx 1$) traverses a homogeneous layer of material (e.g. graphite foam) of thickness z with complex index of refraction $N_2 = n - i\kappa$. In the simplest model reflections at the lower surface can be neglected, so that the reflected intensity follows from the Fresnel equations. As the transmitted wave crosses two boundaries one has to multiply the Fresnel equations at each surface with interchanged indices of refraction and angle of incidence. As the first and third medium are the same, the cross section term of Equation 2.18 drops out. Besides, one has to take into account the imaginary part of the index of refraction, which leads to the Lambert-Beer law [10]

$$I(z) = I_0 \cdot e^{-\alpha' z}. \quad (2.19)$$

It describes the exponential loss in intensity due to absorption. The absorption coefficient α' is connected to the imaginary part κ of N via

$$\alpha' = \frac{4\pi\kappa}{\lambda_0}, \quad (2.20)$$

with the vacuum wavelength λ_0 . The transmitted intensity T behind the layer is therefore

$$T = \left| t_{\alpha \rightarrow \beta} \right|^2 \cdot \left| t_{\beta \rightarrow \alpha} \right|^2 \cdot e^{-\alpha' z}. \quad (2.21)$$

2.2 Properties of Antennas

This section summarises the basic terms that are typically used to characterise antennas and to describe antenna theory.

The first one is the directivity D of the antenna. It is defined as the maximum intensity P_{max} transmitted by the antenna compared to that of an isotropic emitter P_{iso} such that

$$D = \frac{P_{max}}{P_{iso}}, \quad (2.22)$$

where the intensity drops with distance r^2 such that

$$P_{iso}(r) = \frac{P_0}{4\pi r^2}, \quad (2.23)$$

according to [12]. The gain G of an antenna takes its efficiency η into account which incorporates power loss due to an impedance mismatch for example, such that

$$G = D\eta. \quad (2.24)$$

The beamwidth of the antenna is defined as the angular range where the transmitted intensity drops by 3 dB from the maximal value, i.e. to half of the maximum output power [13]. It is directly linked to the gain of the antenna such that a high gain is associated to a corresponding small beamwidth.

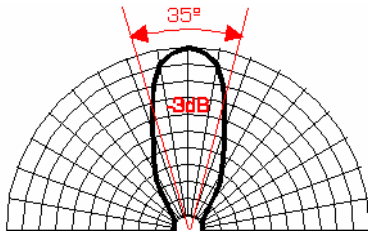


Figure 2.3: Polar pattern of an antenna. 3 dB beamwidth of 35° indicated. Image taken from [14]

The polarisation of an antenna is described by the polarisation of the transmitted electromagnetic waves. Pyramidal horn antennas, which are discussed in the experimental part, are linearly polarised [15]. The planes spanned by the electric and magnetic field vectors together with the propagation direction of the emitted waves are therefore referred to as E-plane and H-plane, respectively. The planes are illustrated in Figure 2.4.

The most important equation of antenna theory describes the path loss in free-space which is dependent on the distance between transmitter and receiver, but also on the wavelength of the electromagnetic waves. Together with the gain of both transmitting

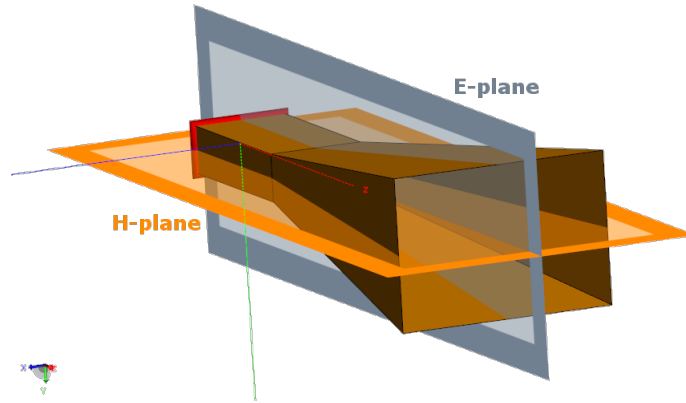


Figure 2.4: E-plane and H-plane of a horn antenna spanned by the field vectors and the direction of the waves

and receiving antennas, G_t and G_r , the Friis transmission equation reads as follows [12]

$$P_r = P_t G_r G_t \left(\frac{\lambda}{4\pi r} \right)^2, \quad (2.25)$$

where P_r and P_t are the received and transmitted intensity, respectively. This equation holds for distances $r \gg \lambda$, that means in the antennas' far field. It can be evaluated in decibels in order to get a feeling for the attenuation as a function of distance. For 60 GHz radiation which corresponds to a 5 mm wavelength the path loss at 1 m is already -68 dB because of the short wavelength. This is a reason why the 60 GHz data transfer is suitable for rather short range applications.

2.3 The Decibel Unit System

Intensities of radio waves used for communication or reflection coefficients are often expressed in decibel (dB). The decibel units are derived from the logarithm of two values that are to be compared [16]

$$L_{dB} = 10 \log_{10} \left(\frac{P_1}{P_0} \right). \quad (2.26)$$

In order to get an absolute value from a quantity in dB one usually needs a reference value. For the measurement of power one typically chooses $P_0 = 1 \text{ mW}$ such that the power P_1 is given in dBm (decibels per milliwatt)

$$P_{dBm} = 10 \log_{10} \left(\frac{P_1}{1 \text{ mW}} \right). \quad (2.27)$$

The gain of an antenna is often compared to an isotropic emitter. This is denoted by the unit dBi (decibels with respect to an isotropic emitter) such that

$$G_{dBi} = 10 \log_{10} \left(\frac{P_{max}}{P_{iso}} \right). \quad (2.28)$$

2.4 Data Transmission and Modulation Schemes

The purpose of communication systems is to transfer data physically from one point to another. This transmission takes place by the transfer of electromagnetic signals along communication channels like wires, optical fibres or wireless channels. For a wired transmission the data is represented by an electrical voltage. It can be transferred directly in its original state as a baseband signal which means that it does not require modulation onto a higher frequency for transmission. In general its frequency spectrum ranges from low frequencies to a cut-off frequency [17]. For a wireless transmission the signal must be lifted from the baseband into a higher frequency range. This happens via modulation of the signal, therefore called the modulation signal, onto a periodic waveform which is referred to as the carrier frequency. Wireless channels offer a specific bandwidth around the carrier frequency. The signal modulated into this bandwidth is called the passband signal [18].

One distinguishes analog and digital modulation techniques. Analog modulation schemes are applied e.g. in radio broadcasting. The information is modulated either in the amplitude (AM), the frequency (FM) or the phase (PM) of the carrier signal. For frequency modulation the modulation index m is defined as the ratio of the modulated frequency δ_f and the modulation signal's frequency f_m such that

$$m = \frac{\delta_f}{f_m}. \quad (2.29)$$

Digital modulation schemes are more efficient and offer a higher noise immunity compared to analog techniques [19]. They are used e.g. in mobile phones and WiFi. The fundamental modulation methods are based on amplitude-shift-keying (ASK), frequency-shift-keying (FSK), phase-shift-keying (PSK) and quadrature amplitude modulation (QAM). The latter is based on IQ modulation which is explained in section 2.4.2. The modulation schemes differ in their spectral efficiency which equals the number of bits that can be transferred per second depending on the carrier's frequency. A higher spectral efficiency generally requires a more complex baseband circuitry and a higher signal to noise ratio for stable transmission. The receiver recovers the data signal from the passband. Depending on the modulation scheme the knowledge of the carrier's phase is necessary, which is called coherent demodulation, or it is not required, which is called non-coherent demodulation.

In the following three modulation schemes are presented and their respective advantages

are highlighted. The first one is On-Off-Keying (OOK) which will be implemented in the new transceiver prototype that is introduced in Section 3.5. The second scheme covered is the general IQ modulation and the third one is Minimum Shift Keying (MSK). Both can be used for the reference transceivers which are presented in Chapter 4.

2.4.1 On-Off-Keying

OOK is a very simple modulation scheme [20] as it is a specific form of ASK. The carrier is switched on if a logic 1 is to be transmitted, otherwise it is turned off which also saves power. It can be easily implemented with a switch and an AM-detector. Therefore it does not need a large baseband circuitry and can be demodulated non-coherently. But this simplicity costs bandwidth. The spectral efficiency of OOK is only $0.5 \text{ b}/(\text{s} \cdot \text{Hz})$, so one needs a bandwidth of 7 GHz to transfer 3.5 Gbps for example. The modulation scheme is illustrated in Figure 2.5.

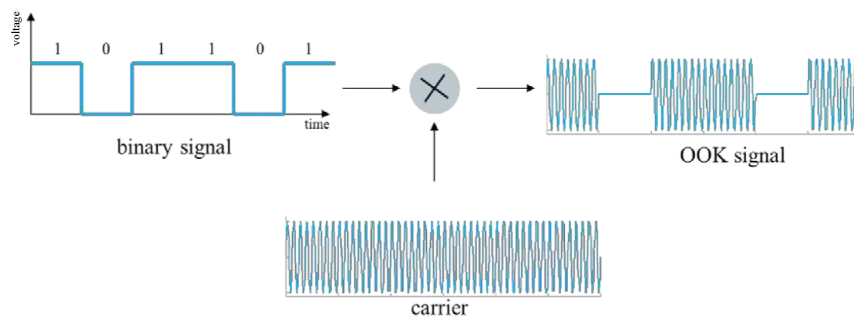


Figure 2.5: Principle of On-Off-Keying

2.4.2 IQ Modulation

The general IQ modulation uses two signals called the In-phase (I) and the Quadrature (Q) component. They are mixed orthogonally onto the carrier of frequency ω and summed afterwards [21]. The mixer block diagram is depicted in Figure 2.6(a). The components I and Q span a two-dimensional plane called the constellation diagram. There are different possibilities how a modulation scheme can use this plane: fixed points in the diagram or phase shifts can be assigned to specific data symbols. The first option is used in QAM (Quadrature Amplitude Modulation), e.g. 16-QAM which is illustrated in Figure 2.6(b). Four different values of each I and Q yield 16 different states in the constellation diagram. Each of these points represents a symbol that consists of four bits. The spectral efficiency of this kind of modulation is therefore higher as several bits can be transferred at the same time. For 16-QAM one reaches $4 \text{ b}/(\text{s} \cdot \text{Hz})$. One uses such modulation schemes if the available bandwidth is limited but higher data rates are required. But a more complex baseband circuitry is necessary as most of the modulation schemes using IQ mixers have to be demodulated coherently. This requires

the use of ADCs² and DACs³ and tracking of the phase between transmitter and receiver.

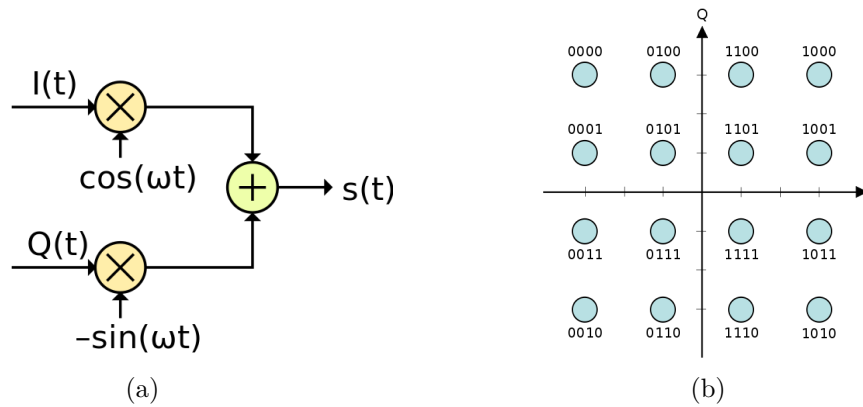


Figure 2.6: IQ modulation: (a) IQ mixer block diagram; (b) Example for IQ modulation: 16-QAM represented in the constellation diagram. Both images taken from [21].

2.4.3 Minimum Shift Keying

Minimum Shift Keying (MSK) is a specific form of IQ modulation which can be also considered as a form of frequency modulation (FM) [22]. Therefore, demodulation can be performed non-coherently and analog to digital converters are not necessary. More specific, MSK is a kind of constant-phase frequency-shift keying (CPFSK) which saves bandwidth as there are no phase discontinuities. Its spectral efficiency of 1 b/(s · Hz) is lower compared to more sophisticated IQ-modulation schemes but higher than that of OOK.

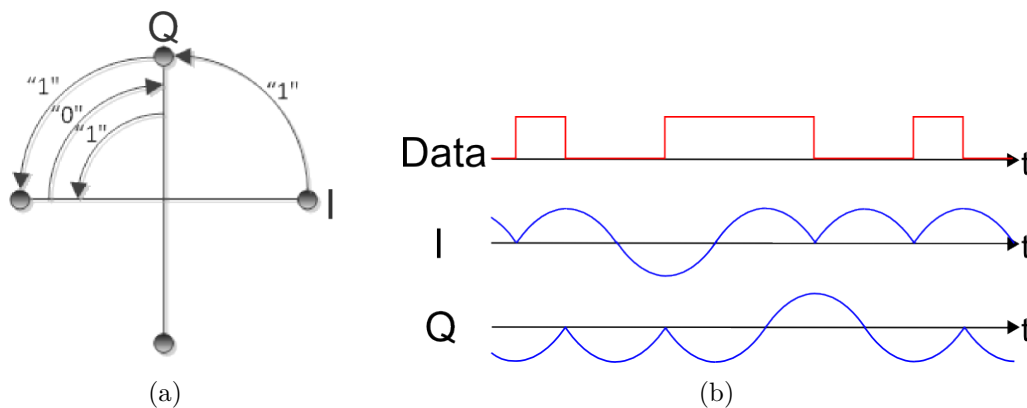


Figure 2.7: Principle of MSK modulation using IQ signals. (a) Constellation diagram, taken from [23]. (b) I- and Q-sinusoids inverted at the zero-crossings correspondingly to the data stream drawn above.

²ADC = Analog to Digital Converter

³DAC = Digital to Analog Converter

MSK uses a baseband of two sinusoids at a frequency f with a relative phase shift of 90° and equal amplitudes. In the constellation diagram shown in Figure 2.7(a) this results in a rotation either counterclockwise or clockwise depending on which component runs ahead. In frequency space the counterclockwise rotation results in a positive modulated frequency $\delta_f = f$, whereas the clockwise rotation results in a negative $\delta_f = -f$. This follows from Euler's identity as I and Q can be treated like the two components of a complex number. Thus, two orthogonal frequency states are represented by the rotational direction. Logical bit states can be assigned to these states such that a binary 1 is transmitted by a counterclockwise rotation and a binary 0 by a clockwise rotation. As the data rate that can be achieved is four times the baseband's frequency the modulation index of MSK is $m = 0.25$. This is the smallest possible value for any form of frequency shift keying, thus it is called minimum. In order to create transitions between 1s and 0s the baseband sinusoids are inverted at their respective zero-crossings. This is illustrated in figure 2.7(b). In doing so the rotational direction in the constellation diagram can be changed.

The following table summarises the most important facts about the three different modulation schemes presented above.

Modulation scheme	Spectral efficiency [b/(s · Hz)]	IQ mixer necessary	Demodulation non-coherently
OOK	0.5	✗	✓
MSK	1	✓	✓
16-QAM	4	✓	✗

Table 2.1: Summary of modulation schemes

3 A New Wireless Readout Technique at 60 GHz for the ATLAS Tracker Upgrade

This chapter covers the current ATLAS tracking detector as well as the Phase-II Upgrade of the inner detector. The requirements are discussed that are imposed on the tracker's readout system after the high luminosity upgrade of the LHC that should take place between 2022 and 2023. The idea of a wireless readout system operating in the license-free frequency band around 60 GHz is presented. Its implementation in the tracker and its advantages are discussed in the following.

3.1 The ATLAS Detector

The ATLAS detector is one of the four big experiments at the LHC which attracted major media attention in the last few years caused by the discovery of a Higgs particle [24] together with the CMS experiment [25].

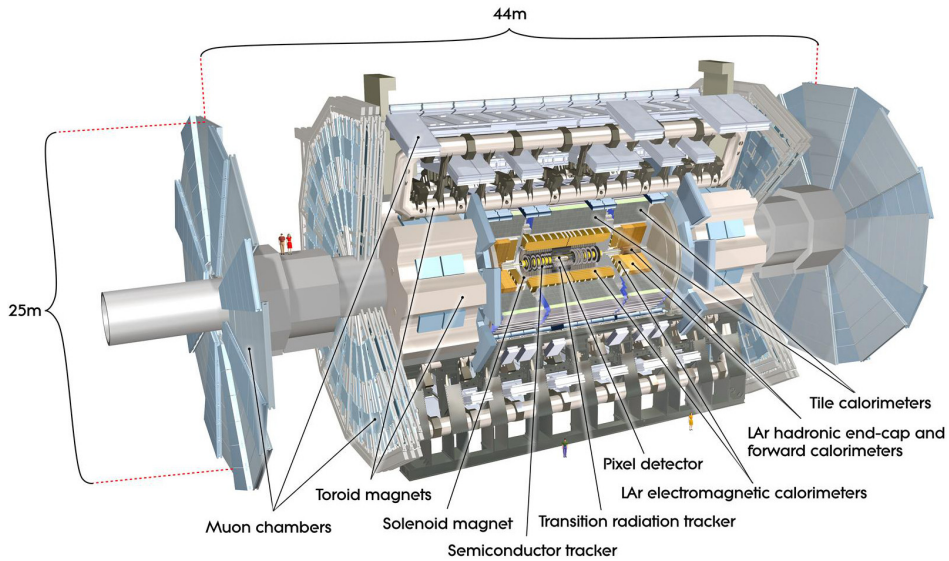


Figure 3.1: A model of the ATLAS detector [26]

The detector consists of four major components [27]: the inner detector measures the momentum of each charged particle, the calorimeters measure the energy carried by the particles, the muon spectrometer identifies muons and measures their momenta and last but not least the magnet system generates the magnetic field to bend the trajectories of charged particles in order to determine their momenta. A model of the full detector is

illustrated in Figure 3.1.

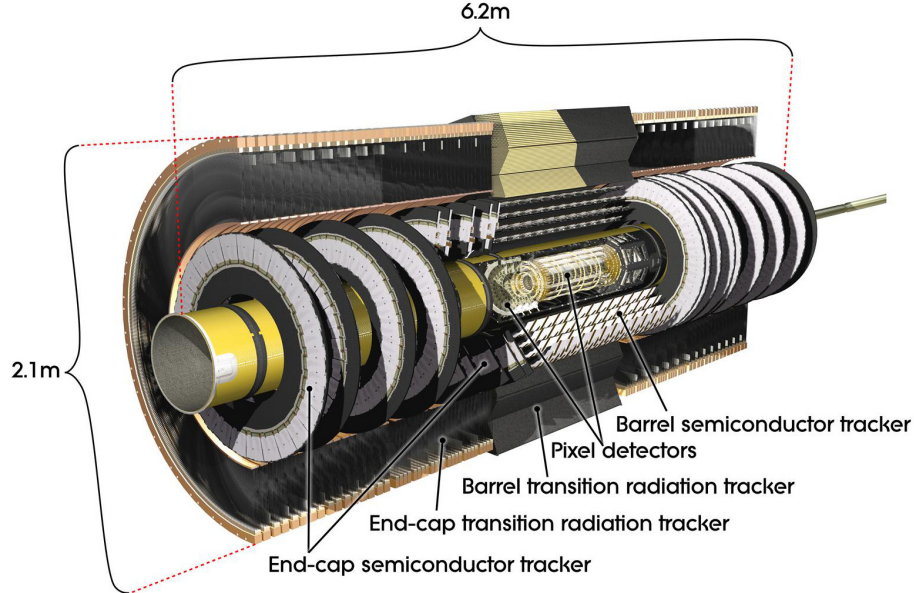


Figure 3.2: The ATLAS inner detector [26]

The inner detector consists of three components [27]: the silicon pixel detector is closest to the interaction point. It consists of three layers and provides data for vertex reconstruction. The semiconductor tracker (SCT) consists of four double layers of silicon microstrip detector modules. The outermost part of the inner detector is the transition radiation tracker (TRT) that is based on straw detectors and is used for electron identification. A close up of the inner detector model is depicted in Figure 3.2.

The trigger decision of the ATLAS experiment is split into three stages. The first level trigger is a pure hardware trigger with a decision latency of about $2.5 \mu\text{s}$ [28] that reduces the incoming event rate of 40 MHz by a factor of 400. It is followed by two software level triggers which further reduce the event rate by a factor of 30 and 15 respectively. By that, one ends up at an outgoing event rate of 200 Hz. The raw data recorded per event after the third level trigger are equivalent to 1.6 MB [2]. The hardware trigger relies on information from the muon spectrometer and the calorimeters [1]. So far, the silicon strip tracker is not involved in this first level of the trigger decision.

The current SCT consists of a barrel of four double layers of silicon strip sensors and two endcaps with nine layers each. The total number of 4088 modules is readout redundantly with two optical links per module operating at 40 Mb/s each [3]. The data is readout axially along the beam pipe. The cables and connectors inside the tracker induce multiple Coulomb scattering.

3.2 The Phase-II Upgrade of the ATLAS Detector

Between 2022 and 2023 the LHC will be upgraded to provide a higher instantaneous luminosity of about $5 \times 10^{34} \text{ cm}^{-2}\text{s}^{-1}$. Over ten years of operation the HL-LHC is aimed to deliver about 2500 fb^{-1} of data [29]. This huge data sample will allow e.g. for a significant improvement of the precision of the measurements of the Higgs couplings or for a search for new physics at an extended energy scale.

For the high luminosity upgrade of the LHC the inner detector of the ATLAS experiment will have to be replaced. The current model for the upgrade consists of four layers of pixel detectors and five layers of strip sensors [5]. With increasing luminosity not only the event rate increases but so does the number of pile-up collisions as well. The current Level-1 hardware trigger will have to face many challenges that are associated with the overall rate. The efficiency of the calorimeter isolation will be degraded and the resolution of the current level-1 muon chamber would not be sufficient [28]. The tracker has a much higher granularity than the calorimeter or the muon chambers. It would be well suited to cope with the high track density in the HL-LHC. Adding information from the tracker to the hardware trigger decision, i.e. building a Level-1 track trigger, might remedy the problems stated above. It will improve momentum resolution and yield a better identification of isolated leptons [28].

The new hardware trigger decision is intended to be split into a Level-0/Level-1 architecture based on a regions of interest (RoI) approach [5]. The proposed Level-0 hardware trigger uses information from the calorimeter and muon spectrometer as before to define the RoIs. Its rate would be at least 500 kHz within a latency of $6 \mu\text{s}$. The planned Level-1 trigger operates in these RoIs and is based on the tracker and the aforementioned detectors. It will reduce the rate to 200 kHz within an additional latency of $14 \mu\text{s}$. A second option for the implementation of a track trigger uses a self-seeded approach. Therefore the high- p_T tracks must be reconstructed not only in the defined RoIs, but in the full coverage of the tracker, which requires more bandwidth.

Along with the replacement of the tracking detector a new readout system must be developed. The currently used optical links are not capable of transferring the huge amount of data provided by the upgraded tracker. But a fast readout is essential for a track trigger. For the self-seeded approach the necessary bandwidth to readout all 1-hit and 2-hit clusters of the silicon strip tracker, which are produced by interesting events with high transverse momenta, is estimated to be between 50 and 100 Tbps [7]. Splitting the readout system into about 20 000 links yields a bandwidth of up to 5 Gbps per link. The bandwidth of today's readout systems is limited by the power and material budget as well as the space this system occupies inside the tracker. It is therefore of importance that a new readout system does not only offer a high bandwidth but that it consists of little amount of material, has low power consumption and small form factor at the same time. Such a system can be provided by using the 60 GHz wireless technology.

3.3 Wireless Data Transfer at 60 GHz

In the last couple of years wireless communication systems have found their way into everyday life. The need for systems that can transfer high data rates has led to a growing interest in millimetre waves. The unlicensed frequency band at 60 GHz is available for open research since 2001. It offers a bandwidth of 7 to 9 GHz depending on the country, except e.g. Australia. The license-free spectrum is depicted in Figure 3.3. Using the full bandwidth it is possible to transfer 10's of Gbps depending on the modulation scheme [8].

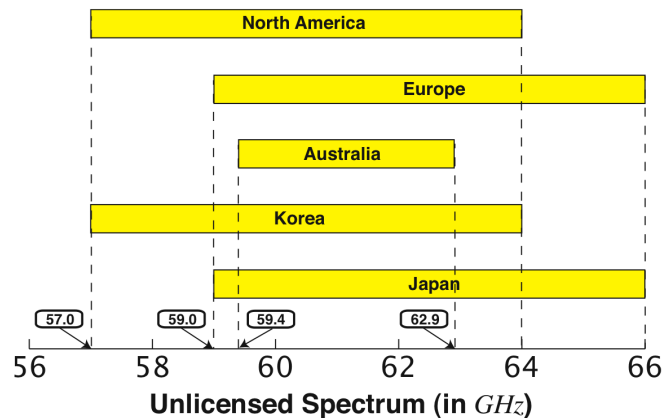


Figure 3.3: The unlicensed 60 GHz frequency band [30]

The wavelength in this frequency band is about 5 mm which yields a form factor that is about 140 times smaller than that of today's wifi operating at 5 GHz [31]. This allows for high level integration including antennas placed directly on the chip [6]. The usage is limited to short range applications due to the high free-space path loss of 68 dB at 1 m distance. Moreover, the signal would be attenuated in the atmosphere due to absorption by oxygen or rain at large distances [32]. Up to now the 60 GHz spectrum is still largely unused which induces only low interference that could distort communication. Furthermore, the radio signal does not penetrate walls. This allows for secure communication.

3.4 A Wireless Tracker Readout System

Our approach for a high bandwidth readout system for future tracking detectors is to establish a wireless readout system operating in the 60 GHz band. Such a system would meet the high bandwidth requirement and not strain the material and power budgets as the links would be of short range of about 10 cm. Huge output power of the transmitter are therefore not necessary for stable communication. Moreover, one can get rid of the bunches of data cables and their respective connectors inside the tracking volume which would reduce the multiple Coulomb scattering probability. The readout system could be implemented in such a way that the data is transferred radially from the inner layers to the outer enclosure of the detector as depicted in Figure 3.4(a). Thus the data would follow the topology of high- p_T events. This would ease the implementation of a first

level track trigger since hits from the same high- p_T tracks would be readout by only a few adjacent links.

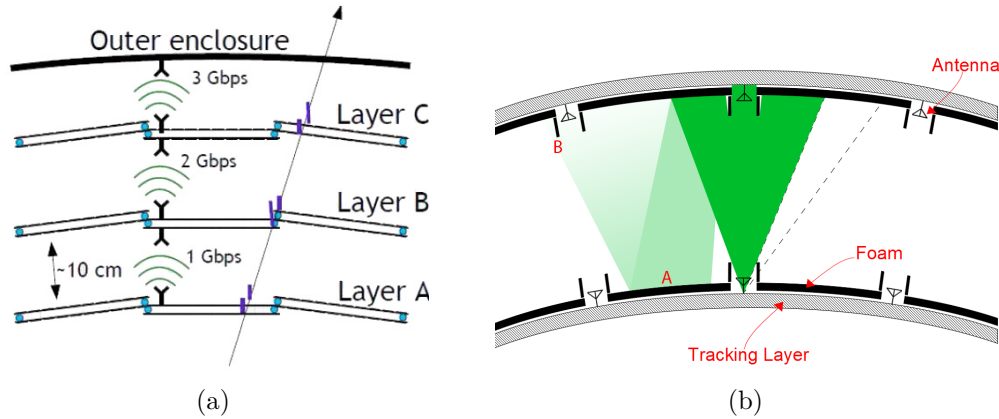


Figure 3.4: A radial readout of a tracker facilitated by a wireless system operating at 60 GHz. (a) Data transfer from the inner layers to the outer enclosure. Image taken from [33]. (b) Approach to reduce crosstalk by putting absorbing material on the detector surfaces to attenuate reflections and by placing shielding around the antennas. Image adapted from [34].

It was found that the radio signal at 60 GHz cannot penetrate the tracker modules that are currently used in the ATLAS SCT as it is attenuated by about 20 dB on average [7]. On the one hand, this means that the other detectors like calorimeter and muon spectrometer will not be influenced by the wireless readout system and that links between different layers do not interfere with each other. On the other hand, the signals reflected by the layers will induce crosstalk between links on the same layer. A simulation by Hugle [35] showed that data transfer would not be possible without directing the signal or shielding the links from each other. There are different approaches to address this problem like directive antennas or absorbing materials which are investigated in this thesis. An exemplary sketch of an attempt to reduce crosstalk with an absorbing material covering the reflective modules is shown in Figure 3.4(b). The most promising candidate for an absorber is graphite foam, which has a low density and is highly absorbent in the microwave range. The communication from the innermost layers to the outer enclosure requires connections between the transceivers on the receiving and transmitting side of the layer which could be established by wires or vias.

3.5 A New 60 GHz Transceiver

There are already some 60 GHz transceivers commercially available but these do not meet the requirements for a tracking readout system. First of all, the inner detector of the ATLAS experiment is a very harsh environment for electronic devices, so radiation hardness is an issue. This is not taken into account for transceivers that are targeted for applications like wireless high definition video streaming at home. Moreover, the power

consumption may be too high as these chips provide more output power than necessary for short link distances of about 10 cm. In addition general purpose transceivers typically use IQ-modulation which requires a large analogue and digital baseband circuitry. Modulation schemes are discussed in Section 2.4. In the following paragraphs a first prototype of a radiation hard 60 GHz transceiver and the chosen production technology are described. The transceiver has been presented first by Soltveit et al. [8].

3.5.1 Functional Design

The design comprises transmitter and receiver in a single chip. The block diagrams of both chains are illustrated in figures 3.5 and 3.6. The targeted data rate of the first prototype is 3.5 Gb/s using the full spectral bandwidth of 7 GHz and On-Off-Keying (OOK) as modulation scheme. The aimed power consumption is below 0.5 W.

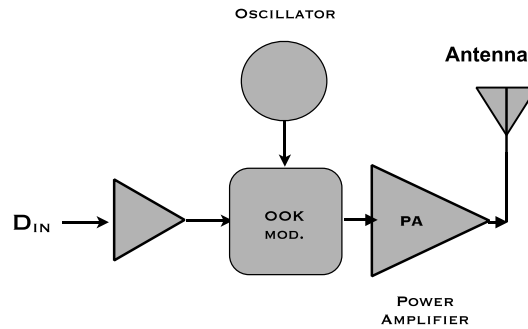


Figure 3.5: Block diagram of the transmitter chain.

The transmitter chain consists of the following stages: the data input drives the OOK-modulation block which switches the 60 GHz carrier signal provided by a voltage controlled oscillator (VCO). Afterwards the radio frequency (RF) signal is amplified by a power amplifier (PA) that provides high gain to reach the required power level at the receiver. The PA is followed by a bandpass filter (BPF) which is skipped in the diagram in order to focus on the most important blocks. It suppresses noise induced by the PA as well as carrier feedthrough [8].

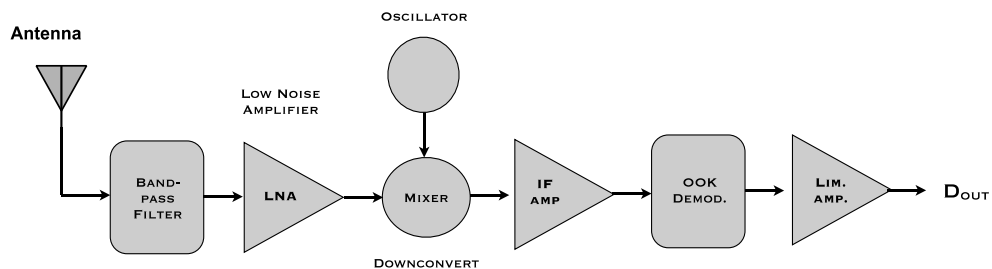


Figure 3.6: Block diagram of the receiver chain.

The receiver's purpose is to detect the modulated 60 GHz RF signal which is usually of

low intensity. After a BPF that reduces out-of-band noise the signal reaches the low noise amplifier (LNA). Its function is to amplify the small signal but to add as little noise as possible to the signal. For further signal processing the RF signal is down-converted to an intermediate frequency (IF) of 7 GHz using a Gilbert mixer and a local oscillator (LO) because the following functions can be implemented with less noise operating at lower frequencies. It is followed by another bandpass filter that eliminates noise from the down conversion process which is left out in the block diagram for the aforementioned reason. The IF is once again amplified before the OOK demodulator recovers the transmitted data. The purpose of the last amplifier is to deliver the demodulated data at the desired amplitude.

3.5.2 Technology

The technology for the transceiver is chosen to be 130 nm SiGe¹ HBT BiCMOS 8HP technology from IBM [36]. HBT stands for heterojunction bipolar transistor, a kind of transistors that can handle up to several hundred GHz [37]. BiCMOS transistors integrate the bipolar junction transistor technology and the CMOS² technology [38]. The decision for this technology is based on the following considerations: the technology must fulfill requirements like low noise and linearity at the targeted high frequencies. The production yield should be high and the costs reasonably low at the same time. There are two technologies which come into consideration with respect to availability and costs. These are CMOS and SiGe HBT BiCMOS. Gallium arsenide (GaAs) technologies are more costly [36]. SiGe HBT BiCMOS has the advantage over CMOS that it provides less process variability and a higher breakdown voltage. It allows for a high level of integration combining high speed HBTs and standard CMOS transistors. Moreover, the performance after irradiation has been tested and it was found that the technology is suited for operating in the tracker after the high luminosity upgrade [39].

¹SiGe = Silicium Germanium

²CMOS = Complementary Metal Oxide Semiconductor

4 The Reference Transceivers

In order to build a reliable test bench for the chip prototype, commercially available 60 GHz chipsets were tested and used for the experiments. There were two different transceiver evaluation kits at disposal at the time of this thesis: the Gotmic TX/RXQ060A01 and the Hittite HMC6451 evaluation kit.

4.1 Gotmic 60 GHz Transmitter and Receiver

The TXQ060A01 and RXQ060A01 transmitter and receiver chipsets from Gotmic¹ use GaAs technology. In contrast to the design under development this chip uses IQ modulation and a factor four frequency multiplier to generate the carrier frequency. Thus an external local oscillator of 15 GHz is required to generate the 60 GHz carrier frequency. The block diagram of transmitter and receiver are illustrated in Figure 4.1. A photo of the transmitter evaluation board is shown in Figure 4.2(a). The board provides connectors for the bias voltages and a single pad antenna as a feed for directive antennas. The intermediate frequency bandwidth of the transmitter is 8 GHz, such that the full spectral bandwidth is exploited.

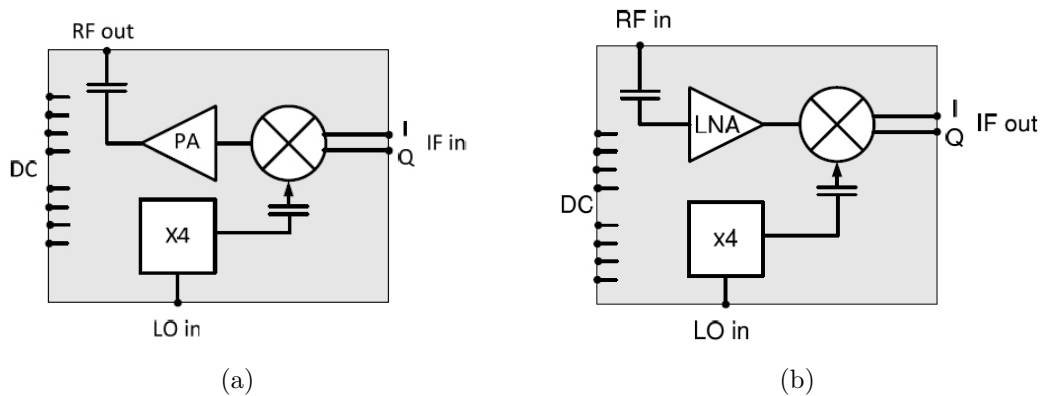


Figure 4.1: Block diagram of the Gotmic (a) Transmitter [40] and (b) Receiver [41]. LO is the local oscillator that is quadrupled to generate the carrier frequency. IF is the intermediate frequency that is mixed with the carrier in the transmitter and recovered from the radio frequency (RF) in the receiver. PA = Power Amplifier, LNA = Low Noise Amplifier.

Applying a sine wave of fixed frequency f_{IF} to one of the IQ inputs results in three peaks in the radio frequency's spectrum: the carrier frequency $f_c = 4f_{LO}$ generated by

¹www.Gotmic.se

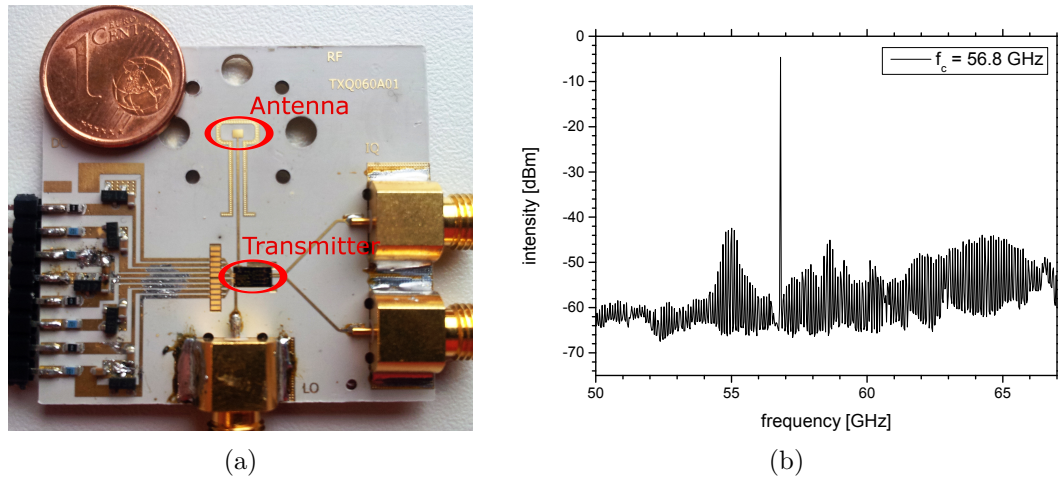


Figure 4.2: Gotmic transmitter and its bandwidth; (a) the Gotmic TXQ060A01 on its evaluation board; (b) Radio frequency spectrum using a carrier of $f_c = 56.8$ GHz and varying intermediate frequency.

the frequency quadrupling of the local oscillator's input f_{LO} and the upper and lower sidebands $f_{USB} = f_c + f_{IF}$ and $f_{LSB} = f_c - f_{IF}$ produced by the mixer. If operating correctly the carrier frequency should be suppressed by about 30 dB with respect to the sidebands whose output level should be around 0 to 10 dBm. But it was found that the situation was reversed caused by a malfunction of the mixer. The intensity of the carrier was about 40 dB higher than that of the sidebands which were strongly suppressed.

This reflects in the measurement of the transmitter's intermediate frequency (IF) bandwidth at a fixed carrier frequency of 56.8 GHz. The local oscillator frequency of 14.2 GHz was provided by an Anritsu MC3692 signal generator. A second signal generator provided the IF signal with fixed intensity and varying frequency. The intensity of the radio frequency (RF) was measured with the FSU spectral analyser by Rohde&Schwarz. The spectrum is shown in Figure 4.2(b). The distinct carrier frequency peak and the highly suppressed remaining RF spectrum indicate the malfunction.

For the Gotmic chip the bias voltages for the different analogue stages had to be applied manually which allowed for tuning of the output power. The negative control voltages had to be applied before the positive supply voltages were turned on. The bias currents could be monitored using a remote control software accessing the power supplies (HAMEG HMP4040 from R&S) via USB. A picture of the graphical user interface can be found in the Appendix B. In the following it is referred to the bias currents with the names of their associated voltages Vd_PA for the power amplifier, Vd_x4 for the frequency multiplier and Vd_x4A for the frequency multiplier's amplifier. While the bias current Vd_x4A did not show any correlation with the local oscillator's frequency, a dependence of the bias currents Vd_x4 and Vd_PA on the applied local oscillator's frequency for fixed voltages was found which is shown in Figure 4.3(a). These two currents also depend on the power of the external local oscillator. This can be seen in Figure 4.3(b). The plot also shows the linearity of the power amplifier. The output power of

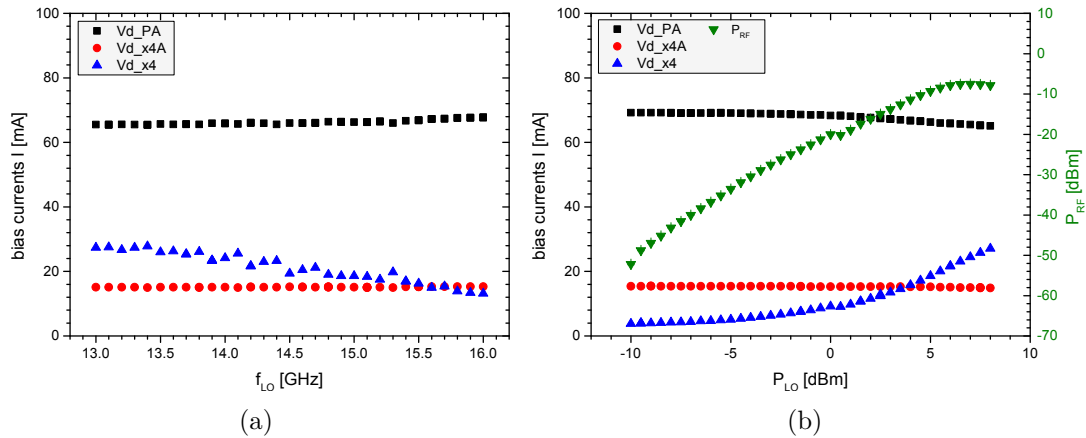


Figure 4.3: (a) Bias currents (power amplifier (Vd_{PA}), x4 multiplier's amplifier (Vd_{x4A}) and x4 multiplier (Vd_{x4})) of the Gotmic Tx as a function of the (LO) local oscillators-frequency.
 (b) Bias currents and RF-power as a function of the LO-power.

the radio frequency P_{RF} rises linearly with the level of the external local oscillator P_{LO} until its saturated around 6 dBm of input power. There is a small dip at 0.5 dBm which differs from the linearity which is not yet understood.

Measurements of bias currents and their dependence on different input variables are a helpful tool to spot weaknesses or malfunctions in specific stages of a complex circuit. These measurements can be used to verify the correct operation of the chip under development and to compare with simulations of the circuitry. The aforementioned program to monitor and control the power supplies is well suited for this purpose.

4.2 Hittite 60 GHz Transceiver Evaluation Kit

The second transceiver evaluation kit at disposal is used for the setup of the wireless data transmission reference system. It is the HMC6451 transceiver evaluation kit from Hittite² consisting of two HMC6000 transmitter and two HMC6001 receiver chips. Both pairs are mounted on individual evaluation boards such that two independent wireless links can be set up. The chipsets use SiGe BiCMOS technology. The output signal is provided via a single MMPX connector. A picture of the transceiver kit is shown in Figure 4.4.

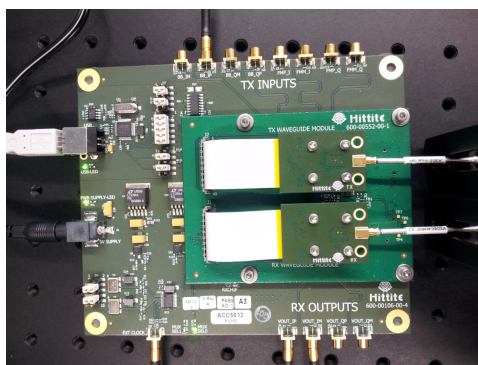


Figure 4.4: The Hittite HMC6451 60 GHz evaluation kit

For the generation of the carrier frequency either internal oscillators or an external reference can be chosen. Different parameters like the carrier frequency provided by PLLs³ and programmable attenuations in the intermediate frequency or baseband stage can be set using the slow control software provided by Hittite. The transmitter features IQ modulation and has dedicated inputs connected to inverters that are used for MSK. The receiver recovers the baseband IQ signal from the RF. Parallel it also features detectors for frequency modulated (FM) and amplitude modulated (AM) signals. The FM discriminator is used for the non-coherent demodulation of the MSK signal. A block diagram of the transmitter and receiver is shown in Figure 4.5.

Both transmitters and receivers feature an intermediate frequency bandwidth of 1.8 GHz. The radio frequency spectrum of the transmitter is shown in Figure 4.6(a). The spectrum of the receiver's baseband output is shown in Figure 4.6(b). Compared to the planned chip design, the IF bandwidth of the Hittite transceiver is smaller, but it can be operated in different frequency channels as it incorporates a more complex frequency synthesiser. The power consumption of the transceiver was measured to be about 4.5 W including the full evaluation board which itself consumed 1.4 W without any transmitter or receiver mounted. The power consumption was measured during a wireless data transfer at 1.76 Gbps using the MSK option of the transmitter and the FM demodulator in the receiver. The MSK option was used because it offered the possibility of transferring data without the need for digital to analog converters and a large external baseband

²www.Hittite.com

³PLL = Phase Locked Loop

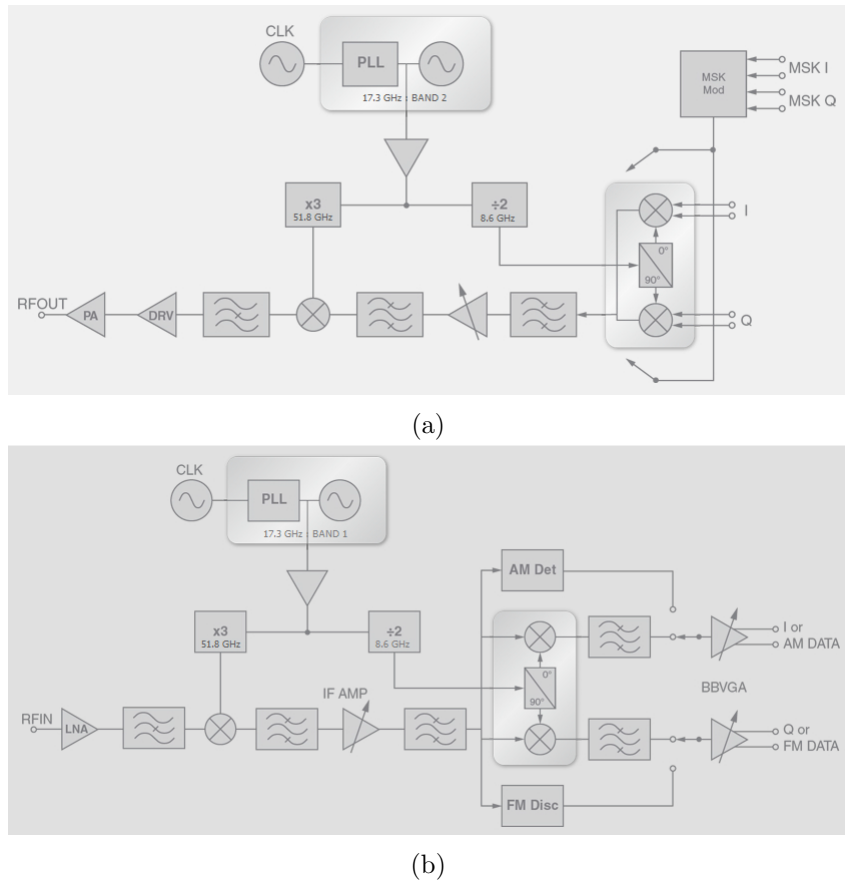


Figure 4.5: Block diagram of the Hittite (a) transmitter and (b) receiver. Taken from the control software.

circuitry to track the phase between transmitter and receiver.

Moreover, a phase drift between transmitter and receiver was observed when sine waves were transferred using analogue IQ modulation. Already Petersen described this effect [34] which can now be explained by non-linearities in the power and low noise amplifiers that are strongly influenced by temperature variations. With this transmitter and receiver pair IQ modulation can therefore only be used reliably if ADCs are applied to track the phase between transmitter and receiver permanently. The phase drift is illustrated in Figure 4.7. A 150 MHz sine wave was applied to the baseband Q-input of the transmitter only, baseband I was not connected. In the IQ constellation diagram this corresponds to a single line along the Q-axis (see Figure 4.7(a)). The receiver's output was permanently drifting generating a circle in the receiver's output constellation diagram (see Figure 4.7(b)). The drift occurred on a time scale of about 90° per minute.

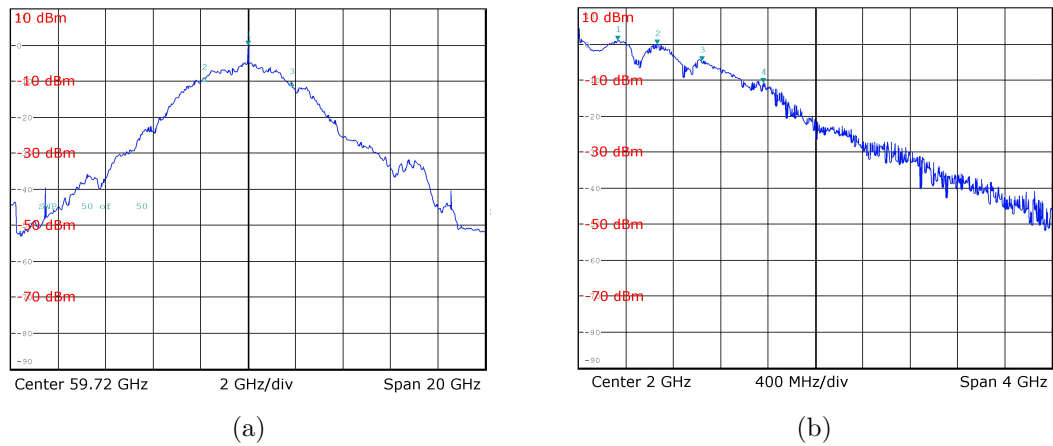


Figure 4.6: IF-bandwidth of the Hittite transceiver. (a) Radio frequency spectrum of the transmitter. (b) Baseband spectrum of the receiver.

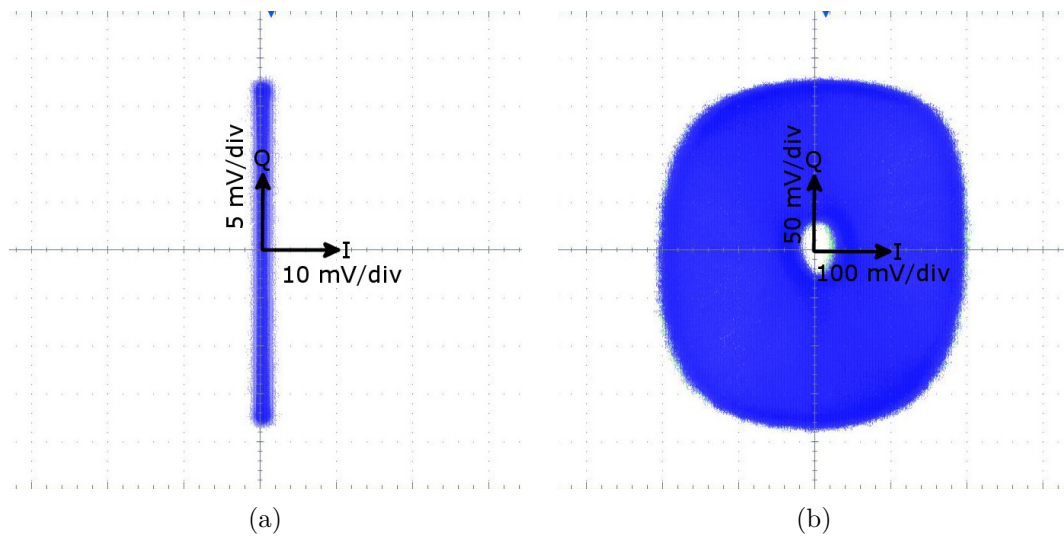


Figure 4.7: Phase drift of the Hittite wireless link using baseband IQ-modulation. (a) Transmitter baseband input: Q vs I; Q: 150 MHz sine wave, I: not connected. (b) Receiver output: Q vs I; Phase drift creates circle in IQ constellation diagram .

5 Crosstalk Suppression

The successful implementation of a readout system consisting of thousands of wireless links in a comparatively small volume like the ATLAS tracker can be achieved only if crosstalk can be controlled [7]. A simulation by Hogle [35] using a ray tracing program has shown that a stable wireless data transfer system in a tracker cannot be established without taking care of crosstalk induced by reflected waves. This chapter presents a set of measurements that have been performed in order to address this problem.

The first part of this chapter takes up the idea of a highly directional aluminised Kapton horn antenna which has first been presented by Petersen [34]. A smaller version of this antenna has been built and tested regarding gain and beamwidth. In addition to using the directivity of antennas one can also exploit their polarisation. Therefore this section also presents polarisation measurements for different antennas. For this purpose a polarising filter has been produced by laser ablation of aluminised Kapton foil. The second part focuses on material studies. They have been conducted to analyse the reflective and transmitting behaviour of materials typically used in tracking detectors in the millimetre wave regime. In addition graphite foam has been investigated because it is a material commonly used for absorbing microwaves [42] but whose properties at 60 GHz have not been tested sufficiently so far. First measurements were performed by Petersen [34] and first simulations were performed by Hogle who could demonstrate that crosstalk is reduced by shielding the transceivers with a fully absorbing material [35]. In the last part of this chapter experiments are described which have been conducted to quantify the expected crosstalk and the influence on the signal to noise ratio of the approaches mentioned above. It includes a test using different frequency channels with limited bandwidth in the 60 GHz band.

5.1 Characterisation of Antennas

In any area of application for wireless communication systems it is common practice to use antennas for transmitting and receiving radio signals. For the implementation of a wireless tracker readout directive antennas are not only necessary to establish the data transfer but they can also reduce crosstalk. Therefore the directivity of the antennas must be sufficiently large and the beamwidth consequently small. The form factor of antennas operating at 60 GHz is very small because of the small wavelength. This allows for high directivity with small structures of the order of milli- to centimetres.

In the following paragraphs constraints on antennas for the wireless readout system are derived from the current ATLAS tracking detector's geometry. The full detector has a cylindrical shape and consists of three layers. Each layer is formed by several detec-

tor modules which are tilted by about 11° with respect to each other [43]. For this model calculation the modules' surfaces are assumed to be flat. Assuming a distance between two layers of about $r = 10$ cm and assuming the transmitters to be placed about 10 cm next to each other the antennas' 3 dB beamwidth z on the surface should be substantially smaller than 10 cm. The beamwidth is typically given in degree, starting from a measurement with fixed distance r . Its angle is denoted by α . As we are interested in the beamwidth, on a flat surface at a small distance, the signal emitted under the angle α has to travel an extra distance y with respect to a circular geometry to reach the surface. This distance induces further path loss according to the Friis transmission equation (see Equation 2.25). On the surface the intensity drops by 3 dB under the emission angle β instead of α . The discussed geometry is illustrated in Figure 5.1(a).

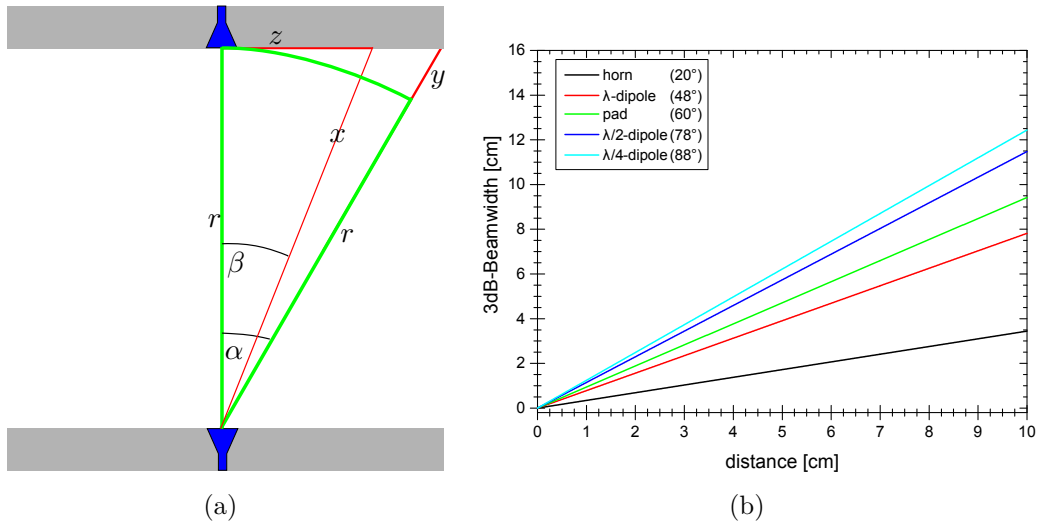


Figure 5.1: (a) Geometry of the tracker model for the 3 dB beamwidth correction by applying Friis equation for a Gaussian intensity profile. α yields -3 dB at distance r ; β yields -3 dB at the layer's surface.
(b) Beamwidth in cm as a function of distance

The angle β should now be calculated. It muss fulfill

$$I(\beta) \stackrel{!}{=} I(0) - 3 \text{ dB}, \quad (5.1)$$

which means that the intensity on the surface emitted under this angle $I(\beta)$ is 3 dB less than the maximum intensity $I(0)$. A Gaussian shape of the radio beam is further assumed where α equals the FWHM¹, i.e. $\alpha = 2\sqrt{2 \ln 2} \sigma$. The following equation has to be evaluated to obtain the angle β :

$$\Rightarrow 10 \text{ dB} \log \left(\exp - \frac{\beta^2}{2\sigma^2} \right) + 20 \text{ dB} \log (\cos \beta) \stackrel{!}{=} -3 \text{ dB}, \quad (5.2)$$

where the first term is the result of the Gaussian shape and the second term takes

¹FWHM = Full Width at Half Maximum

the additional path loss along y following from the Friis transmission equation into account. This correction term is almost negligible for antennas with small beamwidth. For a highly directive antenna, like a horn antenna with an estimated beamwidth of $\alpha_{horn} = 20^\circ$, the correction is very small (corrected beamwidth $\beta_{horn} = 19.5^\circ$). But for less directive antennas this term becomes more dominant. For example for a $\lambda/4$ -dipole the influence is very large ($\alpha_{\lambda/4} = 88^\circ, \beta_{\lambda/4} = 63.8^\circ$).

Figure 5.1(b) shows the calculated beamwidth in cm for different antennas according to their typical beamwidth in degree. The beam dispersion can be reduced by about a factor of 4 if a highly directive antenna is applied with respect to a small $\lambda/4$ -dipole. The advantage of horn antennas is that they can be produced easily and offer a high frequency bandwidth for operation, but they would extend into the space between the layers. Therefore the wireless link distance between transmitter and receiver would be decreased. One could also think of using flat patch array antennas which do not extend into the space between the layers, however they typically have a smaller bandwidth and the production process is more complex. An example for such an antenna is presented in [44] with a gain of 11.0 dBi achieved, though operating at higher frequencies around 79 GHz. An example for a planar directive antenna operating at 60 GHz can be found in [45] with a reached gain of 23 dBi over a bandwidth of 2 GHz.

5.1.1 Near Field Effects

As Friis transmission equation has been used it was implied that the receiver will be placed in the far field of the transmitter. This holds for small antennas like a single pad antenna (size about 1 mm^2) or a dipole (length $l = \lambda = 5 \text{ mm}$) as the Fraunhofer distance [46]

$$d_f = \frac{2D^2}{\lambda}, \quad (5.3)$$

where D is the largest dimension of the antenna, is well below 10 cm. For a comparable large antenna like the horn presented in [34] with an aperture of $1.85 \times 1.28 \text{ cm}^2$ the Fraunhofer distance is of the order of 10 cm. A horn antenna also would extend into the space between the tracking detector layers (this one about 4.5 cm), therefore reduce the distance between the antennas to much less than 10 cm so that near field effects emerge. A measurement of the received intensity at 58.3 GHz depending on the distance between two 20 dBi brass standard gain horns performed with a spectral analyzer by Rohde&Schwarz proves that near field effects are measurable up to distances of $r \approx 5 \text{ cm}$ which result in oscillations (see Figure 5.2). This region is therefore called transition region between the immediate near field ($r \leq \lambda$) and the far field. At distances $r > 10 \text{ cm}$ the intensity follows Friis transmission equation and drops accordingly with r^{-2} .

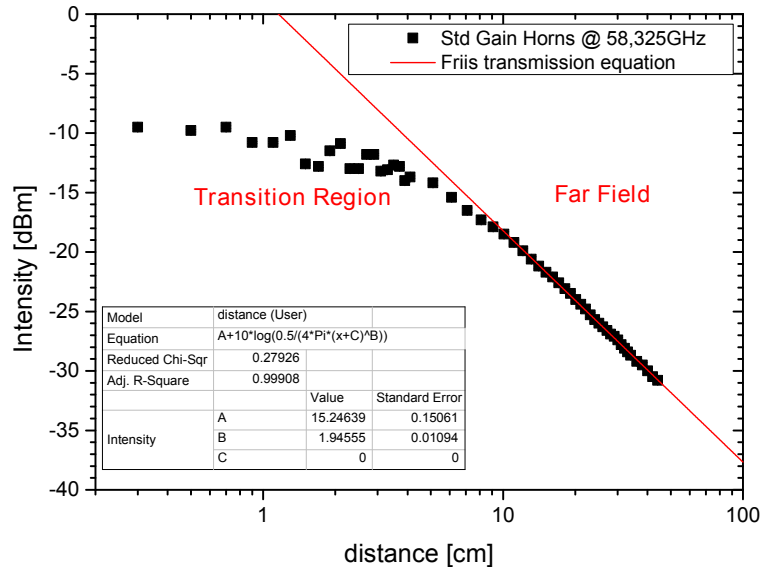


Figure 5.2: Intensity as function of the distance between transmitting and receiving brass horn antennas. Zoomed into the transition region between the near field ($r \leq \lambda$) and the far field ($r > d_f$) where the near field effects are noticeable.

5.1.2 Polar Pattern Simulation of Horn Antennas

A first model of a highly directive horn antenna with a length of 4.5 cm folded from aluminised Kapton foil has been presented in [34]. The foil was $60 \mu\text{m}$ thick in total, consisting of $35 \mu\text{m}$ Kapton and $25 \mu\text{m}$ aluminum. The antenna showed a reasonable directivity compared to an industrial manufactured brass horn. As the size of this antenna may be too large for the short range application over 10 cm a shorter antenna prototype has been built. In order to find antenna dimensions which still provide a sufficiently high directivity a simulation of the far field radiation of horn antennas with different lengths has been conducted using an evaluation version of the FEKO² electromagnetic simulation software. Figure 5.3 shows a simulated 3-dimensional intensity pattern of a horn antenna.

The length of the simulated antennas has been varied from 45.4 mm down to 20.4 mm in steps of the wavelength at 60 GHz $\lambda = 5 \text{ mm}$ whereas the aperture has been downscaled correspondingly. In the simulation directivity equals gain as the efficiency is set to be $\eta = 1$. The simulated gain of a 35.4 mm long horn antenna as function of frequency is shown in Figure 5.4. For all antennas the gain is increasing with frequency. The gain of the antennas in the simulated frequency range at 55 and 65 GHz are listed in Table 5.1.

From the simulated radiation pattern the 3 dB-beamwidth can be extracted. The results in both H- and E-plane are depicted in Figures 5.5(a) and (b). The focusing power of the antenna is decreased if its length is reduced. This can be seen in gain and beamwidth. While the maximum gain is decreased by only 0.8 dB scaling the antenna from 45 mm

²<http://www.feko.info>

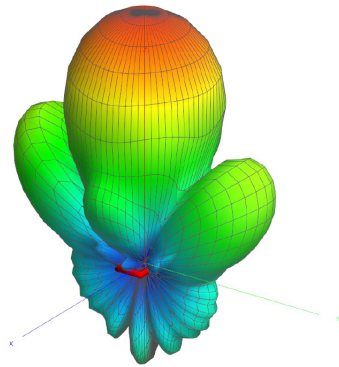


Figure 5.3: Simulated radiation pattern of a 35.4 mm long horn antenna at $f = 60$ GHz

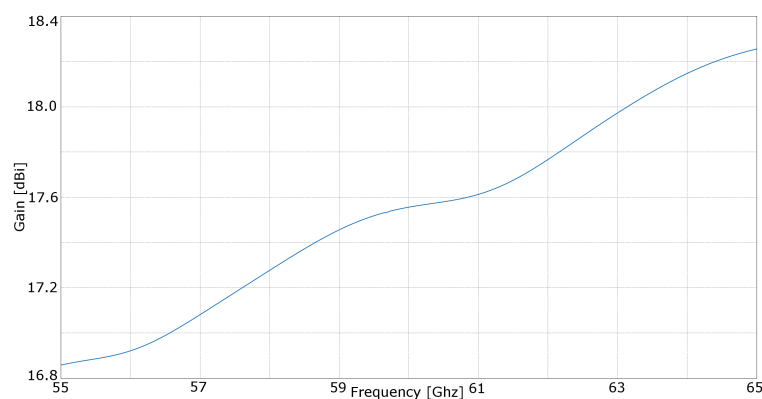


Figure 5.4: Simulated gain vs frequency of a 35.4 mm long horn antenna

down to 40 mm length, the loss is twice as large by reducing its length from 25 mm to 20 mm (1.6 dB). Correspondingly the beamwidth is increasing more rapidly by shrinking the antenna more and more. As the beam is already more focused in the H-plane its dispersion in the E-plane is influenced more strongly by the antenna's length. In addition, the frequency dependence grows by downscaling the antenna so that its properties are not as constant anymore in the simulated spectral bandwidth.

A reasonable trade-off between length and directive properties seems to be 35 mm as the directivity is reduced by less than 2 dB and the beam is still concentrated in a cone with an opening angle smaller than 30° through the analysed frequency band. Figure 5.6 shows the produced 35 mm long Kapton horn antenna in a flange and a 45 mm long brass gain horn³ as comparison partner. In the following the properties of the Kapton horn antenna are measured.

³Flann Standard Gain Horn Model-Nr. 25240-20

Antenna length [mm]	Gain [dBi] ($f = 55$ GHz)	Gain [dBi] ($f = 65$ GHz)
45.4	18.7	20.1
40.4	17.9	19.3
35.4	16.9	18.3
30.4	15.6	16.9
25.4	14.0	15.5
20.4	12.3	13.9

Table 5.1: Simulated gain of ideal horn antennas with different length. Properties of the new prototype are highlighted.

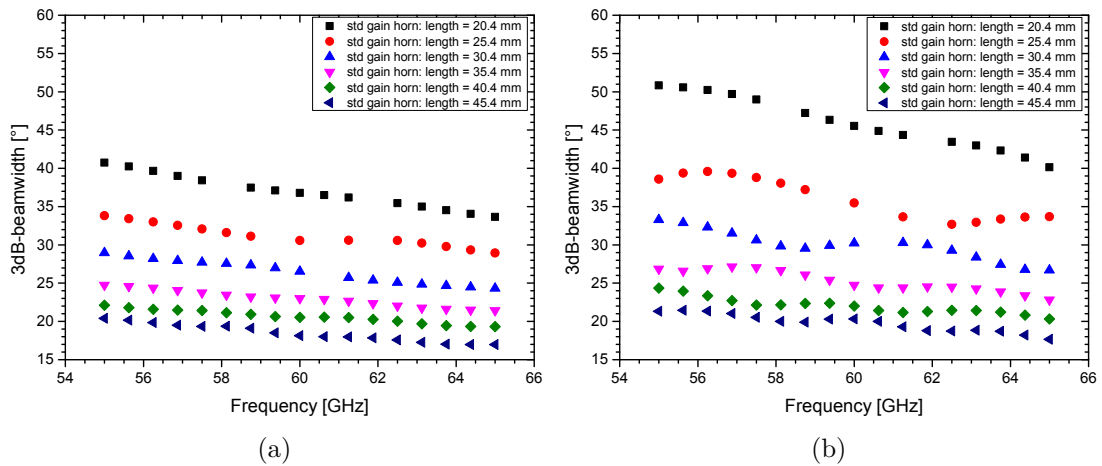


Figure 5.5: Simulated beamwidth of horn antennas with different length in the (a) H-plane and (b) E-plane



Figure 5.6: Aluminium Kapton horn antenna and brass standard gain horn

5.1.3 Directivity Measurements

The setup for the characterisation of the 35 mm long Kapton horn antenna is depicted in Figure 5.7. The antenna under test has been placed in the middle of a rotary table where a receiving brass horn antenna was mounted on. The distance between the antennas was chosen to be 14 cm so that near field effects would not distort the measurement. In order to obtain both planes' beamwidth the antennas were rotated by 90° .

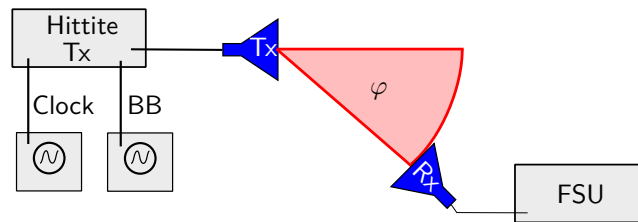


Figure 5.7: Measuring the polar pattern by rotating the receiving brass gain horn around the transmitting antenna under test. The intensity has been measured with the spectrum analyser (FSU). Clock and baseband (BB) signals for the Hittite 60 GHz transmitter have been provided by Anritsu MC3692 signal generators.

Measured Polar patterns are shown in Figure 5.8(a) and (b). For comparison the pattern of the 4.5 cm long Kapton horn antenna from [34], the brass standard gain horn and a 1 mm^2 pad antenna are included in these plots. As the pad antenna was connected to a Gotmic TXQ060A01 transceiver chip it was the only measurement not conducted with the Hittite transceiver kit. One can see that the smaller horn antenna is still very directive and the pattern is compatible to the larger Kapton and brass horn antennas. A small imperfection in the aperture's shape results in an angular deviation of the beam direction in the H-plane. Side lobes in the E-plane are induced by the rectangular shape of the aperture. The pad antenna has a very broad angular transmission pattern, especially in the E-plane, and therefore only a small gain.

Gain and beamwidth of the 35 mm long Kapton horn antenna together with the 45 mm long horn from [34] and the pad antenna at different frequencies are plotted in Figures 5.9 and 5.10. The uncertainties of the measurements are related to variations of the intensity. On the one side the output power of the transmitter was not constant in time and also dependent on the temperature. On the other side the measurement setup was sensitive to bending of the coaxial cables which were used to connect the receiving antenna to the spectrum analyser. The precision of the analyser itself was sufficiently high down to low intensities. The observed variations increased with decreasing intensity. The uncertainties taken into account are of the order of 0.05 dBm to 0.30 dBm for intensities between 10 dBm and -60 dBm. Below this value the measured variations increased strongly and maximum errors up to 2.0 dBm at levels of less than -90 dBm are used. The measurements were performed using the option of the spectrum analyser to average over a sample of 50 measurements. The uncertainties of the gain include the variations of the measured intensity and of the normalisation intensity. The latter is

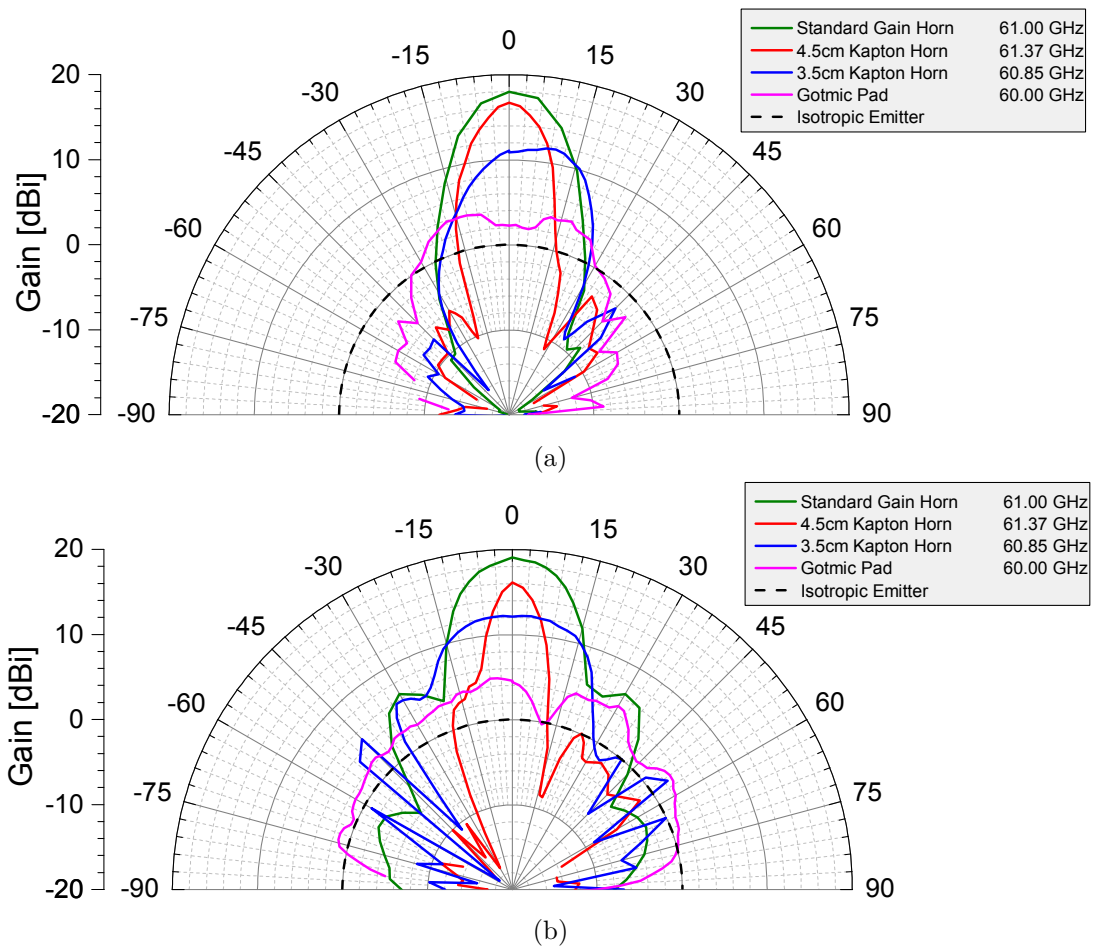


Figure 5.8: Polar patterns measured for horn and pad antennas in the (a) H-plane and (b) E-plane. 4.5 cm Kapton horn data taken from [34].

composed of the uncertainty of the total transmitted power and the distance between transmitting and receiving antenna which is of the order of 2%. The uncertainty of the beamwidth includes in addition the uncertainty of the angular measurement which is negligible compared to the intensity variations.

The gain of both Kapton horns is comparable. This means that the smaller horn has a higher efficiency because the directivity of the longer horn should in general be higher as the simulation showed. It can be attributed to a better connection of the smaller horn as it was connected with a flange to the waveguide adapter whereas the 45 mm horn was tested with a cardboard connection [34]. On average the gain rises with frequency. It is between 13.6 dBi at 55.7 GHz and 16.7 dBi at 64.5 GHz, so the total rise is steeper than simulated. Between 59.2 GHz and 62.4 GHz the gain is decreasing from 15.7 dBi down to 13.6 dBi. This could be related to an impedance mismatch, but it is not yet understood completely.

Regarding beamwidth the 35 mm Kapton horn shows a stronger frequency dependence

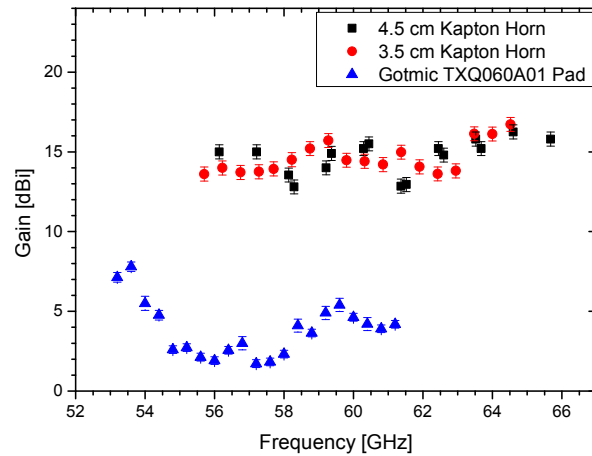


Figure 5.9: Gain of the pad antenna and the Kapton horn antennas

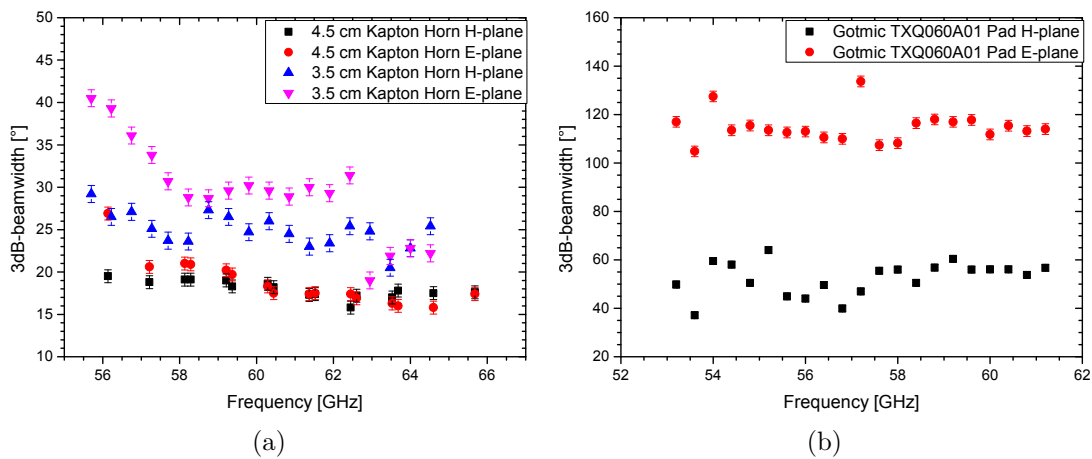


Figure 5.10: Beamwidth measurements of the (a) Kapton horn antennas and (b) pad antenna

than the simulated model, especially in the E-plane. The width drops more than 10° from 56 GHz to 58 GHz. Above this frequency it is stable around 30° up to about 63 GHz. There is a discontinuity which is probably caused by a similar reason as the loss of gain. Again, this is not yet completely understood. In the H-plane the average beamwidth is about 25° from 58 GHz to 64 GHz.

The pad antenna under test has a much smaller gain compared to the horns. It depends strongly on frequency below 58.5 GHz. Above it is rather stable up to 61.5 GHz. The variations may be accounted to the impedance bandwidth of the pad antenna which is smaller than that of horn antennas. The pad antenna is designed for a frequency of 60 GHz and the bandwidth is limited to a few GHz, whereas horn antennas can principally be operated over more than one magnitude of frequency. Measurements at higher frequencies were not possible due to the malfunction of the Gotmic transmitter's mixer as stated in Chapter 4.

The beamwidth of the pad antenna in the E-plane is quite stable through the whole frequency spectrum tested. In the H-plane there are strong relative variations below 58.5 GHz. Above this frequency the beamwidth is quite constant. Average values for the beamwidth are $52 \pm 7^\circ$ in the H-plane and $115 \pm 6^\circ$ in the E-plane.

In conclusion, it is possible to produce directive horn antennas using little material by folding aluminised Kapton foil. The new antenna was downscaled by 22% of the size of the prototype presented in [34]. It has a high gain of 13.6 to 16.7 dBi and a beamwidth smaller than 30° from 58 to 64 GHz. This beamwidth corresponds to a beam dispersion of less than 5.1 cm at a distance of 10 cm in the aforementioned tracker model.

5.1.4 Analysis of Polarisation

Polarisation can be very helpful to reduce crosstalk. In the ideal case of two links next to each other using orthogonal, linear polarisations there should be zero crosstalk. This section shows how well orthogonally polarised waves can be suppressed in reality. The polarisation of an antenna is the same as the polarisation of the waves it emits or receives. A proper linear polarised antenna amplifies one polarisation component and attenuates the orthogonal one. Like this the degree of polarisation is increased. In this work two setups have been developed for measuring the polarisation of the antennas under test.

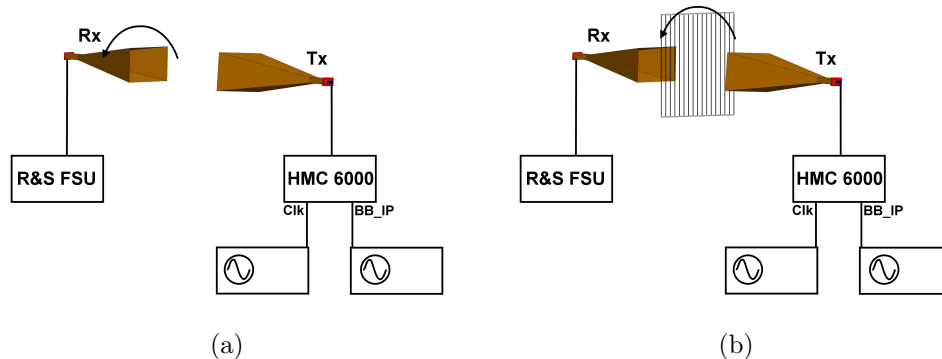


Figure 5.11: Polarisation measurements' setup. (a) Rotation of receiving antenna. (b) Rotation of polarising filter. FSU = spectrum analyser; BB = Baseband

Figure 5.11(a) illustrates the first setup. The receiving antenna is rotated along the transmission axis and the intensity is measured with the spectrum analyser. The second setup (see Figure 5.11(b)) used fixed antennas for transmission and reception while a wire grid polarising filter has been placed in between. The principle of a grid polariser can be found in [47]. A view of the latter setup in the laboratory can be seen in Figure 5.12(b). Rotation of the polariser filters the component of the electric field parallel to the grid. The filter has been made of the same aluminised Kapton foil as the antennas. For the generation of aluminum strips which are not electrically connected aluminum has been ablated from the foil in a grid pattern with a laser. In that way the filter is

stabilised by the remaining Kapton layer. A microscopic view of the filter can be seen in Figure 5.12(a). The pitch of the strips is about $500\ \mu\text{m}$ where the width of each strip is approximately $450\ \mu\text{m}$ and the lasered lines are about $50 \pm 10\ \mu\text{m}$ thick. Moreover, a simple flat ribbon cable has been tested as polariser as well. Its wire pitch was $1.25\ \text{mm}$, so still below the wavelength, but problems concerning the tension of the wires led to the preference for the filter produced via laser ablation.



Figure 5.12: (a) Microscopic view of the polarising filter produced via laser ablation. (b) Setup mounted in the laboratory - back view of the polariser.

Dealing with linear polarised antennas the rotation of one antenna by the angle α with respect to the other should lead to an intensity behaviour following a $\cos^2(\alpha)$ as the antenna itself acts as a polarising filter. Putting the polariser in between yields another factor of $\cos^2(\alpha)$ which results in a dependence on the angle between polariser and antenna of $\cos^4(\alpha)$. This follows from geometry and the fact that the intensity is proportional to the squared absolute value of the electric field. A detailed treatment can be looked up in [9] and [47].

The 60 GHz signal has been coupled from the Hittite transmitter into the antennas using waveguide to coaxial adapters from Ducommun except for the pad antenna which was directly connected to the Gotmic chip. This pad antenna could also be used as a feed for the horn antennas.

The angular intensity dependence for the combination of a 4.5 cm long Kapton horn antenna and a brass standard gain horn is illustrated in Figure 5.13. The uncertainties of the data are dominated by intensity variations which have been described in Section 5.1.3. The uncertainty of the angle is about 1° . A $\cos^2(\alpha)$ fit has been performed which describes the data very well. The fit parameters can be extracted from this plot. Table 5.2 contains the results of the antenna rotation measurement. The maximum intensity suppression is represented by ΔI_{max} . The corresponding angle between the antennas is denoted by α_{max} . By means of directive horn antennas the orthogonal polarisation component can be highly suppressed. Using the brass gain horns on both transmitter and receiver a suppression of more than 50 dB is achieved which seems to be an upper

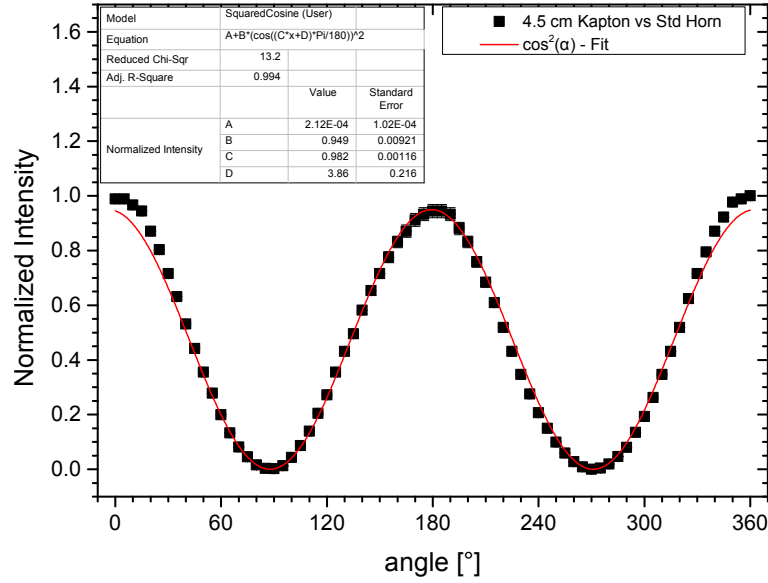


Figure 5.13: Data taken by rotating Kapton horn antenna with respect to a brass horn; a $\cos^2(\alpha)$ - fit is applied.

limit. With a 4.5 cm long Kapton antenna on the transmitter side the suppression is lower but still more than 30 dB with a brass horn on the receiving end. The smaller 3.5 cm Kapton horn antenna behaves worse. Its orthogonal component is suppressed by only 14.8 dB with a brass horn on the receiving end, which is less compared to the waveguide. This may be caused by the same imperfections which led to the small angular shift of the directed beam. A more sophisticated production process could help to increase this value. Operating the pad antenna as a feed the suppression with the standard gain horns could be reproduced.

Tx Antenna	Rx Antenna	ΔI_{max} [dB]	α_{max} [°]
Waveguide	Waveguide	-10.7 ± 0.6	80 ± 2
Waveguide	Std horn	-19.2 ± 0.6	80 ± 2
Std horn	Std horn	-53.8 ± 1.0	90 ± 2
Kapton 3.5 cm	Std horn	-14.8 ± 0.4	95 ± 2
Kapton 4.5 cm	Std horn	-33.2 ± 0.6	90 ± 2
Kapton 4.5 cm	Kapton 3.5 cm	-13.5 ± 0.4	85 ± 2
Gotmic pad	Std horn	-18.7 ± 0.9	80 ± 2
Gotmic pad + Std horn	Std horn	-50.0 ± 1.1	100 ± 2

Table 5.2: Intensity suppression by rotation of antennas

Figure 5.14 shows an exemplary measurement with the polarising filter rotated between the transmitter and receiver antenna which were fixed at zero relative angle. Regarding uncertainties the aforementioned intensity variations are the dominating error source. The data can be well described by a $\cos^4 \alpha$ - fit. The fit parameters can be extracted

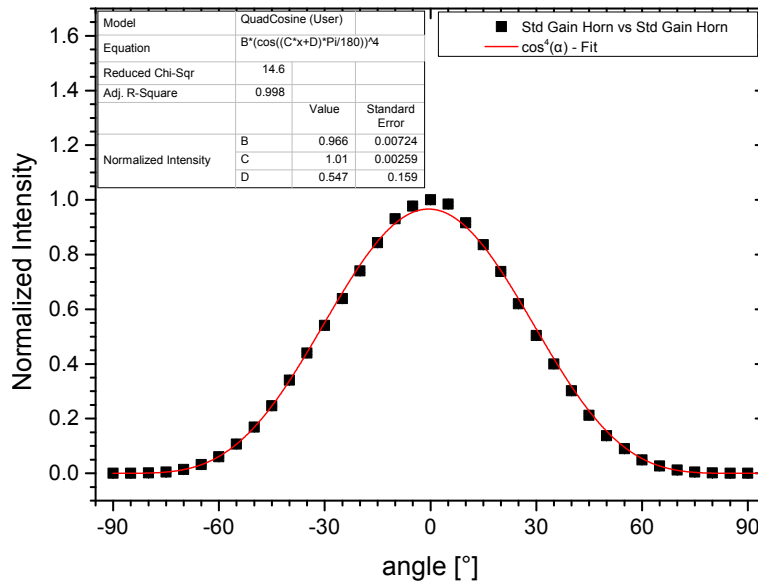


Figure 5.14: Data taken by rotating aluminised Kapton polariser between brass horn antennas and applied $\cos^4(\alpha)$ - fit

from the plot. Table 5.3 summarises the measurements with the same antenna installations as for the measurement before. Again, the measured maximum intensity difference is denoted by ΔI_{max} . In all cases except for the standard gain horns applied on both sides the orthogonal component is even more suppressed. Even with both Kapton horn antennas applied the polariser leads to a suppression of more than 30 dB if it is aligned parallel to the electromagnetic field component.

Tx Antenna	Rx Antenna	ΔI_{max} [dB]
Waveguide	Waveguide	-28.9 ± 0.6
Waveguide	Std horn	-47.0 ± 0.6
Std horn	Std horn	-56.0 ± 1.0
Kapton 3.5 cm	Std horn	-43.5 ± 0.4
Kapton 4.5 cm	Std horn	-42.0 ± 0.6
Kapton 4.5 cm	Kapton 3.5 cm	-33.5 ± 0.4
Gotmic pad	Std horn	-33.3 ± 0.9
Gotmic pad + Std horn	Std horn	-50.7 ± 1.1

Table 5.3: Intensity suppression with the help of polarising filter

In conclusion it can be stated that highly directive antennas can be built easily by folding aluminised Kapton horns and are therefore of low cost and little material. As the antennas are very sensitive to deformations the production process could definitely be improved to achieve an even more stable behaviour across the 60 GHz frequency band, though the results are very promising. Regarding polarisation the longer Kapton horn performed better than the shorter one whereas neither of them could reach the degree

is a very low density material. Measurements yield an average of the four foams of $59 \pm 10 \text{ mg/cm}^3$ which leads to a large radiation length of approximately $7.7 \pm 0.6 \text{ m}$ under the assumption that the radiation length of polyethylene $X_0 = 44.77 \text{ g/cm}^2$ [48] can be applied. The latter has been chosen because the foam is only impregnated with carbon and its main component is synthetic foam. This yields $0.13 \pm 0.01 \%$ of radiation length per centimetre of foam.

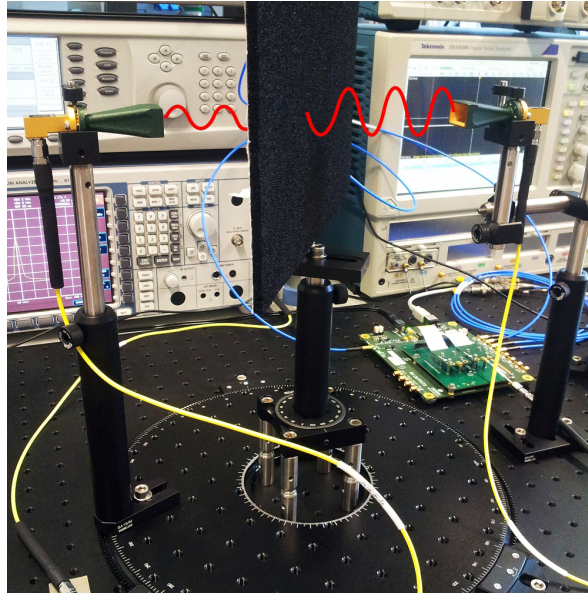


Figure 5.16: Setup in the laboratory: graphite foam sample between two horn antennas. Polarisation perpendicular to the incident plane.

The setup of the reflection and transmission measurements in the two following subsections is illustrated in Figure 5.15. The receiving antenna was mounted on a rotary table. In its centre a second rotary platform was placed which held the material samples under test. Tests have been performed with linearly polarised waves. Both polarisations parallel and perpendicular to the incident plane have been analysed separately. The setup in the laboratory using perpendicular polarised waves is shown in Figure 5.16. A baseline measurement without sample yields limits on the angular range which could be used for fitting of the reflectivity data. Besides, it can be used for normalising the data.

In the following the polarisation of the waves corresponds to the orientation of the antenna's E-plane with respect to the incident plane as the measured intensities depend on the electric field of the waves. For parallel polarisation the E-plane and the incident plane coincide, for perpendicular polarisation the planes are orthogonal.

For waves polarised perpendicularly to the incident plane the range from 6° to 70° is well suited to perform fits, whereas for parallel polarised waves the angular range is limited from 4° to 70° . Smaller angles were not possible due to the setup. At larger angles the direct signal from the transmitting antenna interfered with the reflected one.

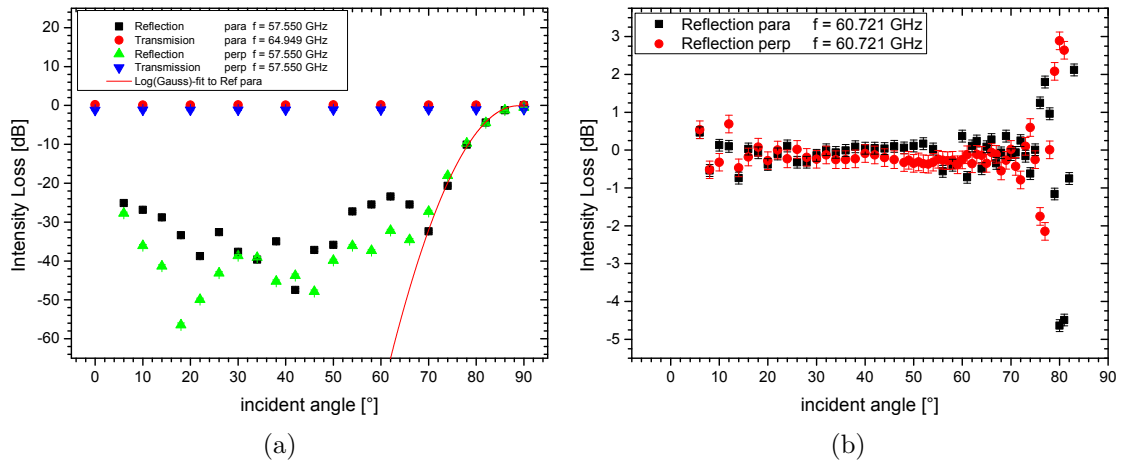


Figure 5.17: (a) Baseline measurement for reflection and transmission using parallel (para) and perpendicularly (perp) polarised waves. A Gaussian fit has been performed to the beam profile for parallel polarisation. (b) Reflection reference measurement with 2 mm thick aluminum sample.

This also happened during the transmittance measurement when the sample was too small. The baseline measurement and the aluminum reference result over the angular range are depicted in Figure 5.17(a) and (b). The reflectivity measurement of the aluminum plate proves the quality of the setup as the reflection coefficient of aluminum is 1. Only small deviations in the reflected intensity of 0.4 dB at the maximum have been detected in the angular range from 15° to 67° for perpendicular polarisation and 15° to 55° in the parallel case. These small deviations are acceptable for the setup. One can see the Gaussian beam profile in the baseline measurement at large incident angles and the resulting interference pattern in the aluminum reference setup.

Differences in the reflection baseline measurement are induced by the different radiation patterns of the antennas in the E- (corresponding to parallel polarisation) and H-plane (perpendicular). The error bars are too small to be displayed in the baseline measurement. The uncertainties are again dominated by the time-dependent variations of the measured intensity. The angular uncertainty is less than 1° .

5.2.1 Reflectivity and Transmittance of Aluminised Kapton and Silicon

Different materials typically used in tracking detectors have been tested with respect to their reflectivity and transmittance in the 60 GHz frequency band. These measurements are useful to quantify the crosstalk expected in the detector. Values like the index of refraction can be applied to simulations to generate a precise model of a wireless read-out system. In this section the results of the measurements for the following samples are presented: a thin aluminised Kapton foil ($25 \mu\text{m}$ Kapton metallised with 50 nm aluminum), a $730 \mu\text{m}$ thick silicon wafer with test structures with a diameter of 12" and a silicon wafer thinned down to approximately $50 \mu\text{m}$. Figure 5.18 shows the three utilised samples. The Kapton foil has been tested because it is the base material for flexible

circuits. The thinned silicon wafer has been used because there are new silicon detector technologies that can be thinned down to this size [49]. The second silicon wafer with traces has been tested to analyse the influence of structures on the transmitted and reflected intensity.

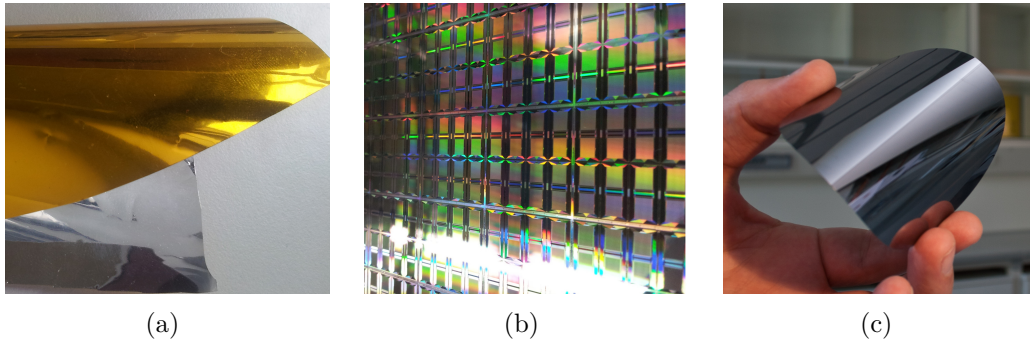


Figure 5.18: Samples for reflectivity and transmittance measurements:

(a) 25 μm Kapton foil with 50 nm aluminum, (b) 730 μm silicon wafer with test structures and (c) 50 μm silicon.

The reflected and transmitted intensity are normalised to the power sensed by the receiving antenna at 0° incident angle without any sample in between. As both foil and thinned silicon were mounted with an additional cardboard holder another baseline measurement including this mounting had to be performed for normalisation. The aluminised foil itself served as a reference for the reflectivity measurement of the thin silicon wafer. The reflected and transmitted intensity have been measured for both polarisations at a single frequency of $f = 60.721$ GHz generated by the Hittite transceiver using an external reference of 302 MHz and a double sideband baseband signal of 1 GHz in the same manner as for the antenna characterisations. A fit of the Fresnel equations (see Equations 2.13 to 2.16) with a complex index of refraction was applied to suitable data only which is the case for the 50 μm silicon sample and certain data from the 730 μm wafer.

The data of the aluminised Kapton foil is depicted in Figure 5.19(a). The 50 nm of aluminum were already sufficient to generate an almost perfect reflector so there is no distinct angular dependence neither of the reflected nor of the transmitted intensity. Instead an average value for the insertion loss can be given which is about $\Delta I = -43 \pm 1$ dB at $f = 60.721$ GHz. Moreover, the reflectivity measurement can be used as a reference for the silicon test. Placing the 50 μm silicon wafer in front of the foil did neither yield any significantly different results of the transmitted nor of the reflected intensity. The average insertion loss including the silicon was about $\Delta I = -40.5 \pm 0.5$ dB which is compatible to the first result.

The transmission and reflection loss measurements of the 50 μm thin silicon wafer itself yielded data suitable to perform a fit of the reflection and transmission coefficients according to the Fresnel equations. The index of refraction could be treated to be purely

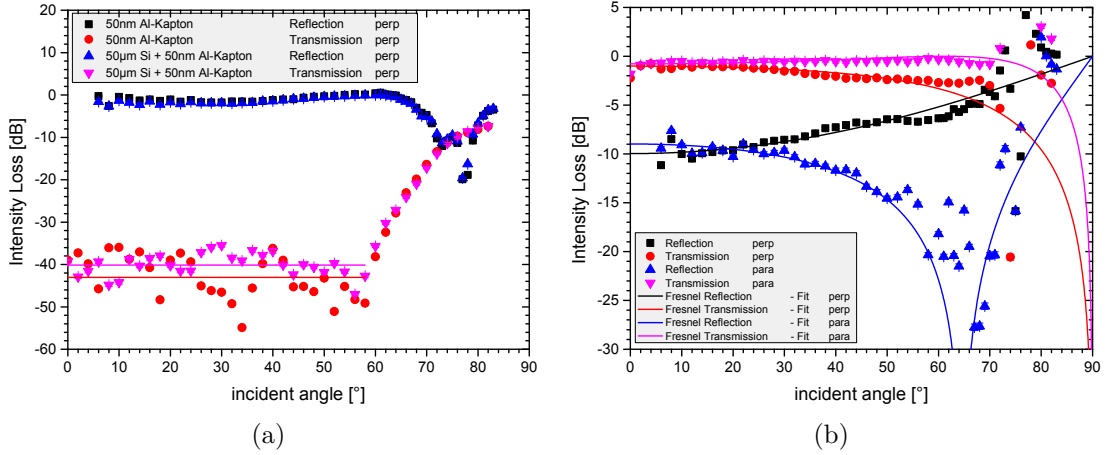


Figure 5.19: Reflection and transmission loss results. (a) 25 μm Kapton foil metallised with 50 nm aluminum using perpendicular polarised waves. Also depicted: data with 50 μm silicon wafer in front of the foil. (b) 50 μm silicon wafer using perpendicular (perp) and parallel (para) polarised waves.

real in this situation such that κ has been fixed to zero. Figure 5.19(b) presents the data taken for both polarisations at 60.721 GHz and the corresponding fits. The fit results together with their average value are comprised in Table 5.5.

Measurement	Polarisation	n	χ_{red}^2
Reflection	perpendicular	1.93 ± 0.02	12.7
Reflection	parallel	2.10 ± 0.02	5.8
Transmission	perpendicular	1.99 ± 0.03	4.2
Transmission	parallel	1.83 ± 0.04	2.0
Average		1.96 ± 0.06	

Table 5.5: Index of refraction of 50 μm silicon wafer at $f = 60.721$ GHz derived from fit functions with fixed $\kappa = 0$.

The average index of refraction of the 50 μm thick silicon wafer is about $n = 1.96 \pm 0.06$. This value differs significantly from the one expected for pure silicon $n_{Si} = 3.95$ [48]. This may be caused by the exposure to air. Typically, pure silicon oxidises and a small coating of silica ($n_{SiO_2} = 1.46$ [48]) forms. This may reduce the index of refraction of the wafer in total. The intensity passing through the 50 μm of silicon at small incident angles is reduced by about -0.63 ± 0.03 dB for parallel polarised waves and -1.04 ± 0.05 dB for perpendicular polarisation. That means that it is almost transparent.

The structures on the 730 μm thick silicon wafer led to a dependency of the reflected and transmitted intensity on the orientation of the wafer perpendicular to the incident plane. Three orientations have been used which are illustrated in Figure 5.20. The coordinate systems of the chosen orientations are rotated by 90° (no. 2 to no. 1) and 60° (no. 3 to

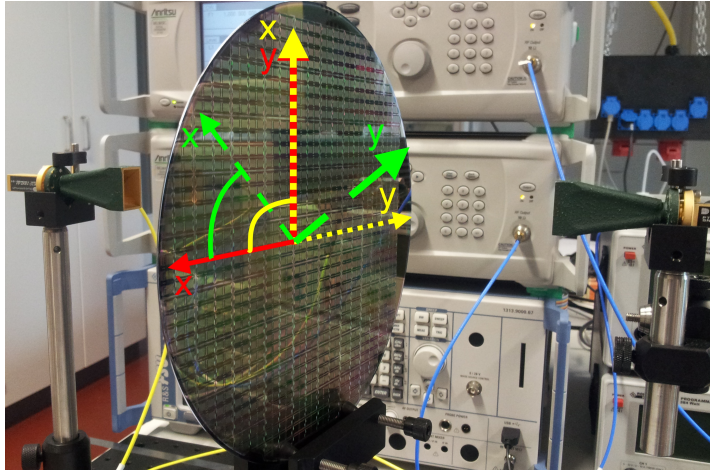


Figure 5.20: Three orientations chosen for the silicon wafer.
 Orientation 1: red, traces on the wafer vertically aligned.
 Orientation 2: yellow (depicted), 90° clockwise rotation from no. 1.
 Orientation 3: green, 60° clockwise rotation from no. 1.

no. 1) respectively.

Measurement	Polarisation	Orientation	n	κ	χ_{red}^2
Reflection	perpendicular	#1	3.41 ± 0.05	0 (fixed)	0.64
Transmission	perpendicular	#1	3.61 ± 0.42	0.68 ± 0.09	1.47
Transmission	parallel	#2	4.24 ± 0.11	0.40 ± 0.01	34.2
Average		3.75 ± 0.25	0.54 ± 0.14		

Table 5.6: Index of refraction of the $730 \mu\text{m}$ silicon wafer with test structures at $f = 60.721 \text{ GHz}$ derived from fit functions.

The reflectivity and transmittance results for both polarisations are depicted in Figures 5.21(a) to (d). The test structures lead to an effect comparable to a polarising filter. In position #1 the transmitted intensity of the parallel polarised waves is decreased under small incident angles below 20° compared to the other orientations whereas the reflected intensity is increased. For perpendicularly polarised waves the same effect occurs using orientation #2, i.e. after a 90° rotation of the wafer in the plane perpendicular to the incident one. In this plane the effect is even more distinct up to higher incident angles of about 40° . Orientation #3 therefore yields a mixture of both effects at reduced extent.

Fits have been performed to all measurements whereas the data points influenced by the filtering have been omitted. The error bars take the measured time-dependent intensity variations into account. Table 5.6 summarises the results from the fits which were best suited. These are obtained from orientation #1 for perpendicularly polarised waves and orientation #2 for parallel polarised waves for the reasons stated above. For

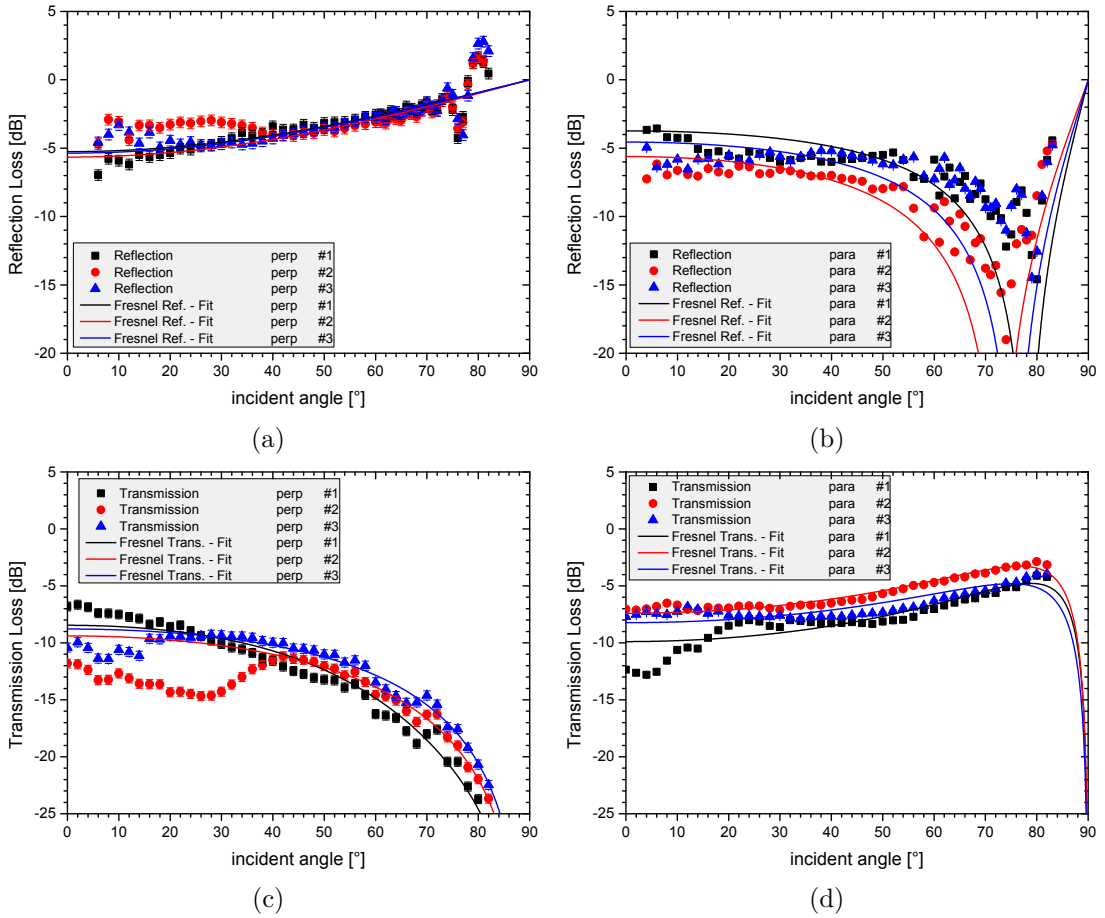


Figure 5.21: Reflection and transmission loss of a 730 μm silicon wafer with test structures at $f = 60.721$ GHz using 3 different orientations.

- (a) Reflection: perpendicularly polarised (b) Reflection: parallel pol.
(c) Transmission: perpendicularly pol. (d) Transmission: parallel pol.

the reflection coefficient of parallel polarised waves the fitting routine did not provide a stable fit result. Thus, this measurement is not included in the averaging of the results. The average value $n = 3.75 \pm 0.25$ is compatible with the literature value of $n_{Si} = 3.95$. The fits to the reflected data were performed for a real index of refraction to eliminate accidental correlations between the fit parameters. As the transmitted data is anyway more sensitive to the imaginary part by means of absorption it is deduced from these fits only. The result of $\kappa = 0.54 \pm 0.14$ shows that absorption takes place, which might be accounted for by the structures on the wafer.

Summarising it can be stated that 50 μm of silicon are almost transparent to radiation at 60 GHz. 50 nm of aluminum on a 25 μm Kapton foil instead are already enough to form a perfect reflector in this frequency range. The test of the 730 μm wafer showed that the transmitted intensity at small incident angles is reduced by about 7 dB and that traces and structures on the wafer have large influence on the reflection and transmission pattern. It is interesting to see how a real tracking detector element would behave

regarding reflection and transmission of 60 GHz radiation under different incident angles.

5.2.2 Reflectivity and Transmittance of Graphite Foam

The reflectivity of a tracking detector element is expected to be very high because of the electronics and metal construction components. The transmission coefficient of a tracking element has been determined in [7] to be around -20 dB which supports this assumption. Therefore the properties of graphite foam in the 60 GHz frequency band have been determined. So far, only the insertion loss up to 20 GHz has been specified. In the following paragraphs the results of reflectivity and transmittance measurements for the four different foams (see Table 5.4) are presented. For foam LS-11451-1 (6.35 mm thick) an analysis including frequency dependence has been performed whereas for the other three foams measurements have been conducted at a single frequency of $f = 60.721$ GHz.

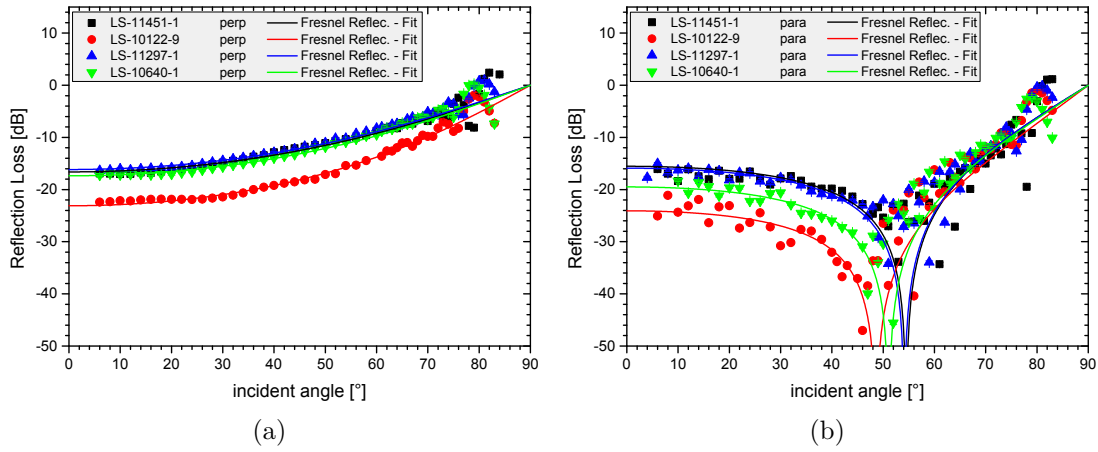


Figure 5.22: Reflection loss of the four different types of graphite foam at $f = 60.721$ GHz including fit functions. (a) perpendicular polarisation; (b) parallel polarisation;

Foam	thickness [mm]	n	κ	α [dB/cm]
LS-11451-1	6.35	1.34 ± 0.02	0.250 ± 0.002	-27.3 ± 0.9
LS-10122-9	12.70	1.11 ± 0.02	0.117 ± 0.001	-12.8 ± 0.6
LS-11297-1	19.05	1.40 ± 0.18	0.221 ± 0.013	-24.1 ± 6.2
LS-10640-1	25.40	1.33 ± 0.04	0.178 ± 0.001	-19.5 ± 0.2

Table 5.7: Index of refraction and absorption loss per centimetre of four types of graphite foam at $f = 60.721$ GHz derived from fit functions.

Figure 5.22(a) and (b) show the data of all four samples at this frequency using both polarisations including the fits to the Fresnel theory. Again, the measurement of the transmitted intensity yields the more suitable data to obtain the full complex index of

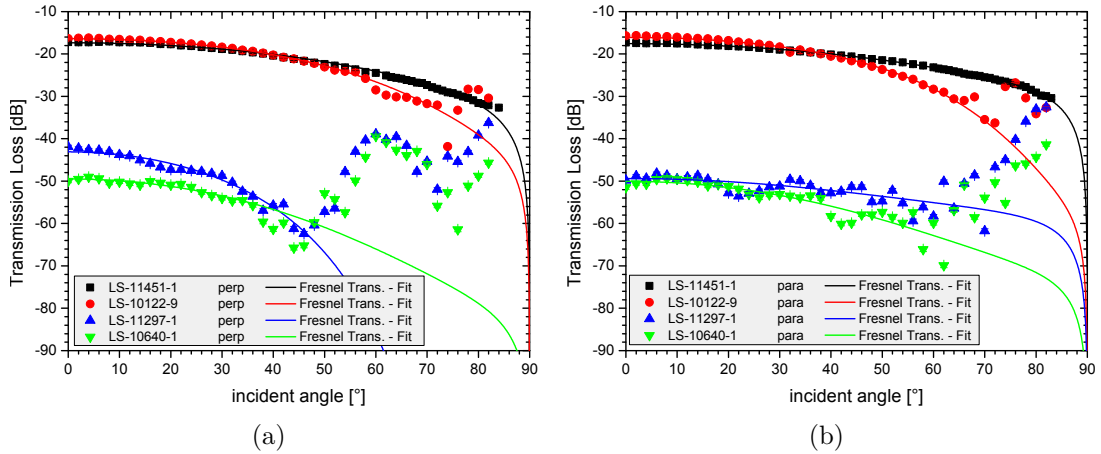


Figure 5.23: Transmission loss of the four different types of graphite foam at $f = 60.721$ GHz including fit functions. (a) perpendicular polarisation; (b) parallel polarisation;

refraction as absorption evidently takes place. Uncertainties are dominated by time-dependent intensity variations as explained in section 5.1.3.

The fit results are summarised in Table 5.7. The real part n is an average of all four measurements (reflection and transmission using both polarisations) whereas the imaginary part κ has been determined from the transmission measurements only. For the reflected data κ has been set to zero to eliminate accidental correlations between the fit parameters. From the plots one can see that foam LS-10122-9 differs significantly from the others as it is less absorbing but also less reflective. The fit results confirm this observation. The effective index of refraction is smaller in both real and imaginary part compared to the other samples. This leads to less reflected and absorbed intensity and corresponds to a higher transmittance especially at small incident angles. All four samples show good attenuation characteristics. Reflections can be attenuated by 10 dB even at angles up to 50° or even 70° in the case of LS-10122-9 which has the best reflectivity properties. The transmitted intensity can be reduced by about 18 dB by using only 6.35 mm of the LS-11451-1 foam which would satisfy the tracker requirements. The thicker samples attenuate even more than 40 dB but at the cost of more material and multiple Coulomb scattering.

Further tests regarding the tracker environment has been performed with the LS-11451-1 foam sample by attaching it to an aluminum board. This setup simulates the simplified case where the tracker layer would form a perfect reflector with a smooth surface. As seen before, the reflectivity of silicon is not as high as for aluminum, but the electronics and traces on the layer will increase the reflected intensity. The ideal setup would have been with a piece of the tracker. In this test (see Figure 5.24) the reflected intensity is dominated by the reflectivity of the foam itself as expected. The waves reflected at the foam aluminum border have to pass through the foam twice, therefore are attenuated twice by at least 18 dB under small incident angles and have subsequently no large influ-

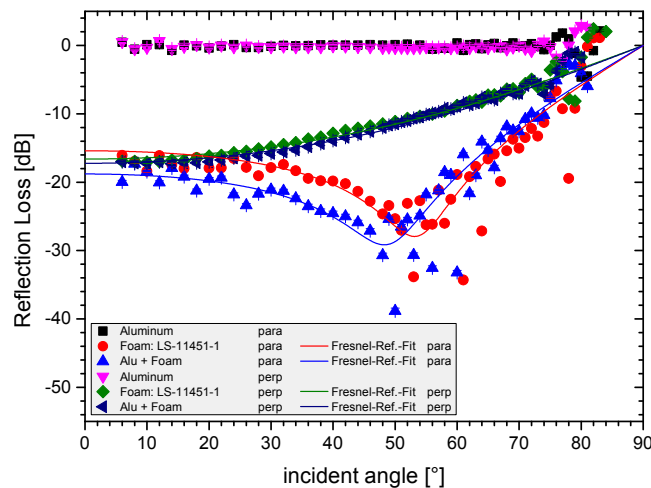


Figure 5.24: Reflection loss by graphite foam stuck onto an aluminum plate

ence on the reflected intensity. This holds especially for perpendicularly polarised waves. As the reflected intensity of parallel polarised waves is decreasing with rising incident angle up to the Brewster angle between 50 and 60° waves reflected by the aluminum board are of similar intensity. They seem to interfere destructively with the waves reflected at the boundary between air and foam and therefore reduce the total reflected intensity.

For the thinnest foam sample LS-11451-1 a frequency scan has been performed in the 60 GHz band. Analogously the data has been fitted using the reflection and transmission coefficient functions as before. The results for the complex index of refraction are illustrated in Figure 5.25. The uncertainties are the result of the averaging of the fit parameters. Therefore they are of pure statistical nature. In good approximation the real component n can be treated constant in the frequency band. Its average value is $n = 1.33 \pm 0.01$. The complex component κ (in the plot denoted as k) shows a small rise in the frequency range under test. The absolute value of the absorption loss per centimetre α (denoted as A) is correspondingly growing.

The index of refraction determined in this work as well as the absorption loss could be used for a more precise simulation of the wireless tracker readout system implementation. So far the simulation conducted by Hügler [35] assumed a fully absorbing material used as shielding. Graphite foam is highly absorbent, but especially under large incident angles the reflections are attenuated by only a few dB. These reflections from the shielding have been neglected. So, further simulation studies might be necessary which take them into account.

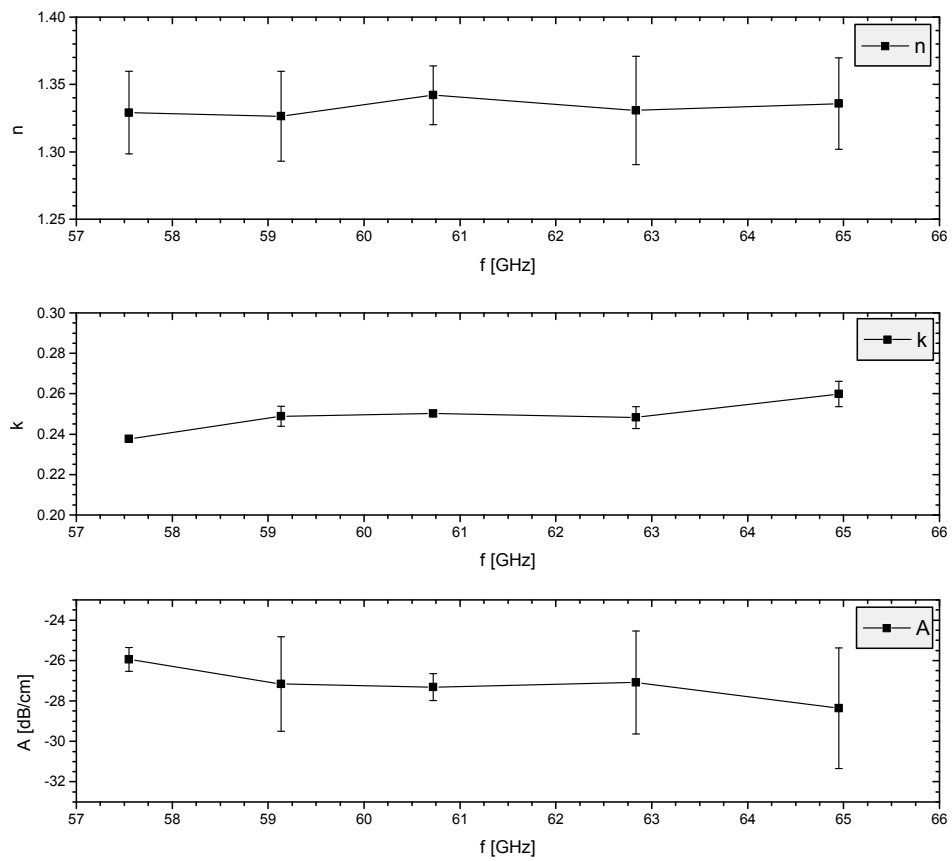


Figure 5.25: Frequency dependence of the index of refraction $N = n - ik$ and absorption loss A in dB/cm of graphite foam LS-11451-1

5.2.3 Insertion Loss and Inhomogeneity of Graphite Foam

In addition to the angular dependent reflection and transmission measurement an analysis with respect to the insertion loss at 0° incident angle of graphite foam has been performed. Results for the foam LS-11451-1 have already been presented in [34]. In this work the remaining three types of foam have been tested to find the material best suited for application.

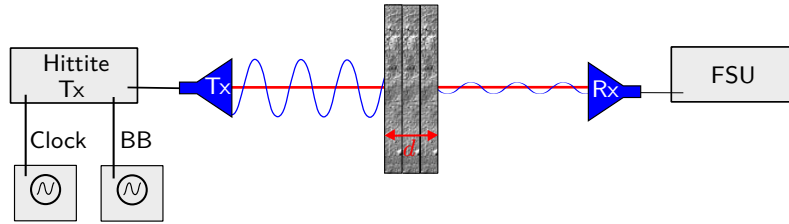


Figure 5.26: Setup for the measurement of insertion loss of graphite foam. FSU = spectrum analyser; BB = Baseband

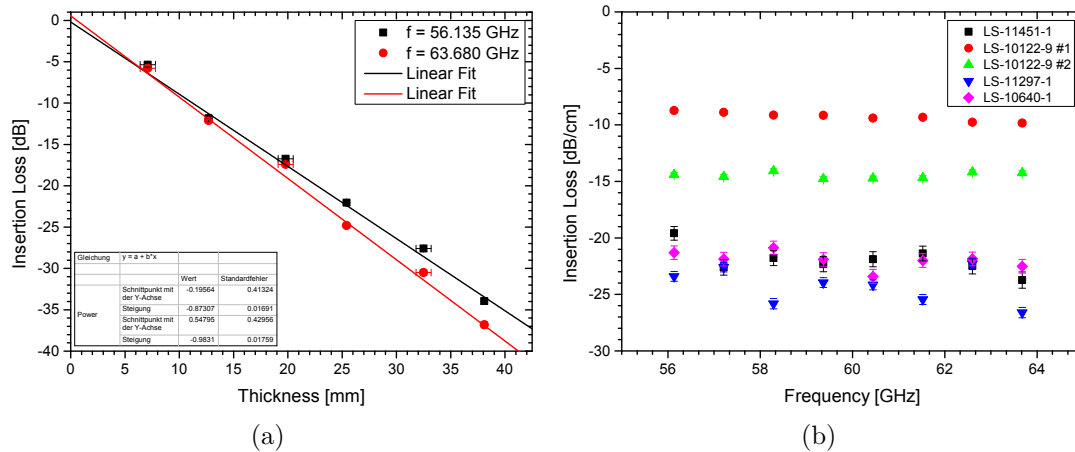


Figure 5.27: Insertion loss versus frequency of the tested foams derived from fit functions. (a) Fit of Lambert-Beer law to data of LS-10122-9. (b) Insertion loss of all foams as a function of frequency. LS-11451-1 data taken from [34].

In order to obtain the insertion loss in dependence on the thickness d of the sample different slices and multiple pieces of foam in a row have been tested. The setup is illustrated in Figure 5.26. Eight frequencies in the 60 GHz band have been chosen for this test. A fit of the Lambert-Beer law (see Equation 2.19) has been applied to the data whereas the function could be reduced to a linear fit as the intensity was measured in decibel. The slope directly yields the insertion loss per length. An exemplary fit to a LS-10122-9 sample can be seen in Figure 5.27(a). The uncertainties of the data points are derived from measurements of the thickness of the sample (x-error) and from time-dependent variations of the intensity (y-error). The fit results versus the corresponding frequency for all foams under test are illustrated in Figure 5.27(b) whereas the data for LS-11451-1 is adapted from [34] for completeness. The error bars correspond to the statistical errors

of the fit parameters. Two different samples of the LS-10122-9 foam have been tested. The samples LS-11451-1 and LS-11297-1 show variations of the order of several dB and also a small trend of higher absorbance at higher frequencies. The insertion loss of the remaining samples is quite constant across the frequency range analysed. The insertion loss has been averaged over the frequency band under test. The results are summarised in Table 5.8. As already seen in the reflectivity and transmittance measurement, foam LS-10122-9 differs significantly from the other samples. Besides, two samples of this foam exhibit largely different insertion losses which may be explained by inhomogeneities of the material.

Foam	Insertion Loss [dB/cm]
LS-11451-1	-22.0 ± 1.2
LS-10122-9 #1	-9.3 ± 0.3
LS-10122-9 #2	-14.5 ± 0.3
LS-11297-1	-22.0 ± 0.8
LS-10640-1	-24.3 ± 1.6

Table 5.8: Insertion loss of graphite foam averaged over the frequency band 56 – 63.75 GHz. Results for LS-11451-1 are taken from [34].

To quantify the inhomogeneity of the different foams the insertion loss has been measured for 9 pieces of each sample. All four materials under test showed a large spread regarding the insertion loss. Table 5.9 summarises the measured peak to peak values as well as the average insertion loss obtained. Regarding peak to peak values a variation of 6 dB to 12 dB was measured for all samples. This measurement has been conducted at a single thickness which corresponds to the sample's thickness itself. The average values are normalised with respect to this thickness. Like that the foams can be compared with each other on the one hand and with the results from the former measurements on the other hand. The average values are compatible to the last preceding measurements.

Foam	Thickness [mm]	ΔI_{min} [dB]	ΔI_{max} [dB]	$\Delta \bar{I}$ [dB/cm]
LS-11451-1	6.35	-12.8 ± 0.4	-18.5 ± 0.4	-25.3 ± 3.4
LS-10122-9	12.70	-14.2 ± 0.4	-22.2 ± 0.4	-13.9 ± 2.2
LS-11297-1	19.05	-46.3 ± 0.5	-54.6 ± 0.5	-26.0 ± 1.7
LS-10640-1	25.40	-50.7 ± 0.5	-62.7 ± 0.5	-22.1 ± 1.8

Table 5.9: Inhomogeneity of graphite foam regarding insertion loss ΔI . The mean value $\Delta \bar{I}$ has been normalised to the sample's thickness to allow for a comparison between the materials.

Graphite foam is highly absorbent in the 60 GHz band and has a low density. Reflections are strongly attenuated up to large incident angles. This material is therefore well suited to reduce the crosstalk in a tracking detector - even more if it is combined with directive antennas which can reduce crosstalk in the first place.

5.3 Crosstalk Measurements

The following experiments have been performed to determine the influence of crosstalk on the 60 GHz wireless transmission. The signal to noise ratio at the front of the receiving stage has been determined, i.e. the intensity ratio of the signals transmitted by the correct and the neighbouring transmitter has been measured. Hereinafter the signal introduced by the second transmitter is referred to as noise. These measurements will serve as a reference for the wireless data transfer measurements including crosstalk between two channels where the bit error rate is measured as a function of the settings. Two setups have been prepared, one to analyse the direct crosstalk, one to measure crosstalk introduced by reflections. In addition channeling has been tested.

5.3.1 Direct Crosstalk from Neighbouring Transmitter

The first setup is illustrated in Figure 5.28 and simulates two wireless links placed in direct proximity to each other by displacing a single transmitter along the axis perpendicular to the direct line of sight. Therefore the displaced link emits waves of the same polarisation like in the worst case scenario. Orthogonal polarisations would already yield a gain of more than 20 dB in the signal to noise ratio as seen in Section 5.1.4. Operating with two physical links the pitch between those two would be equivalent to the displacement.

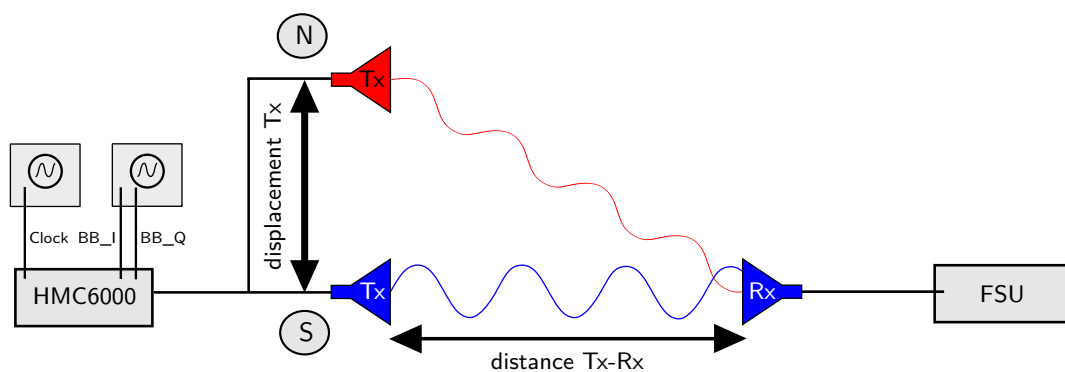


Figure 5.28: Crosstalk measurement setup #1: measuring signal to noise ratio by displacing the transmitter perpendicular to the direct line of transmission. BB_I/Q = baseband I/Q-component; FSU = spectrum analyser;

The distance between the waveguide adapters, i.e. without horn antennas mounted, of the transmitter at zero displacement and receiver has been chosen to be about the ATLAS tracker layer distance of 10 cm. The intensity of a 59.87 GHz single sideband signal is measured for all settings. A test without any horn antennas or graphite foam on both sides was carried out as a reference with a very broad intensity distribution, as the waveguide aperture itself leads to a beamwidth of about 75° . Three configurations with 4.5 cm long Kapton horn antennas have been tested: transmitters only, receivers only and to both at the same time. Hollow graphite foam cylinders (see Figure 5.31(c)

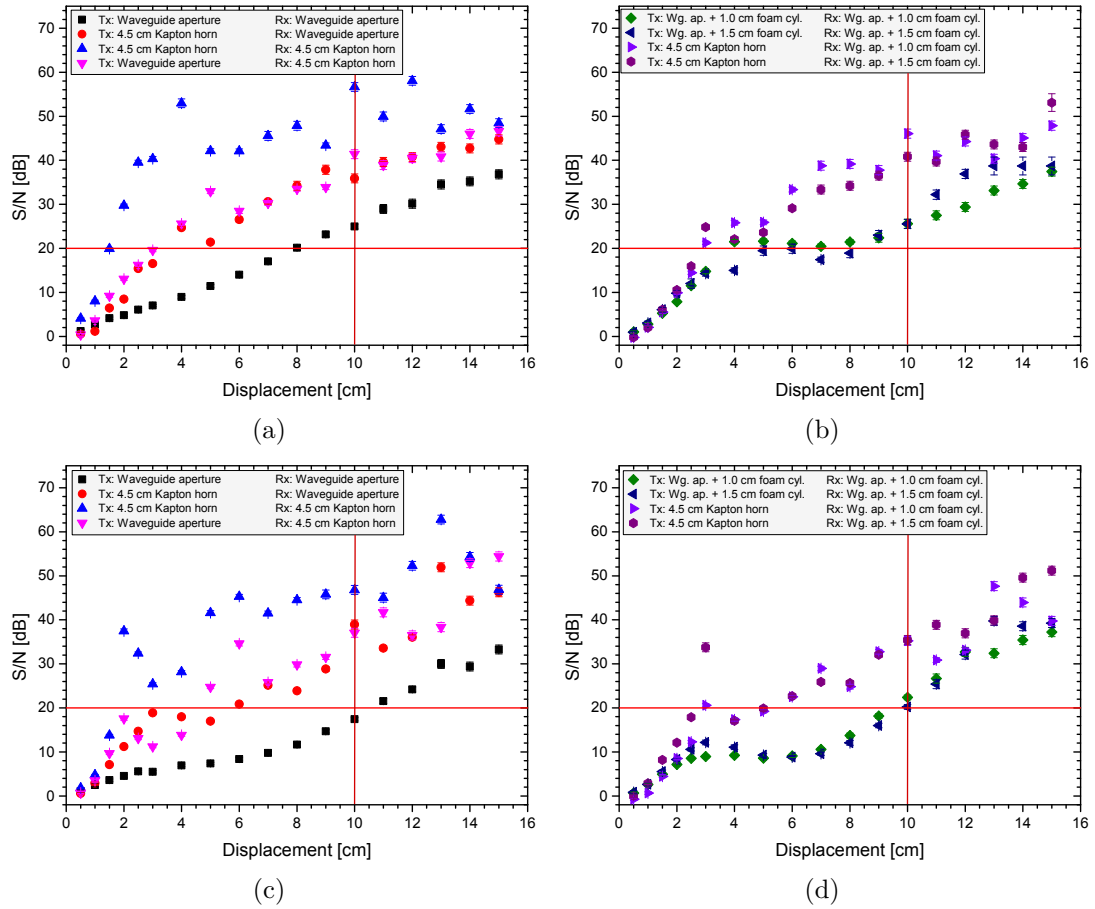


Figure 5.29: Signal to noise ratio by displacing transmitter in the
 (a) H-plane: horn antennas. (b) H-plane: foam and horns.
 (c) E-plane: horn antennas. (d) E-plane: foam and horns.

in the next section, material LS-11451-1, 6.35 mm thick) with a diameter of 1.0 cm and a length of 1.0 cm or 1.5 cm respectively have been used on both ends of the wireless link without directive antennas. In addition a measurement has been conducted with a directive antenna mounted on the transmitter and a foam cylinder on the receiver. The resulting signal to noise ratios by displacing the transmitter in both polarisation planes are illustrated in Figures 5.29(a) to (d). The uncertainties of the ratios follow from the variations of the signal's and noise's intensity measured with the spectrum analyser.

As expected the signal to noise ratio is drastically increased by applying the highly directive antennas in both planes. The sidelobes of the antennas in the E-plane lead to the characteristic drops in the ratio at e.g. 3 cm with horn antennas applied. Expecting a signal to noise of more than 20 dB to be necessary for a stable transmission with a transmitter displacement of 10 cm the reference setup without any antennas would be sufficient in the H-plane but it would fail by a few dB in the E-plane. By applying one single antenna on either the transmitter or receiver the requirement can be fulfilled at a smaller displacement of 4 cm in the H-plane and 6 cm in the E-plane. With both

horn antennas mounted, the minimum displacement necessary for 20 dB signal to noise reduces further to 2 cm in both planes. Using hollow graphite foam cylinders instead of antennas a signal to noise ratio similar to that of a single directive antenna can be achieved at displacements up to about 4 cm. At larger displacement up to 11 cm no significant advantage to the reference setting is visible whereas at even larger displacement the 1.5 cm long foam cylinders reduce the measured noise. If a directive antenna is applied to the transmitter the gain in signal over noise with the shielding foam on the receiver is rather small compared to the setup with the antenna alone.

The results of this measurement can be transferred directly to the situation of two real data links operating at the same carrier frequency with parallel polarisations and equal output power. Then, the pitch between the two links resembles the displacement used in the experiment. A signal to noise ratio of more than 20 dB can be achieved for a system of two short-range wireless links by means of antennas and graphite foam shielding. This allows for reliable communication.

5.3.2 Multi-Path Crosstalk Between Reflecting Layers

The second setup represents a more realistic scenario of the tracker implementation by adding reflections to the line of sight crosstalk. The transmitting and receiving waveguide adapters have been placed in holes drilled into aluminum boards and have been fixed from the inside of the setup using flanges. A schematic of the setup is illustrated in Figure 5.30 and a view in the lab can be seen in Figures 5.31(a) to (d).

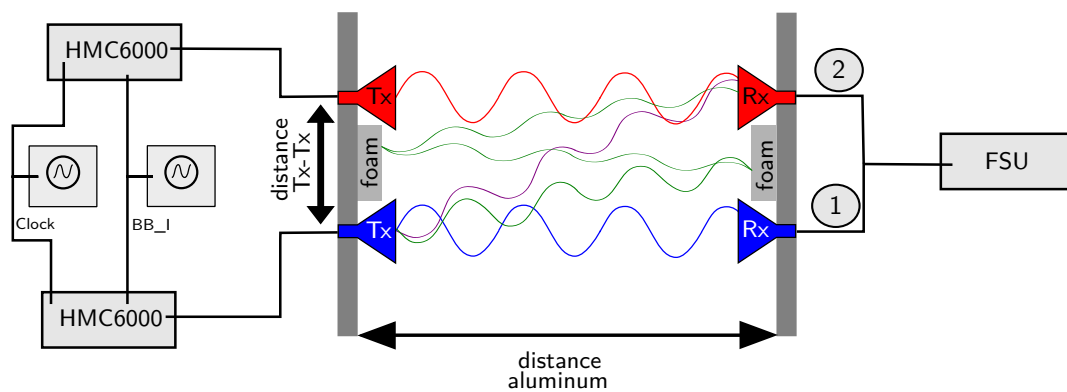


Figure 5.30: Crosstalk measurement setup #2: measuring signal to noise ratio by using two radio links between two aluminum plates. In purple a direct crosstalk path is indicated, green illustrates a reflected path. An example for a test to reduce the crosstalk is indicated by the graphite foam attached to the aluminum boards. FSU = spectrum analyser; BB_I = Baseband I-component of the IQ modulator's input;

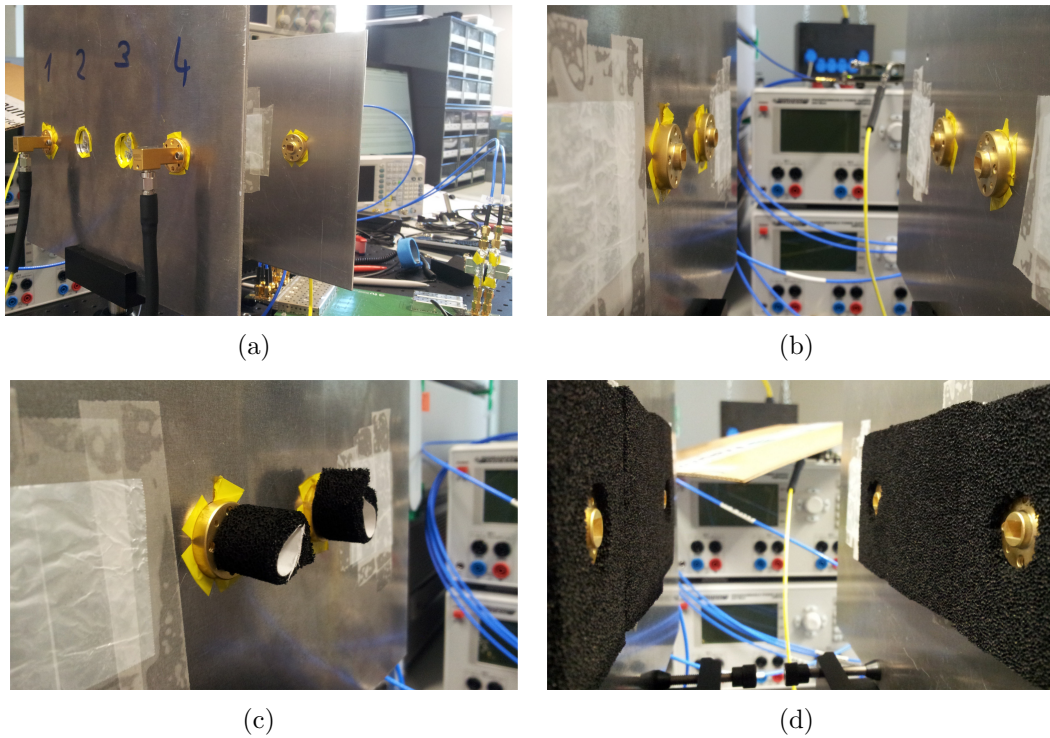


Figure 5.31: Setup in the laboratory. (a) view from outside (b) view from inside (c) hollow foam cylinders (1 cm diameter, 1 cm long, 6.35 mm thick) (d) 6.35 mm graphite foam covering both layers

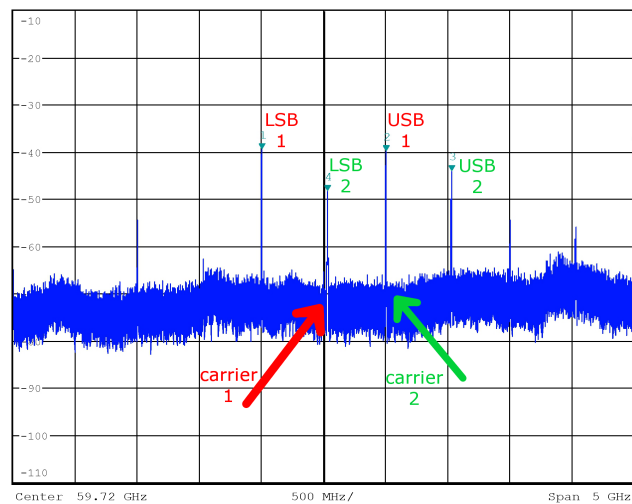


Figure 5.32: 500 MHz double sideband signals (upper = USB and lower = LSB) of two links operated at 59.72 GHz and 60.25 GHz. Carrier signals' intensity at noise level.

The waveguide adapters could be rotated to perform tests with both linear polarisation components. Moreover 4.5 cm long Kapton horn antennas were mounted as well as hollow graphite foam cylinders as shielding. Pieces of graphite foam could be mounted onto the plates to test the impact of attenuated reflections. Different settings have been tested and the results are presented in the following paragraphs. Both transmitters were operated with an external clock reference of 302 MHz and a double sideband signal of 500 MHz. The transmitters operated at neighboring carrier frequencies: one was operated at 59.720 GHz, the other at 60.249 GHz. The signals measured with the spectrum analyser are depicted in Figure 5.32.

The intensity of the RF signals has been measured in both receivers. The upper and lower sideband signals of the links have been compared in each receiver which produced four signal to noise ratios in total. The average of these ratios is used for the further analysis to give a rough estimate on the benefit of the tested settings. The standard deviation resulting from the averaging process is used as the mean ratio's uncertainty. The pitch between the transmitters could be set to 5 cm, 10 cm and 15 cm. The distance between the plates was 10 cm once and 15 cm in a second measurement. The impact of both distances on the ratios was analysed.

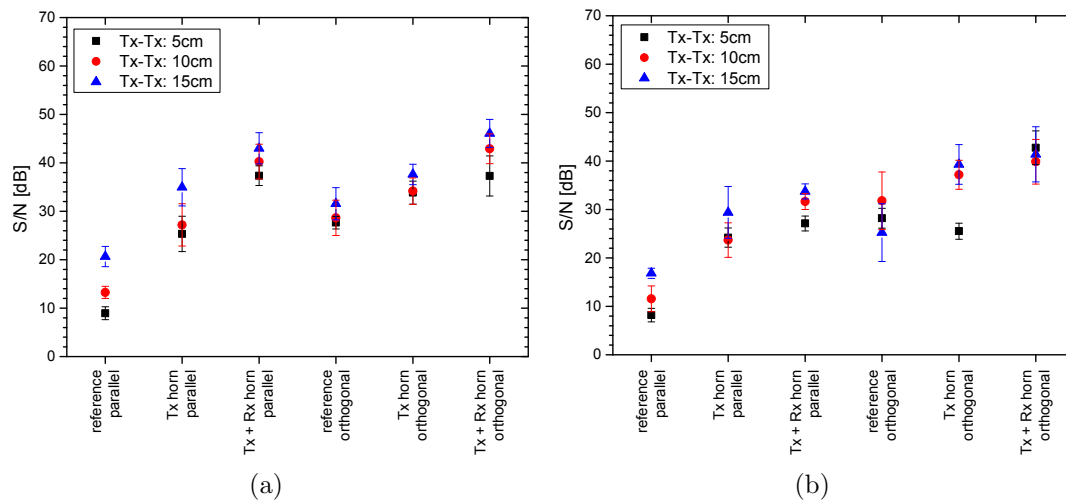


Figure 5.33: Signal to noise ratios at different layer distances and pitches between transmitters with parallel and orthogonal polarisation using horn antennas at (a) 10 cm and (b) 15 cm layer distance.

The setup without horn antennas and foam absorber serves as a reference using both parallel and orthogonally polarised links. In the reference setup the S/N increases strongly with the transmitter's pitch from less than 10 dB at 5 cm pitch to 21 dB at 15 cm pitch at a link distance of 10 cm. For 15 cm distance it reaches 17 dB at the maximum pitch.

Using orthogonally polarised transceivers already yields signal to noise ratios of more than 25 dB at all tested pitches and distances even without directive antennas or shielding. Horn antennas were applied to the transmitter only and to both transmitter and

receiver. A signal to noise larger than 22 dB was achieved in all cases with horn antennas mounted on the transmitter only for both polarisations. With both antennas mounted a S/N of more than 25 dB was achieved for 15 cm distance and more than 35 dB for 10 cm distance. The gain in S/N by the horns is larger at a smaller layer distance because the link distance over air is reduced. It also appears that the benefit of the antennas is bigger for links of parallel polarisation, but operating at orthogonal polarisation one can also gain 10 dB and more by the application of horn antennas. The described results are plotted in Figures 5.33(a) and (b).

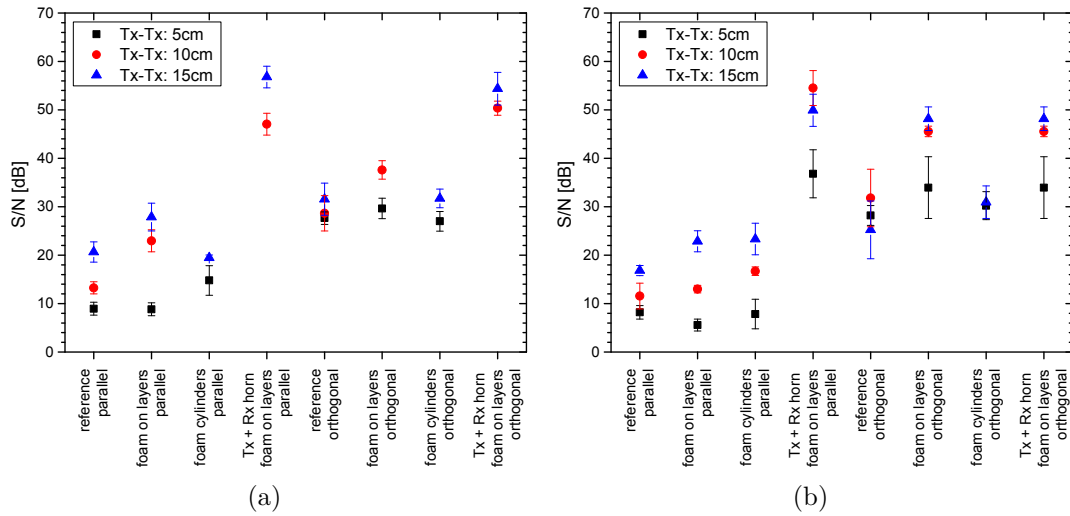


Figure 5.34: Signal to noise ratios at different layer distances and pitches between transmitters with parallel and orthogonal polarisation using graphite foam at (a) 10 cm and (b) 15 cm layer distance.

Figures 5.34(a) and (b) show signal to noise ratios for settings including graphite foam. Sticking pieces of foam on the layers between the transmitters and receivers only yields a gain in signal to noise at larger pitches of 10 and 15 cm. At a closer pitch of 5 cm without a directive antenna the line of sight crosstalk is dominant such that no gain is visible for parallel polarisations. For 1 cm long hollow foam cylinder with a diameter of 1 cm there is no absolute trend observable. Some measurements show an increasing, others are slightly decreasing trend. The cylinder also diminishes the quality of the correct signal. A measurement has been performed with antennas mounted on the transmitters and receivers and with graphite foam mounted on the plates. At pitches of 10 and 15 cm the foam further increases the signal to noise ratio compared to the measurement with the antennas alone. In these cases reflections from the layers are the dominating source of noise and the foam attenuates them.

The conclusion of these measurements is that graphite foam can reduce reflections at pitches of the order of 10 cm between the transmitters. At smaller pitch the impact of the foam decreased as the crosstalk is dominated by the line of sight paths. Together with orthogonal polarisations and directive antennas the crosstalk can be strongly reduced. It would be interesting to use directive antennas smaller than the horns under test like

e.g. patch array antennas where the wireless transmission distance matches the distance between the layers. An even more realistic scenario could be created by exchanging the aluminum layers with spare tracking detector elements.

5.3.3 Signal to Noise at the Output of the Receiver

So far the signal to noise ratio has been considered only at the input of the receiver. But the demodulated output's signal to noise is at least as important. The connection between the signal to noise in the 60 GHz modulated signal and the receiver's output has been probed in the following experiment.

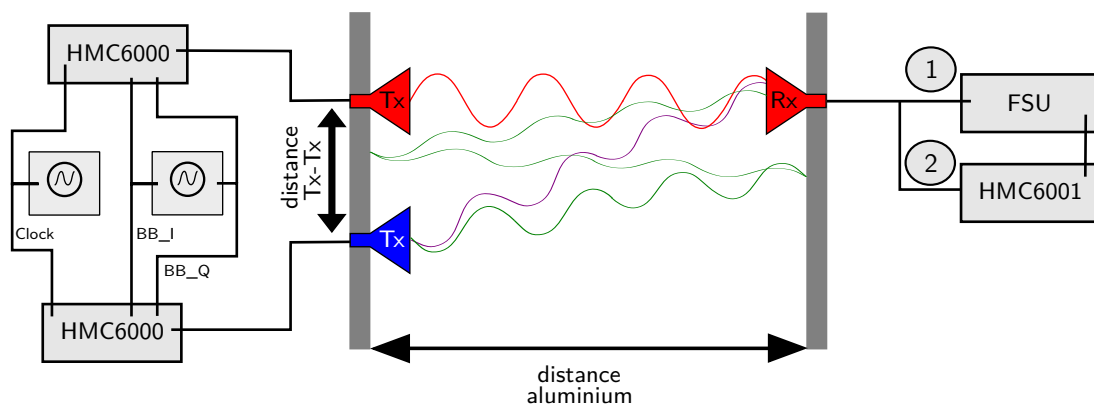


Figure 5.35: Crosstalk measurement setup #3: measuring signal (red Tx) to noise (blue Tx) ratio at the receiver input (1) and output (2). FSU = spectrum analyzer; BB_I/Q = baseband I/Q-component;

Carrier [GHz]	Carrier [GHz]	RF [GHz]	RF [GHz]	BB [GHz]	BB [GHz]
Tx 1	Tx 2	Tx 1	Tx 2	Tx 1	Tx 2
59.72	60.25	59.87	60.10	0.15	0.38
59.72	60.78	59.87	60.63	0.15	0.91
59.72	61.83	59.87	61.68	0.15	1.96

Table 5.10: Carrier, sideband radio frequencies (RF) and baseband (BB) frequencies of signal (Tx 1) and noise (Tx 2)

The experiment has been conducted with a wireless link at 10 cm distance and a second transmitter placed 5 cm next to the link. The carrier frequency of the link was fixed to 59.72 GHz while the additional transmitter was operated at three different higher carrier frequencies. Their values are summarised in Table 5.10. The signal was a 150 MHz single upper sideband (USB) sinusoid generated with a Rigol DG4162 signal generator using both baseband I and Q inputs with a 90° relative phase shift between I and Q. The noise from the second transmitter was a 150 MHz single lower sideband (LSB) generated by inverting I and Q to create a -90° phase shift between them. The signal to noise

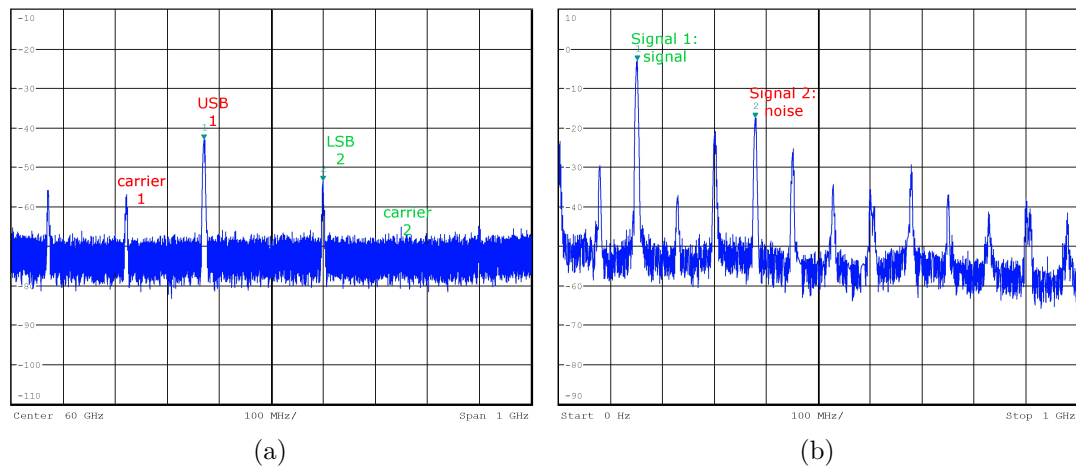


Figure 5.36: (a) Radio frequency (RF) USB1 signal and LSB2 noise at receiver's input. (b) Baseband (BB) signal and noise at receiver's output.

ratio has been measured at the receiver's input stage and its baseband output with the spectrum analyser. The signals in the radio frequency as well as in the baseband are depicted in Figure 5.36(a) and (b). The results of the three noise frequencies under test compared to the 150 MHz signal are depicted in Figure 5.37 on a double logarithmic scale. The uncertainties for the ratios are derived from the measured intensity fluctuations over time.

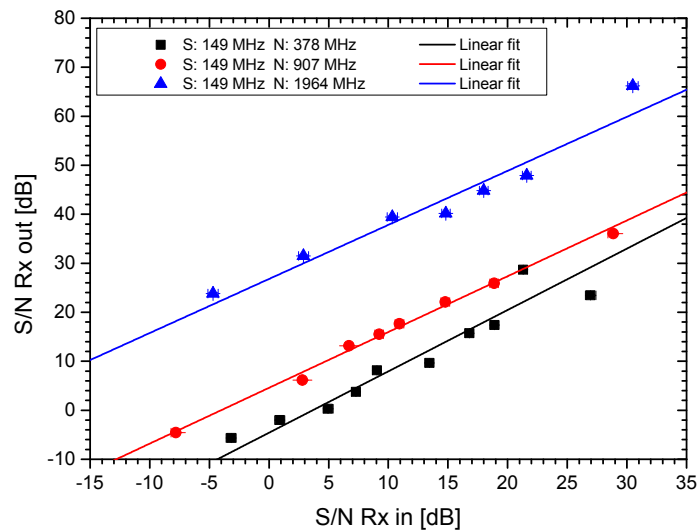


Figure 5.37: Signal to noise at receiver output vs input

The different signal to noise ratios at the receiver input have been generated using the adjustable intermediate frequency attenuation in the transmitter and horn antennas. There is a linear dependency between the input and output intensity ratios in decibel which results in a power law dependence for the intensity in milliwatt. A linear fit has

been performed to the data. Its offset is strongly influenced by the frequency offset. Transmitting a noise signal at 907 MHz the S/N of the output is increased by 9 dB compared to 387 MHz. Outside the nominal intermediate frequency bandwidth of the Hittite transceiver, which is 1.8 GHz, the offset is above 25 dB for a noise frequency of 1.96 GHz. The average slope, i.e. the correlation between the input and output intensity ratios, was found to be 1.16 ± 0.08 and is therefore compatible to 1. Transferring this power coefficient to the linear scale results in a linear dependence of the output S/N on the input.

The intensities at the receiver's input have been chosen to be smaller than -35 dBm maximum input power⁴. Therefore it is not surprising that there is a linear dependence on the input's intensity ratios. As the bandwidth of the receiver is limited to 1.8 GHz, the output's signal to noise ratio rises with fixed signal and increasing noise frequency. That means that two links closely next to each other should be able to transfer data stably if operating at channels that are separated by at least twice their intermediate frequency bandwidth.

⁴datasheet by Hittite [50]

6 Wireless Data Transfer

It is one of the main goals of this master thesis to create a test bench for the future 60 GHz transceiver chip introduced in Chapter 4. In order to test the quality of operation of this newly designed chip a bit error rate test (*short*: BERT) has been developed and tested using the Hittite 60 GHz transceiver. This chapter deals with the implementation and evaluation of this test setup. Section 6.1 shows the principle of such a test and its implementation in hardware. The results of the measurements are comprised in this section as well. Another option to determine the transmission's quality is described in Section 6.2 which deals with the analysis of eye diagrams. Section 6.3 covers different measurements which were performed in order to determine the influence of crosstalk on the wireless data transfer.

6.1 Bit Error Rate Test

The implemented bit error rate test is based on a design example by Altera which can be found in [51]. Because of the needs to include an 8b/10b encoder and an I/Q-splitting module into the data chain and to provide the baseband signal at the same time the design has been implemented completely from scratch. The bit error rate test has been developed in VHDL¹ using the Quartus II software from Altera². It runs on an Altera Stratix V GS FPGA which is the central component of the DSP³ Development Kit, Stratix V Edition [53]. The transceivers of this FPGA are capable of transmitting and receiving data at high rates up to 14.1 Gbps. In the following paragraphs the firmware design is described.

6.1.1 Implementation

The bit error rate test produces pseudo random data which is encoded, modulated and serialized to create a fast data stream. It is also capable of receiving this data stream again and detecting bit and byte errors. A block diagram of the modules of the transmitting chain is shown in Figure 6.1. The receiving data path is presented afterwards. The setup described here runs at an internal clock frequency of 176 MHz and produces data at a rate of 1.76 Gbps to use the full Hittite transceiver bandwidth, though other data rates were tested as well.

The **PRBS8** module generates an 8 bit wide pseudo random binary sequence (PRBS) according to [54] using a linear feedback shift register (LSFR) [55]. Every clock cycle each bit gets shifted up by one as the result of an xor-operation of the bits 7, 5, 4 and

¹VHDL = Very High Speed Integrated Circuit Hardware Description Language [52]

²<http://www.altera.com>

³DSP = Digital Signal Processing

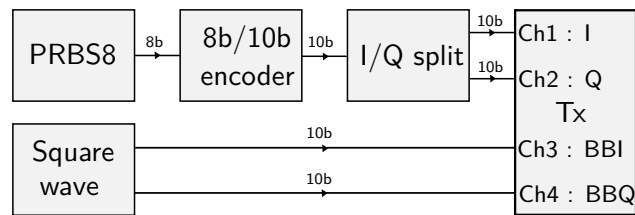


Figure 6.1: Block diagram of the modules in the transmitting data chain of the bit error rate test. Above the arrows the data width is indicated.

3 is inserted as the least significant bit (LSB). Figure 6.2 illustrates this process.

The **8b/10b encoder** generates for each 8 bit word the corresponding 10 bit code following [56]. Although this encoding yields a 25% higher data rate to transfer the same information, the benefit is to gain a DC-balanced data stream which is more robust. DC-balanced means that the number of transmitted 1's equals the number of 0's. The quantity measuring this is called running disparity. The encoder ensures that the disparity stays neutral in the long term. 8b/10b encoding is also useful for the synchronisation of the receiver as unique comma symbols can be inserted into the data stream. It is also possible to detect 1 bit errors as not all possible 10 b symbols are used for the coding. For its implementation a free design by OpenCores⁴ has been used.

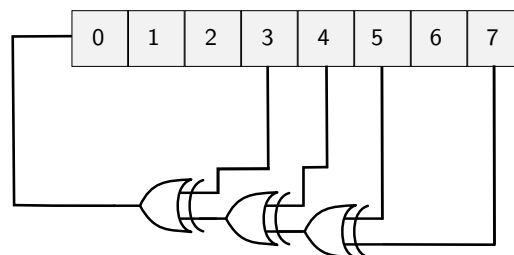


Figure 6.2: Visualisation of the linear feedback shift register which produces an 8 bit pseudo random pattern.

After encoding the data are split into two 10 b components in the **I/Q-split** module which are provided to drive the inverters on the MSK-modulator's inputs of the Hitrite transmitter. According to Section 2.4 the IQ components of the data stream are switched synchronously to the baseband IQ zero-crossings to generate a transition in the serialized data. For diagnostic purposes this module can either create square waves or it can be fully bypassed. It is also possible to inject errors into the data stream before the signal is split.

Parallel to the above mentioned modules two 440 MHz square waves with a relative 90° phase shift at a frequency of one quarter of the data rate are created in the **Square wave** module. These signals are directly connected to the transmitter modules and serve as

⁴<http://opencores.org>

the baseband signals mentioned before.

The transceivers are implemented using the Stratix V Transceiver Native PHY IP core function [57]. The **Transmitter (Tx)** module includes a phase compensation FIFO in the PCS⁵ and a bit serializer in the PMA⁶, which converts the 10 b parallel data at a clock frequency of 176 MHz into a fast serial data stream of 1.76 Gbps. The transmitter data path can be seen in the upper half of Figure 6.3. Blocks in the standard PCS data path not mentioned here are bypassed.

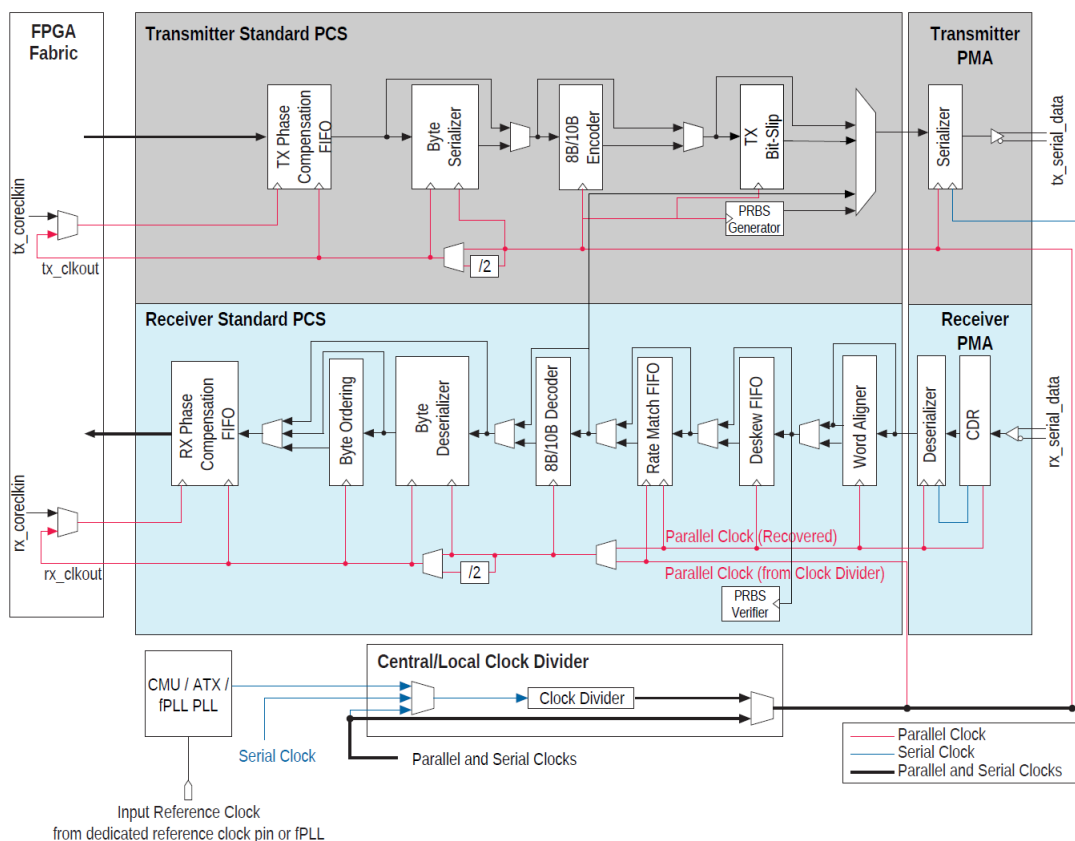


Figure 6.3: Data path of Stratix V Transceiver Native PHY IP core using the PCS standard option. The design uses only the FIFO in the transmitter PCS block, the other modules are bypassed. The receiver uses all the blocks except for the rate match FIFO, the byte deserializer and byte ordering module. Image taken from [57].

The receiving data path is depicted in Figure 6.4. A detailed picture of all blocks included in the **Receiver (Rx)** module can be seen in the lower half of Figure 6.3. Although it is necessary to use four transmitter channels, only one receiver channel is needed to cap-

⁵PCS = Physical Coding Sub-layer

⁶PMA = Physical Media Attachment

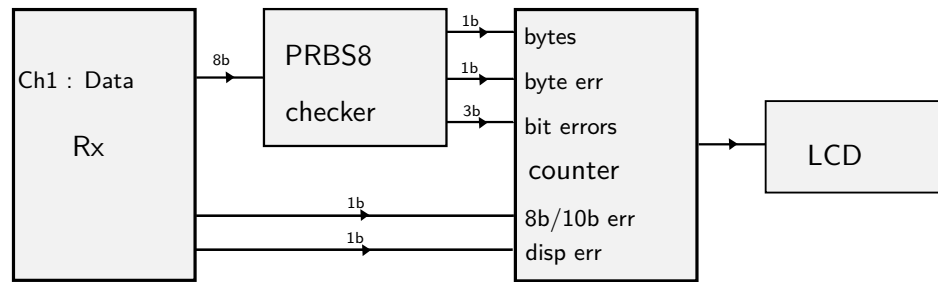


Figure 6.4: Block diagram of the modules in the receiving data chain.

ture the data. In the PMA block the CDR⁷ recovers the fast serial clock from the data which is used for the deserialization and the slower parallel clock. In the PCS block an automatic state machine aligns the data stream to the specified synchronisation pattern which is included in the serial data stream. Once it has been found the receiver is locked to the data. The 10 bit parallel data is then checked for errors in the 8b/10b code and in its running disparity. After decoding the 8 bit parallel data word is available for further processing.

The receiver is followed by the **PRBS8 checker** module which uses the first word after the synchronisation pattern as a seed for its own PRBS8 pattern generator. The following received symbols are then compared to the result of this generator using a bitwise xor of both words. In this manner bit and byte errors can be detected.

The subsequent **Counter** module counts the number of bytes processed, byte and bit errors found as well as the 8b/10b code errors and disparity errors detected. The numbers generated hereby are forwarded to a **LCD-controller** which writes them onto the LCD integrated in the development kit. In this way it is possible to read off the byte and bit error rate easily.

6.1.2 Setup

The test setup for the wireless data transmission is quite small. It consists of one Hittite transceiver pair and one Stratix V FPGA together with its adapters for the input and output signals. The transceivers of the FPGA drive the HSMC (High Speed Mezzanine Card) pins of the development kit with the 1.5-V PCML⁸ differential standard from Altera [58]. The amplitude of the fully differential signal is about 650 to 800 mV. A HSMC to SFP (Small Form-factor Pluggable) adapter card called "SantaLuz Mezzanine Card", developed at TU Dortmund, with 8 SFP ports has been used. SFP to SMA adapters have been plugged into four SFP cages to create four fully differential transmitter and receiver channels. All 4 transmitter channels have been connected according to Figure 6.5 to the Hittite board using SMA to MCX cables, whereas only one receiver channel

⁷CDR = Clock Data Recovery

⁸Pseudo Current Mode Logic

was needed which is driven by the output of the FM demodulator of the Hittite receiver.

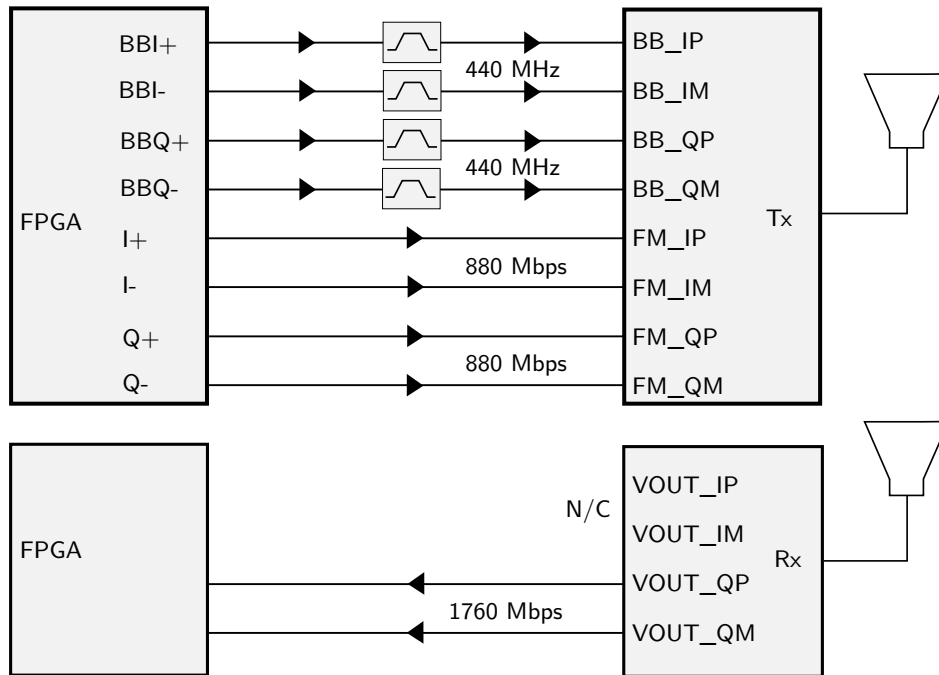


Figure 6.5: Connection of the FPGA transceivers to the Hittite board for the 1.76 Gbps bit error rate test. All signals are fully differential. The square waves on the baseband channels (BBI and BBQ) are bandpass filtered, all other channels are connected directly to the 60 GHz transceiver. The FM-ports are connected to the MSK modulator of the Hittite transmitter (Tx). The FM-demodulator of the receiver (Rx) is enabled. Therefore the demodulated data are present on the Q-output of the Rx. The I-output is not connected.

For 1.76 Gbps bit error rate test the two square waves transmitted by the baseband channels are bandpass filtered using adjustable Neosid UO433 helical filters to generate the sinusoids needed for the MSK. As the filters are adjustable the amplitude of the signal changes according to the center frequency. The filters have been adjusted such that the amplitudes of the differential sinusoids were about 200 mV each. Choosing another data rate between 1.2 Gbps and 2.4 Gbps the sinusoids are filtered out using 600 MHz 7th order low pass filters. The output signal of the low pass filtered sinusoids were about 700 mV, whereby amplitude differences between I and Q of the order of 50 mV have been noticed. This leads to a small degradation of the demodulated signal's quality.

The four differential output signals are phase aligned, i.e. for example at 1.76 Gbps the I- and Q-channel's transitions are synchronous to the zero-crossings of the corresponding baseband 440 MHz sinusoids with a precision of about $1.0 \pm 1.5^\circ$ which corresponds to a timing precision of the order of 10 ps, as can be seen for the I-channel in the right plot of Figure 6.6. As not all the traces on the SantaLuz card are of equal length the best achieved phase difference between I and Q using external delays was around 93° which

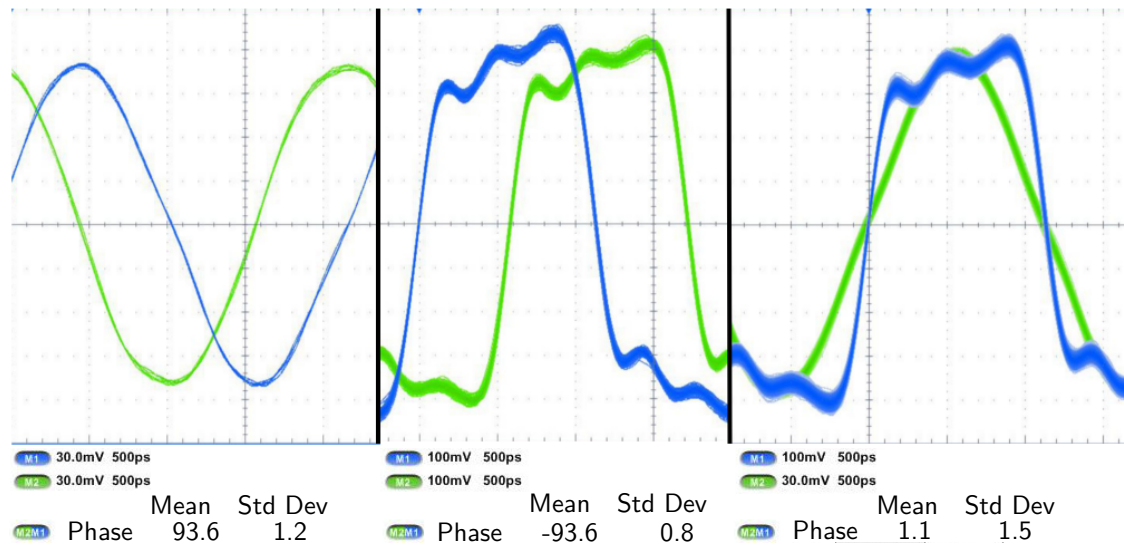


Figure 6.6: Phase relations between: BBQ (blue) and BBI (green) (left plot), I (blue) and Q (green) (middle plot) and between I (blue) and BBI (green) (right plot). The scales for the y-axis (voltage) and the x-axis (time) and the phase difference measured in degree are given.

can be seen in Figure 6.6 as well. Tests have shown that even at a phase difference of 100° the transmission is not completely deteriorated as will be shown in the next section.

The Hittite transceiver has been used with MSK-modulator and FM-demodulator. For all data rates except 1.76 Gbps an attenuation of the transmitter's intermediate frequency of 9.1 dB is necessary to avoid non-linearities in the circuit because the sinusoids amplitude is too large. Both internal and external reference signals have been applied to the frequency synthesizer to check for any differences in the quality of the transmission between these two modes. An Anritsu MG3692C signal generator has been used to provide the external oscillator frequency of 302 MHz at a power level of 3 dBm. For internal reference the 285 MHz on-board oscillator has been chosen. Both reference sources worked out equally well. Besides, as MSK does not need a coherent demodulator for data detection, it even functioned properly using two different transceiver evaluation boards with each board using its own oscillator.

A picture of the full setup in the laboratory can be seen in Figure 6.7(a). Here a wireless transmission over a distance of 22 cm is established using 4.8 cm long Kapton-aluminum horn antennas. The 60 GHz modulated output of the transmitter was coupled via a V-band cable and a coax-to-waveguide adapter to the antenna. The receiver was connected correspondingly.

The spectrum of the transmitter's output signal (see Figure 6.7(b)) has the typical shape for a MSK modulated signal. Asymmetries in the spectrum can be attributed to the small phase imperfection between I and Q. Peaks in the spectrum occur at multiples of ± 880 MHz which is half the transferred data rate.

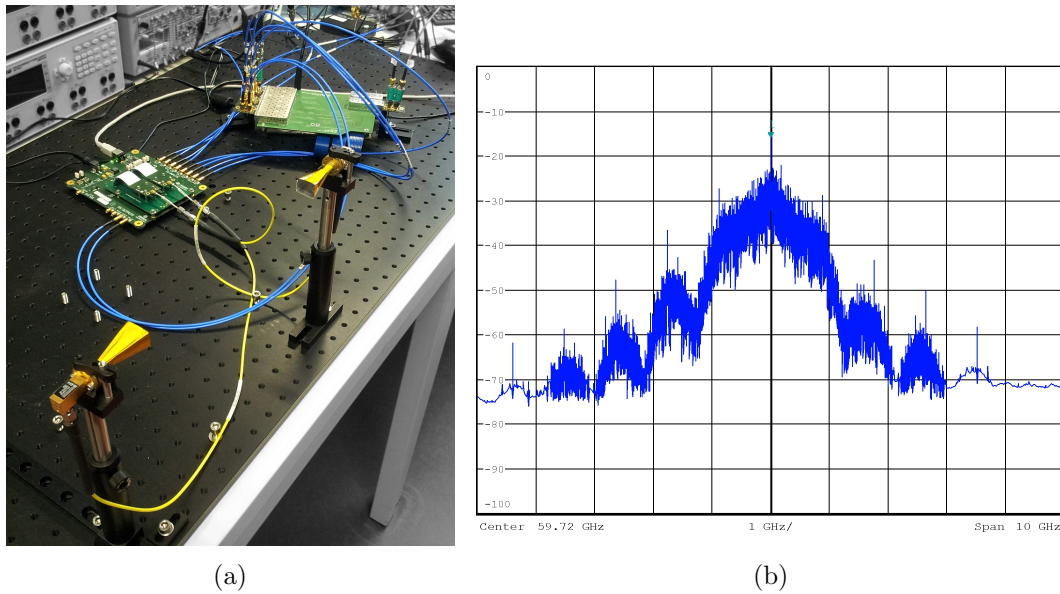


Figure 6.7: (a) Setup of the 60 GHz wireless data transmission in the laboratory. At front one can see the radio link using Kapton-aluminum horn antennas. The 60 GHz transmitter is connected to the antenna in the lower left corner. The FPGA with the HSMC adapter card are in the upper right corner. The Hittite evaluation board is to its left.
 (b) Spectrum of the MSK modulated signal in the 60 GHz-band.

6.1.3 Measurements and Results

The correct operation of the bit error rate test has been verified using both the serial loopback inside the FPGA transceivers as well as a wired connection between the transmitter and receiver. For all data rates not a single bit error was observed, unless it was injected manually.

Different settings have been checked using the wireless data transmission at 60 GHz. Using the setup of Figure 6.7(a) different data rates have been tested, the bit error rate tests ran on average for about 18 hours. The results are summarised in Table 6.1. Up to a rate of 1.76 Gbps not a single error has occurred. Therefore upper limits on the bit error rate are stated. Above the 1.8 GHz transceiver bandwidth limited by low pass filters in the Hittite chips the bit error rate increases quite fast. While at 2.0 Gbps a stable transmission is still possible with a measured BER of $6 \cdot 10^{-13}$, increasing the rate even further to 2.2 Gbps the bit error rate rises by four orders of magnitude to $9 \cdot 10^{-9}$. Finally at 2.4 Gbps, operating at 133% of the Hittite's bandwidth, the bit error rate reaches a level where a reasonable data transmission is not possible anymore. This shows that the bandwidth of the transceiver can be exceeded slightly if necessary without risking too much errors to occur, but one should not exaggerate this. The stability of the Minimum Shift Keying at 1.76 Gbps with respect to duty cycle dis-

Data rate	Bit error rate	Byte error rate
1.20 Gbps	$< 9.5 \cdot 10^{-15}$	$< 9.5 \cdot 10^{-14}$
1.50 Gbps	$< 9.8 \cdot 10^{-15}$	$< 9.8 \cdot 10^{-14}$
1.76 Gbps	$< 4.0 \cdot 10^{-15}$	$< 4.0 \cdot 10^{-14}$
2.00 Gbps	$6.2 \cdot 10^{-13}$	$1.3 \cdot 10^{-12}$
2.20 Gbps	$9.2 \cdot 10^{-9}$	$3.5 \cdot 10^{-8}$
2.40 Gbps	0.26	0.098

Table 6.1: Bit and byte error rates for different data rates using a 22 cm radio link with Kapton-aluminium horn antennas.

tortion was tested during two 16 hour runs. A radio link of 12.5 cm distance with the standard brass gain horns was used. With the before mentioned phase of 93° a bit error rate smaller than $9.5 \cdot 10^{-15}$ has been measured. The distortion was created by increasing the phase difference between I and Q to about 100° . It was found that the bit error rate is not yet increased and was measured to be below $9.6 \cdot 10^{-15}$. So, this 10° phase offset which corresponds to a duty cycle distortion of about $2 \cdot 63$ ps which is 22 %UI of the unit interval does not yet yield a large degradation of the transmission under these conditions in the laboratory.

To test that the demodulation of the 60 GHz MSK signal can be performed non-coherently, two separate evaluation boards have been used: one for the transmitter, the other for the receiver. Each board used its own 285 MHz oscillator, so the phase relation between transmitter and receiver was random. A short 90 minute run showed that at 1.76 Gbps no error occurred and a bit error rate of smaller than 10^{-13} has been measured. So the phase between both transmitter and receiver can be arbitrary and does not influence the data transfer.

6.2 Analysing Fast Data Links with Eye Diagrams

In addition to the direct measurement of bit errors occurring in the data stream with the help of the FPGA's logic it is possible to determine the quality of a high speed data transmission as well as its bit error rate by sampling the digital data. The advantage is that even very low bit error rates of the order of 10^{-15} or lower can be determined in a rather quick measurement whereas one would have to wait for days or even longer to measure one single bit error in the FPGA logic.

6.2.1 Eye Diagram Basics

Figure 6.8 depicts how an eye diagram is created from a typical data stream including impairments [59]. The serial digital data stream consists of 1's, 0's and transitions between these two states. The different bits are folded into a single graph and many samples are overlaid on top of each other. The resulting pattern includes all different transitions in the data stream and represents an average statistic of the signal. Its shape

resembles an eye. The inverse of the data rate, the bit period T_{bit} , is also called the unit interval (UI).

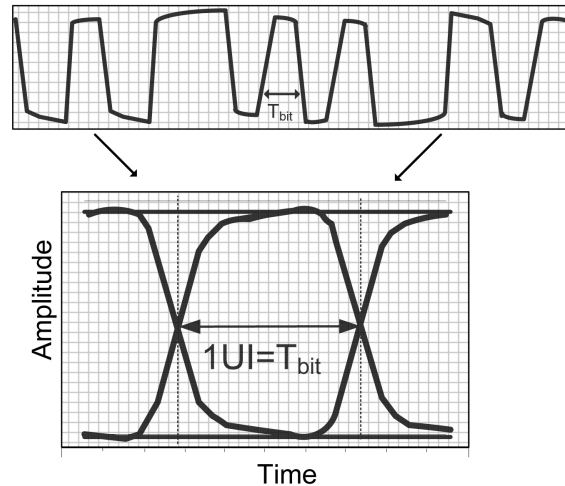


Figure 6.8: Generating an eye diagram from a realistic high speed digital signal. The above drawn serial data stream is sampled and its bits are folded into one single graph. Image taken from [59].

From the eye diagram different quantities can be measured. Some of them are highlighted in Figure 6.9. One and zero level correspond to the voltage of the logic one and zero states. Jitter and noise lead to distortions of the eye so that eye width and eye height will generally not equal amplitude and bit period. Rise and fall time correspond to the slope of transitions whereas the eye crossing percentage gives some indication of pulse symmetry issues and duty cycle distortions.

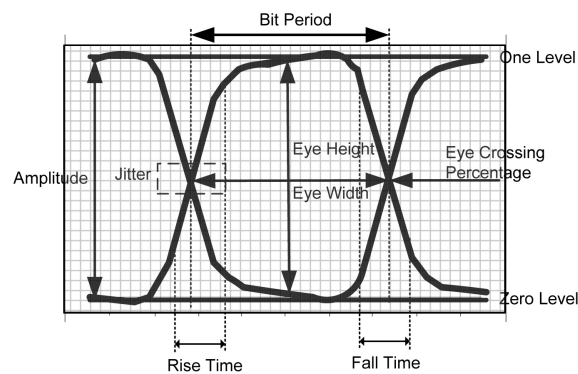


Figure 6.9: Some of the basic quantities which can be determined from an eye diagram. Image taken from [59].

Eye diagram measurements have been carried out using a Tektronix DSA8300 digital serial analyzer including modules with a bandwidth of 20 GHz to sample the signal without any losses. In addition to the overlaying of the data signal to generate the eye, jitter and

noise can be measured and their cumulative density functions can be analysed. Therefore the 80SJNB software has been used. Jitter corresponds to distortions in timing of the transition's edges which leads to horizontal eye closure. Vertical eye closure is caused by noise on the signal's levels. One distinguishes random and deterministic jitter and noise, where the latter consists of data dependent, periodic and other components which are introduced by the pattern, crosstalk, etc. [60]. These quantities are of interest for any data link to detect impairments. For example, data dependent jitter can be related to inter-symbol interference (ISI) [61] which can be caused by a signal which exceeds the bandwidth of the channel [22]. From these measurements the so-called bathtub curves for both timing and amplitude are created by evaluating the measured total jitter and noise probability density functions (PDF) to give an estimate of the bit error rate. A three-dimensional bit error rate eye diagram can be obtained by the convolution of both jitter and noise bathtub function [62]. Therefore the opening of this eye is a direct measure of the signal's quality and yields an estimate of the bit error rate.

6.2.2 Eye Diagram Measurements

The setup for eye diagram measurements is depicted in Figure 6.10. In order to analyse the signal output of the FPGA only the transmitter for the I-channel has been attached directly to the DSA whereas the IQ-modulator inside the FPGA's logic has been bypassed. This serves as a reference for the measurement with the entire wireless setup included.

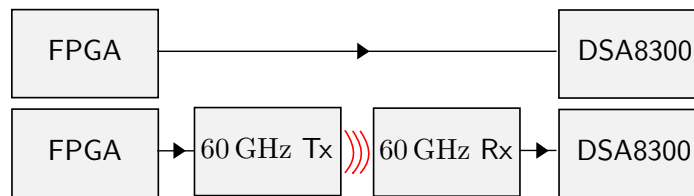


Figure 6.10: Connection of the FPGA to the DSA for measuring the eye diagram without the wireless transmission (up) and connection of the 60 GHz receiver to the DSA for analysing the eye diagram with the radio link included (down).

Figure 6.11 shows the sampled data streams at a data rate of 1.76 Gbps for both transmitting and receiving side. Obviously jitter and noise are added by the wireless transmission so that the transitions and logic levels are not that sharply defined anymore. Nonetheless the eye is widely opened, whereas in Figure 6.12 for a data rate of 2.0 Gbps one can see that the transceivers bandwidth is exceeded as the eye's height is diminished drastically and is only about half the margin between the asymptotical zero and one levels.

Eye width and height have been extracted from these measurements for different data rates and are comprised in tables 6.2 and 6.3. It should be noted that the errors for the automatic measurements of the eye parameters of the FPGA's signal in the wired transmission are of the orders of a few fs and μV which is why they have been omitted. However, this automatized analysis failed and a manual measurement with cursors has

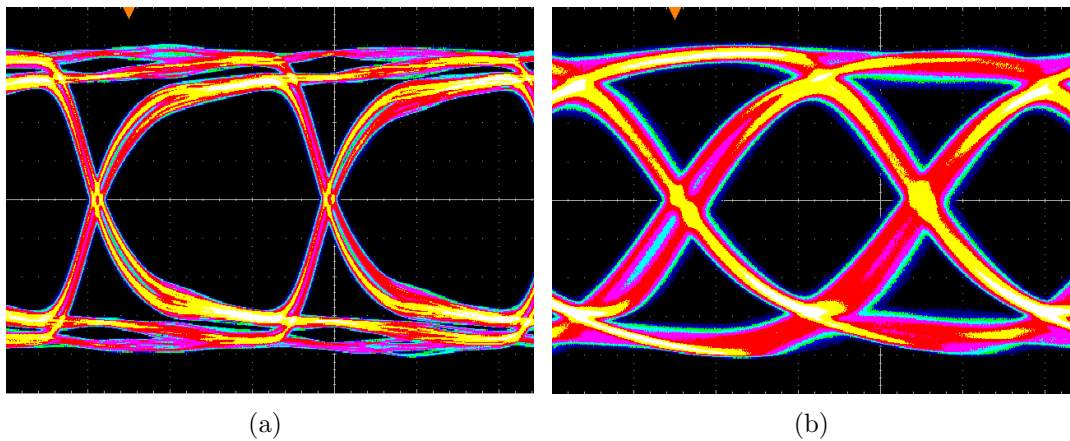


Figure 6.11: Eye diagrams at 1.76 Gbps. Scales: time: 200 ps/div, amplitude: 120 mV/div. (a) Wired data transmission; (b) 60 GHz wireless data transmission;

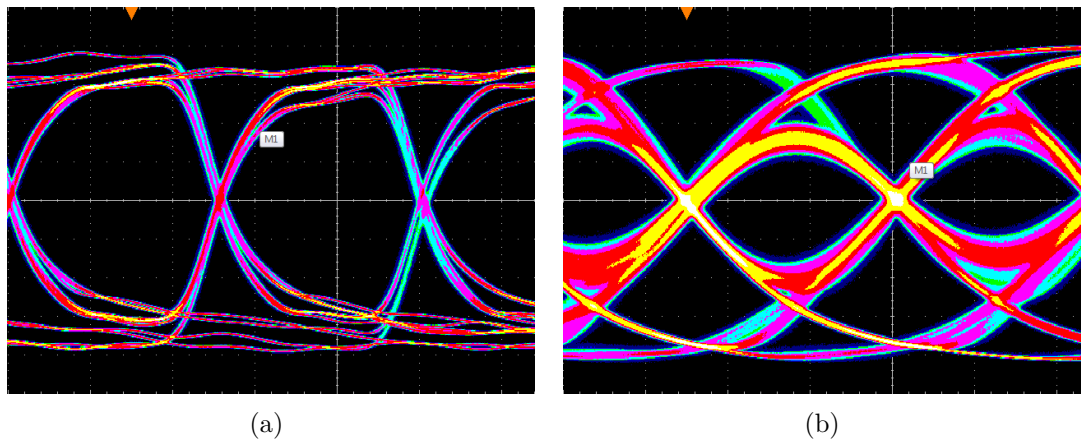


Figure 6.12: Eye diagrams at 2.00 Gbps. Same scales as Figure 6.11. (a) Wired data transmission; (b) 60 GHz wireless data transmission;

been performed for all wireless transmissions except at 1.76 Gbps because the eyes were not so widely opened as can be seen in Figure 6.12. This is reflected in the eye height, which is about twice as large at 1.76 Gbps than at the other rates. The reason for the vertical eye closure at higher data rates is the limiting 1.8 GHz bandwidth of the transceivers, whereas for smaller rates it is attributed to the inequality of the baseband I/Q amplitude's. Interpreting the results of the bit error rate measurements it can be concluded that an eye height greater than 200 mV is required for stable transmission. Comparing eye width before and after wireless transmission one can see that a lot of jitter is inserted by wireless transmission. The width is reduced by 86 to 142 ps for all rates. So the possible sample window for the FPGA's receiver is reduced. This applies most drastically for the highest tested data rate of 2.4 Gbps where the relative horizontal eye closure is about 45 % of the unit interval. The errors of the measurements with cursors are derived from measuring the parameters of two neighbouring eyes and averaging the

values. Large errors are most likely due to amplitude and phase imperfections in the baseband. These lead both to duty cycle distortions.

Data rate	Eye width [ps] wired	Eye width [ps] wireless	Width [%UI] wired	Width [%UI] wireless
1.20 Gbps	797.5	657 ± 7	95.7	78.8 ± 0.8
1.50 Gbps	582.5	490 ± 2	87.4	73.5 ± 0.3
1.76 Gbps	502.9	416.9	88.5	73.4
2.00 Gbps	466.1	351 ± 5	93.2	70.2 ± 1.0
2.20 Gbps	398.6	305 ± 1	87.7	67.1 ± 0.2
2.40 Gbps	371.6	229 ± 24	89.2	55.0 ± 5.8

Table 6.2: Eye width for a wired and a 60 GHz wireless data transmission at different data rates. UI: Unit interval; $UI = T_{bit}$

Data rate	Eye height [mV] wired	Eye height [mV] wireless	Height [% V_{pkpk}] wired	Height [% V_{pkpk}] wireless
1.20 Gbps	513.8	232 ± 20	52.9	26.0 ± 2.4
1.50 Gbps	502.9	257 ± 5	51.6	27.7 ± 0.5
1.76 Gbps	469.8	474.3	48.0	47.9
2.00 Gbps	522.7	227 ± 10	55.5	22.6 ± 1.0
2.20 Gbps	430.3	169 ± 3	43.9	16.0 ± 0.3
2.40 Gbps	470.2	147 ± 7	48.7	14.0 ± 0.7

Table 6.3: Eye height for a wired and a 60 GHz wireless data transmission at different data rates. V_{pkpk} : peak to peak amplitude of the respective signal

6.2.3 Jitter, Noise and Bit Error Rate Analysis

The DSA 8300's software 80SJNB allows for a precise separation of jitter and noise as well as a bit error rate analysis of fast serial data streams [60]. By measuring the cumulative density functions for the different components of timing and amplitude distortions it is possible to create the total jitter and noise probability functions and extrapolate eye closure up to very low bit error rates. In this analysis the software has been used to find impairments which are introduced by the wireless data transmission. Measurements have been carried out using different data rates as well as distances. The following paragraphs describe the analysis exemplary for a wireless transmission at a rate of 1.76 Gbps compared to the direct FPGA's output signal. Results of further measurements are summarised in tables 6.4 to 6.7 and analysed in the last paragraphs of this subsection.

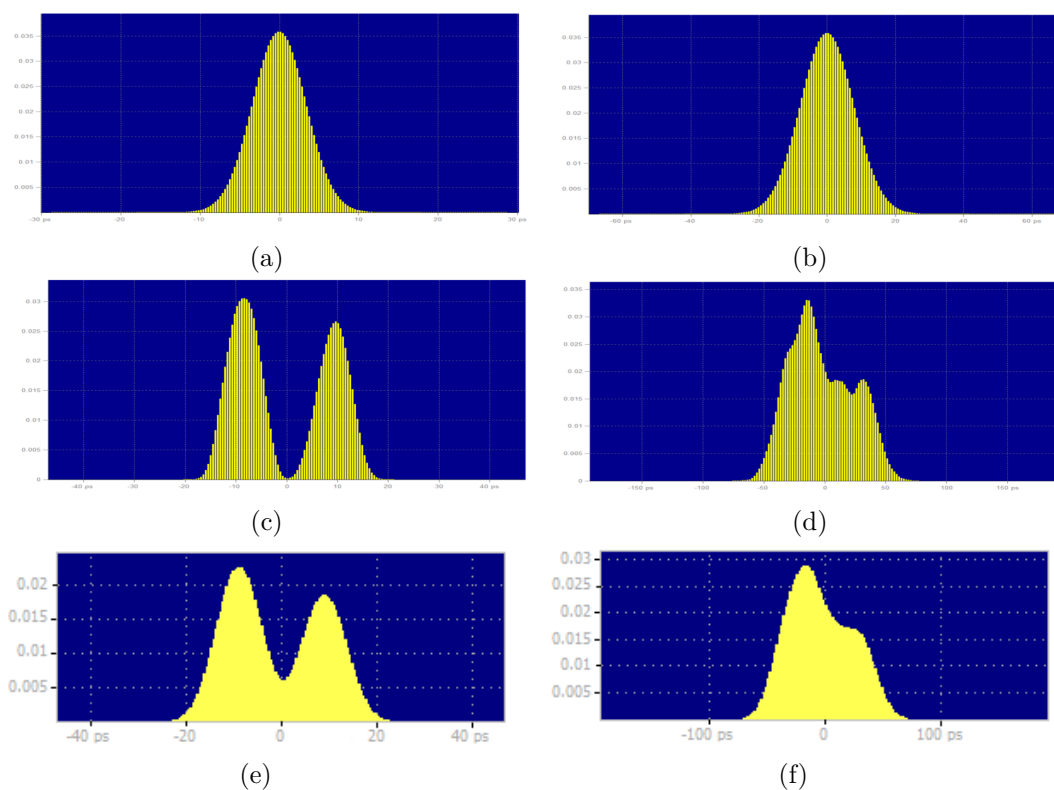


Figure 6.13: Jitter probability density functions a 1.76 Gbps data stream.

- (a) random: wired (10 ps/div); (b) random: wireless (20 ps/div)
- (c) deterministic: wired (10 ps/div); (d) deterministic: wireless (50 ps/div)
- (e) total: wired (20 ps/div); (f) total: wireless (100 ps/div)

By repeatedly sampling the 8b/10b encoded PRBS8 data pattern of a length of 2550 bits jitter and noise in the data stream are measured and their probability density functions (PDF) are generated. Random, deterministic and total jitter can be seen in Figure 6.13. One can clearly see how the wireless channel influences the signal's quality. The random component of jitter has grown as the width of the normal distribution is more than a factor of two larger than for the wired data transfer. But the largest impact can be seen

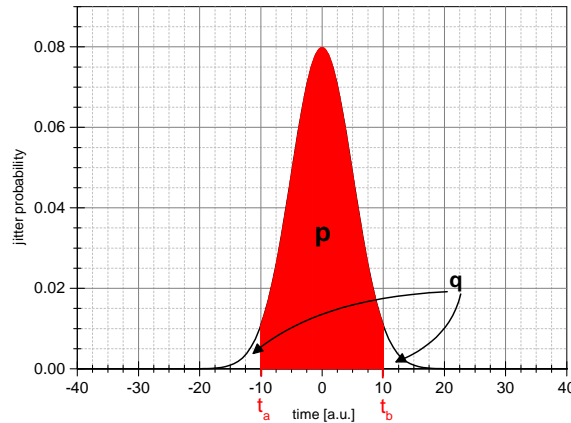


Figure 6.14: Integrating the jitter PDF up to a certain probability $p = 1 - q$ to measure the total jitter in dependence of the bit error rate q .

in deterministic jitter. The shape of its probability distribution is substantially altered so huge jitter is picked up by the wireless channel. The total jitter is dominated by the deterministic component. The same observations are made for the noise.

Based on the total jitter and noise measurement bit error rate estimates can be computed for an ideal decision circuit [62]. An error occurs if the amplitude of a binary 1 signal falls below the decision threshold at the decision point in time. The same holds for a binary 0 if the threshold is exceeded. The following example shows how the bathtub curves are calculated from the measurements and bit error rate estimates are produced.

Figure 6.13(f) represents the total jitter probability density function. Integrating the PDF according to Equation 6.1

$$p = \int_{t_a < 0}^{t_b > 0} p_{TJ}(t) dt = 1 - q, \quad (6.1)$$

from $t_a < 0$ to $t_b > 0$ yields the probability p which includes all the jitter up to the width $t_p = t_b - t_a$ of the PDF. An illustration can be found in Figure 6.14 for the simple example of a normal distribution. By setting p to a fixed probability that includes everything but a small fraction q called the bit error rate ($p = 1 - q$) the jitter is calculated depending on the aimed bit error rate. This amount of jitter is then added to the bit transitions to create the horizontal bathtub curve. Integrating the PDF for example up to a fraction of 10^{-15} yields the points at $\log(BER) = -15$ of the bathtub curve on both transition sides which would ideally take place at ± 0.5 UI. For 1.76 Gbps this corresponds to ± 284 ps. The width between the falling and rising part of the bathtub curve yields the width of the eye at a given bit error rate. Similarly the horizontal bathtub curve is created from the noise measurement at the logic 1 and 0 levels each. The total jitter and noise using the wireless channel at different data rates are summarized

in tables 6.5 and 6.7.

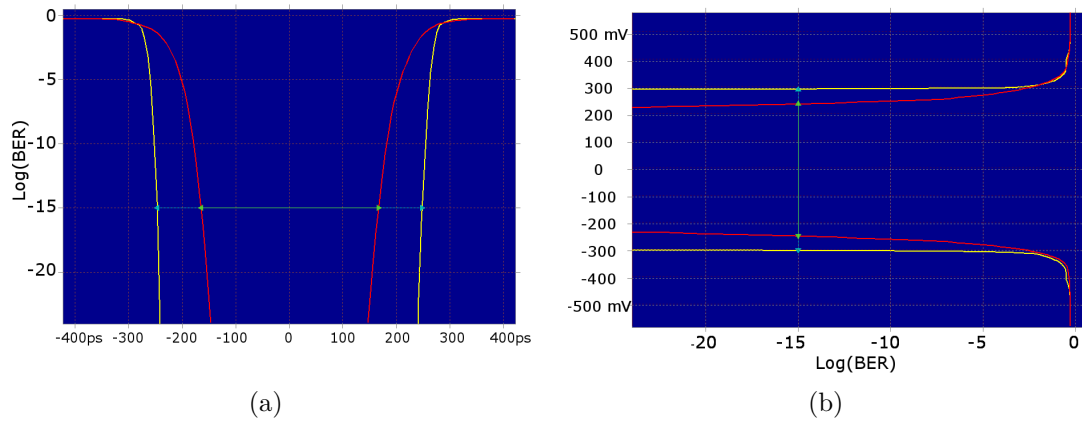


Figure 6.15: Comparison of bathtub curves for (a) timing (horizontal) at decision threshold and (b) amplitude (vertical) at decision point for a wired (yellow) and a wireless (red) system at 1.76 Gbps.

Figure 6.15(a) and (b) show the horizontal and vertical bathtub curves up to a bit error rate of 10^{-24} for both a wired and a wireless transmission. The arrows indicate the eye's opening matching to a bit error rate of 10^{-15} . From the plots one can immediately see the impact of the picked-up jitter and noise by the wireless as the width in both dimensions for smaller bit error rates is decreased. With the knowledge of the receiver's sampling window regarding amplitude's threshold, setup and hold times one can determine the crossing point of the bathtub functions with these thresholds. This yields a very precise estimate of the bit error rate.

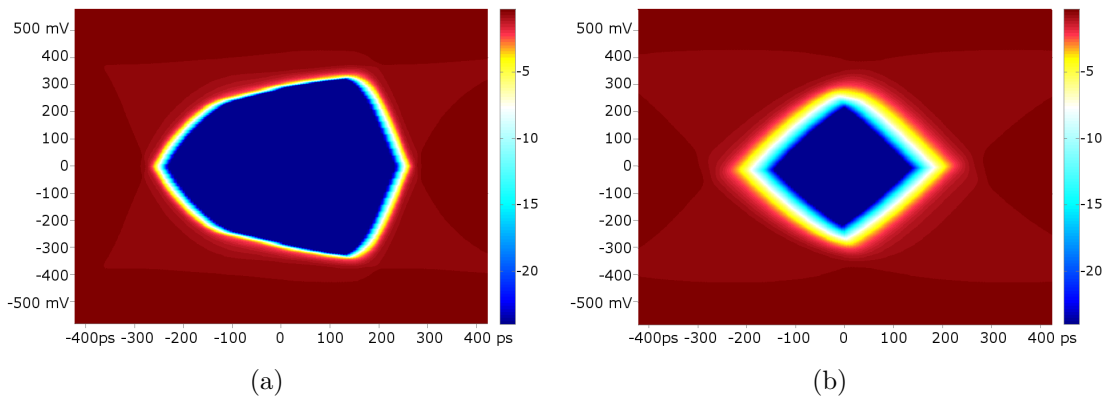


Figure 6.16: Comparison of the bit error rate eye diagrams of (a) wired and (b) 60 GHz wireless data transmission at 1.76 Gbps

Convoluting both bathtub curves the bit error rate eye is produced. For a wired and wireless data transmission the eye is shown in Figure 6.16(a) and (b) for 1.76 Gbps and in Figure 6.17(a) and (b) to 2.0 Gbps. The color code represents the logarithm of the bit

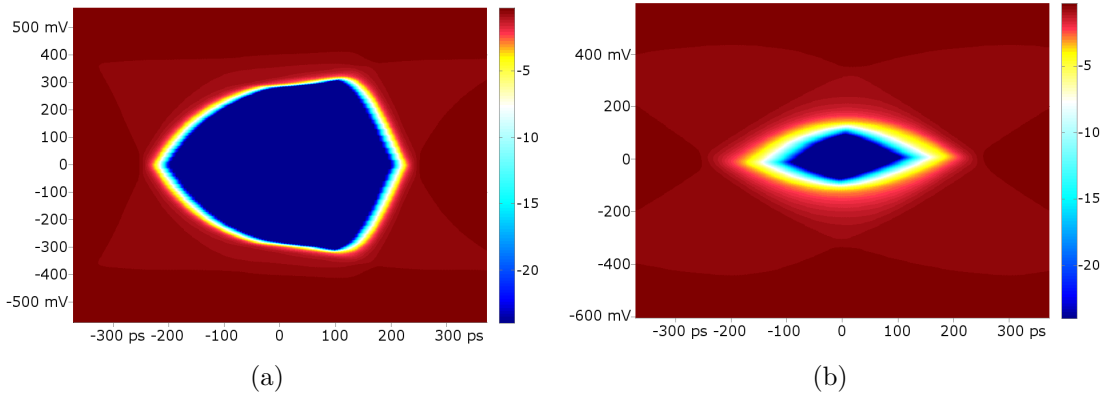


Figure 6.17: Comparison of the bit error rate eye diagrams of (a) wired and (b) 60 GHz wireless data transmission at 2.0 Gbps

error rate. This is a very commonly used representation of the quality of a serial data stream which directly connects the sampled signal to the bit error rate by representing the rate in the width and height of the eye. The wireless eye closes by increasing the data rate from 1.76 Gbps to 2.0 Gbps as the transceiver's bandwidth is limited to 1.8 GHz. In both cases the wireless eye looks more symmetric than the wired one because the bit transition's slope starts steeply and smooths out until it reaches the logic level in the wired transmission. To create the steep transition higher harmonics of the bit rates frequency are necessary which get filtered by the bandwidth limited transceiver. Therefore the rise and fall time are increased for the wireless data transfer. Considering the measured bit error rate at 2.0 Gbps of $6.2 \cdot 10^{-13}$ and assuming the decision time interval to be around $\pm 10\%$ of T_{bit} a minimum eye opening of about 150 ± 20 mV is necessary for a stable data transmission. Bit error rate eye parameters at different data rates are summarized in Table 6.4 to 6.7.

Data rate	TJ [ps]	Eye width [ps]	TJ [%UI]	Eye height [%UI]
BER	10^{-15}	10^{-15}	10^{-15}	10^{-15}
1.20 Gbps	77.7	755.7	9.3	90.7
1.50 Gbps	89.5	577.2	13.4	86.6
1.76 Gbps	79.5	488.7	14.0	86.0
2.00 Gbps	80.1	419.9	16.0	84.0
2.20 Gbps	82.5	372.0	18.1	81.9
2.40 Gbps	84.5	332.1	20.3	79.7

Table 6.4: Total Jitter and bit error rate eye width for a wired data transmission corresponding to a bit error rate of 10^{-15} .

Table 6.4 shows that the absolute total jitter at the same point of the bathtub curve corresponding to a bit error rate of 10^{-15} is independent of the data rate between 1.2 and 2.4 Gbps. The total noise instead is increasing around 50% which may be influenced by the fact that the 1 and 0 levels for single bit transitions are reduced compared to a

Data rate BER	TJ [ps] 10^{-15}	Eye width [ps] 10^{-15}	TJ [%UI] 10^{-15}	Eye width [%UI] 10^{-15}
1.20 Gbps	258.5	574.8	31.0	69.0
1.50 Gbps	263.7	403.0	39.5	60.5
1.76 Gbps	242.6	325.5	42.6	57.4
2.00 Gbps	245.8	254.3	49.2	50.8
2.20 Gbps	221.0	233.6	48.6	51.4
2.40 Gbps	263.7	153.0	63.3	36.7

Table 6.5: Total jitter and bit error rate eye width for a 60 GHz wireless data transmission corresponding to a bit error rate of 10^{-15} .

Data rate BER	TN [mV] 10^{-15}	Eye height [mV] 10^{-15}	TN [% V_{ppk}] 10^{-15}	Eye height [% V_{ppk}] 10^{-15}
1.20 Gbps	128.2	668.2	16.1	83.9
1.50 Gbps	154.9	620.0	20.0	80
1.76 Gbps	157.7	595.4	20.9	79.1
2.00 Gbps	159.5	578.4	21.6	78.4
2.20 Gbps	194.6	536.3	26.6	73.4
2.40 Gbps	170.5	552.9	23.6	76.4

Table 6.6: Total noise and bit error rate eye height for a wired data transmission corresponding to a bit error rate of 10^{-15} .

packet of consecutive 1s or 0s. Comparing the values of the wired transmission to the wireless one notes that the absolute total jitter is not varying much with the data rate as well. But its value is more than a factor of three larger. As the total jitter equals the width of the distribution up to the defined probability, and under the assumption that the jitter contribution from the FPGA and the wireless can be treated independently, a quadratic subtraction according to Equation 6.2 of the jitter measured using the wired data transfer from the wireless transmission yields the total jitter introduced by the wireless. These values together with the noise added by the wireless are comprised in Table 6.8.

$$\sigma_{TJ} = \sqrt{\sigma_{FPGA}^2 + \sigma_{Wireless}^2} \quad (6.2)$$

There is a trend visible in the total noise which is added by the wireless as the bandwidth of the transceiver is exceeded. The picked up noise increases by at least a factor of two. The total jitter however remains stable between 200 and 250 ps. The fact that the eye height at 1.76 Gbps is more than a factor of 2 larger than at all other data rates can be attributed to the baseband bandpass filters which provided the I and Q sinusoids with equal amplitude.

Comparing the eye parameters to the results of the bit error rate test, the small eye

Data rate BER	TN [mV] 10^{-15}	Eye height [mV] 10^{-15}	TN [% V_{pkpk}] 10^{-15}	Eye height [% V_{pkpk}] 10^{-15}
1.20 Gbps	224.2	139.6	31.0	19.3
1.50 Gbps	286.4	189.5	39.6	26.2
1.76 Gbps	237.0	486.1	32.8	67.2
2.00 Gbps	412.4	201.2	57.0	27.8
2.20 Gbps	460.4	139.3	63.7	19.3
2.40 Gbps	465.2	138.8	64.3	19.2

Table 6.7: Total noise and bit error rate eye height for a 60 GHz wireless data transmission corresponding to a bit error rate of 10^{-15} . Relative numbers do not add up to 100 % because the eye's top and bottom are not at the full peak to peak amplitude of the signal.

Data rate BER	Added TJ [ps] 10^{-15}	Added TN [mV] 10^{-15}
1.20 Gbps	246.2	183.9
1.50 Gbps	248.1	240.9
1.76 Gbps	229.2	176.9
2.00 Gbps	232.4	380.3
2.20 Gbps	205.0	417.3
2.40 Gbps	249.8	432.8

Table 6.8: Total Jitter and noise added by the 60 GHz wireless data transmission.

height at 1.2 Gbps seems to be a contradiction to the measured bit error rate smaller than 10^{-14} . But as the eye's width is much larger than for example at 2.0 Gbps the rise and fall times are relatively shorter compared to the eye's width. Therefore the eye's opening is still acceptable. A reason for the small eye opening may be the difference in the baseband signals' amplitudes as well as small phase uncertainties between I and Q. As all bits of the pattern are overlaid in the bit error eye diagram small amplitude offsets between the different bits which are introduced by an imperfect MSK modulation will also lead to a closing of the eye in vertical direction. This effect would also contribute to the total noise.

To draw a conclusion the MSK modulated 60 GHz wireless transmission over a 22 cm link with aluminised Kapton horn antennas adds about 235 ± 7 ps of jitter as well as 200 ± 20 mV of noise to the data stream operating in the limits of the system's bandwidth. A stable transmission is possible with bit error rates of the order of 10^{-15} .

6.3 Direct Crosstalk Measurements

The influence of direct crosstalk between two links, i.e. crosstalk induced by line of sight paths between the antennas, has been analysed using the setup similar to the one used in Section 5.3.1. This time with two complete wireless links operating at the same carrier frequency of 60 GHz and at the same polarisation. The distance between transmitters and receivers without horn antennas has been fixed to 10 cm. The setup is illustrated in Figure 6.18.

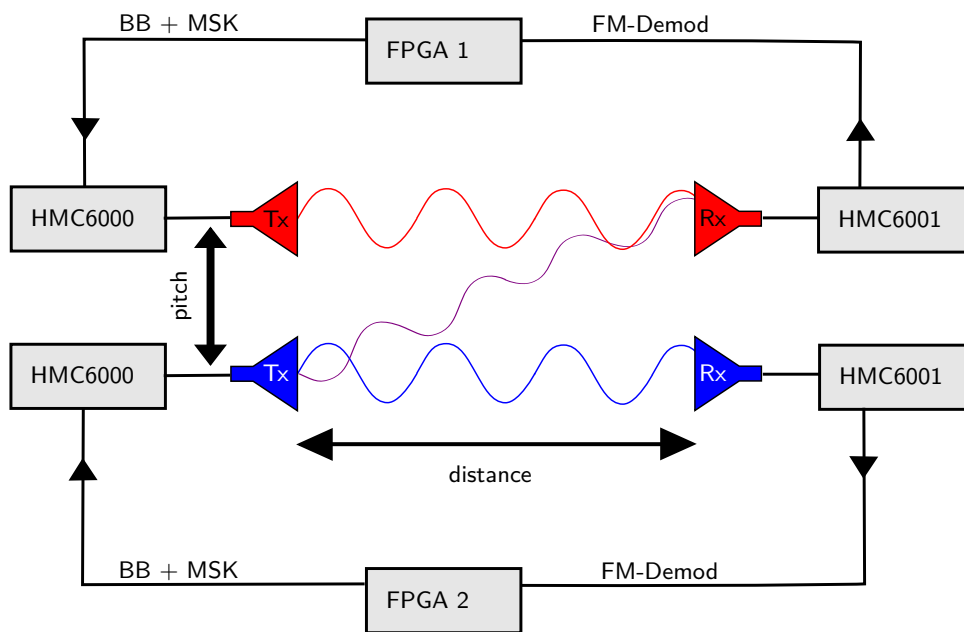


Figure 6.18: Setup for the bit error rate measurement with crosstalk

The pitch between the two links has been varied and four different settings have been tested: Kapton horn antennas applied to transmitter only, receiver only and both at the same time. Moreover 1 cm long hollow graphite cylinders have been under test. The usage of different wireless frequency channels has been investigated.

For the analysis the symbol errors detected by the 8b/10b decoder have been counted which yield the symbol errors in a reliable manner. In the case that not a single error occurred, an upper limit on the error rate is given. One of the links was operated at 1.76 Gbps, the other at 1.2 Gbps. In general, this should not induce differences in the error rates between the links as the individual links work properly at both rates.

6.3.1 Symbol Error Rates with Antennas and Foam

The results of the 8 b/10 b code error rate measurements with horn antennas are depicted in figures 6.19(a) to (c). The error rates measured in both links were different when horn antennas were mounted at the transmitter or receiver only. This may be

caused by differences in the transmitted power and the antennas' directivity.

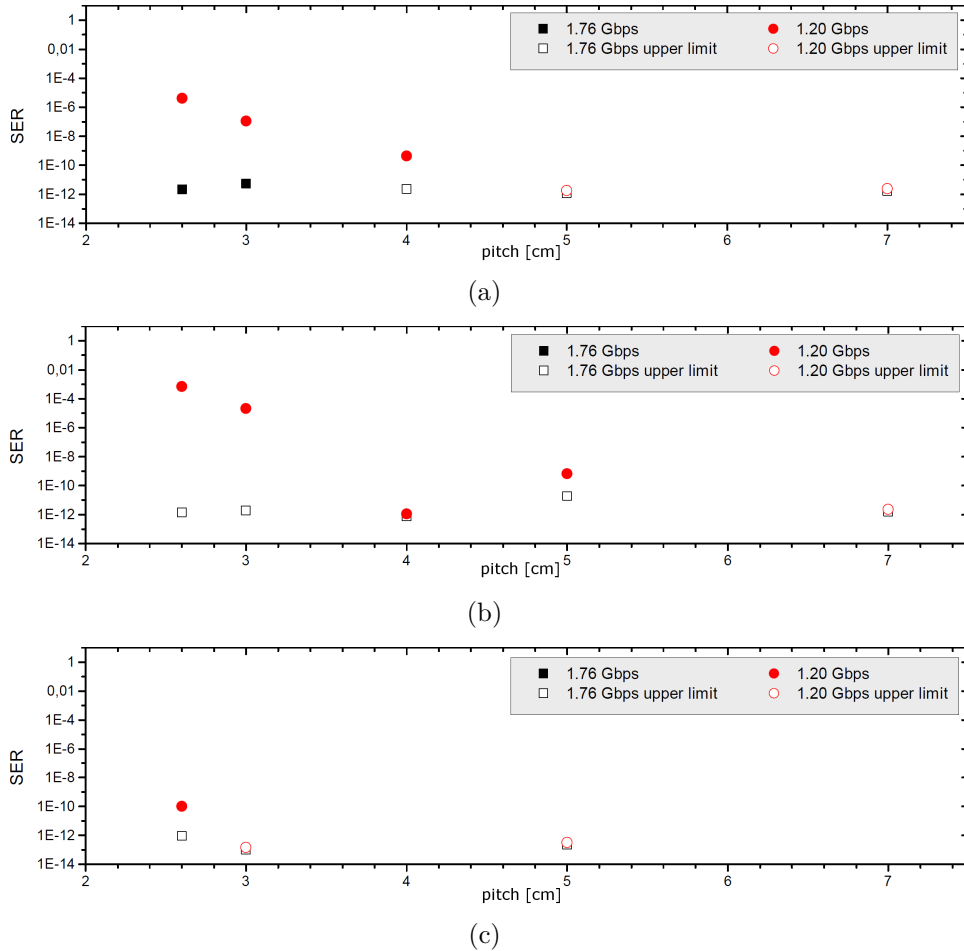


Figure 6.19: 8b/10b code error rates at different link pitches using horn antennas at (a) transmitters, (b) receivers and (c) both . Full coloured: measured symbol error rates if errors occurred. Contours: upper limit on symbol error rate as no error occurred during measurement.

At transmitters' distances above 5 cm not a single error was detected in any of the three configurations. Using horn antennas on both ends of the link, at the smallest possible pitch of 2.6 cm bit errors were detected in the 1.2 Gbps link, but the error rate was of the order of 10^{-10} . With horns applied to the transmitters only the error rate reached 10^{-5} in the same channel at this distance. With horns mounted on the receiver the error rate rose up to 10^{-3} . But the error rates drop quickly by increasing the pitch.

The same setup has been tested without directive antennas but with 1 cm long hollow graphite foam cylinders. The results are illustrated in Figure 6.20. Due to the fact that the signal to noise ratio drops much slower than with horn antennas the error rate drops until at a pitch of 10 cm a constant level is reached. In the 1.76 Gbps channel it reaches 10^{-12} , while the 1.2 Gbps channel stabilizes around 10^{-9} . This again may be influenced

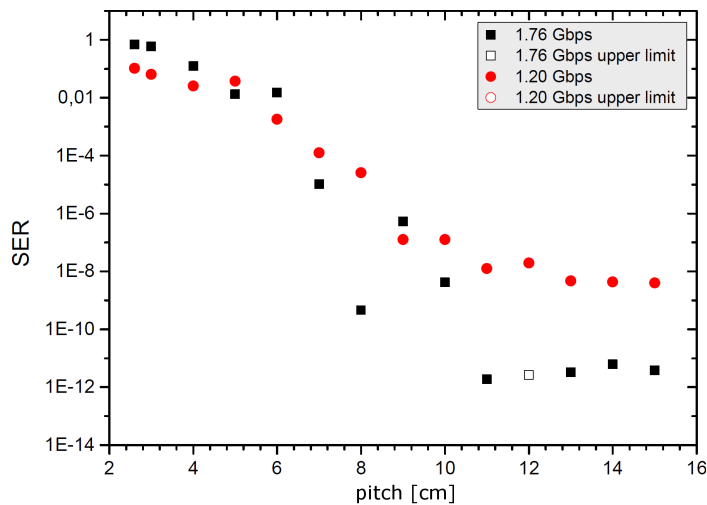


Figure 6.20: 8b/10b code error rates at different link pitches using foam shielding

by differences in the transmitted power. In addition, the foam cylinders lowered the transferred intensity up to 3 dB from the correct transmitter. Therefore the intensity at the receiver's input might have been too low to achieve lower bit error rates.

6.3.2 Symbol Error Rates with Channeling

For this measurement the pitch between the same two wireless links has been fixed to 2.6 cm. No directive antennas but only graphite foam shielding cylinders have been applied. Thus, the crosstalk between the two links was maximal. The carrier frequency of both transmitters was chosen to be 60 GHz first. Then, the 1.2 GHz link's carrier was shifted in steps of 500 MHz to 62 GHz which generates a carrier offset of up to 2 GHz. With 62 GHz for this link the carrier of the 1.76 Gbps link was reduced with the same step size down to 58 GHz to generate a total carrier difference of 4 GHz.

The measured symbol error rates versus the carrier difference are illustrated in Figure 6.21. One can clearly see the impact of the limited bandwidth of the receiver as the error rate drops steeply beyond an offset of 1.5 GHz. The 1.76 Gbps link reaches first a bit error rate lower than $1 \cdot 10^{-10}$ around 3 GHz carrier offset because of the smaller bandwidth which is occupied by the 1.2 Gbps link. The other way around a bit error rate of the order of 10^{-10} is therefore reached beyond 4.0 GHz carrier offset. This was expected as the bandwidth of the transceiver pair is ± 1.8 GHz which makes a carrier difference of more than 3.6 GHz necessary if the full bandwidth is used. The impact of the crosstalk can also be viewed nicely in the eye diagrams. Figures 6.22(a) to (c) shows the eye diagram of the 1.76 Gbps link at the output of the receiver while different carrier frequency offsets between the transmitters have been applied. Using the same carrier the eye is fully closed. With every 500 MHz step added to the carrier offset the eye opens more. At 4 GHz carrier offset no influence of the second link can be detected anymore.

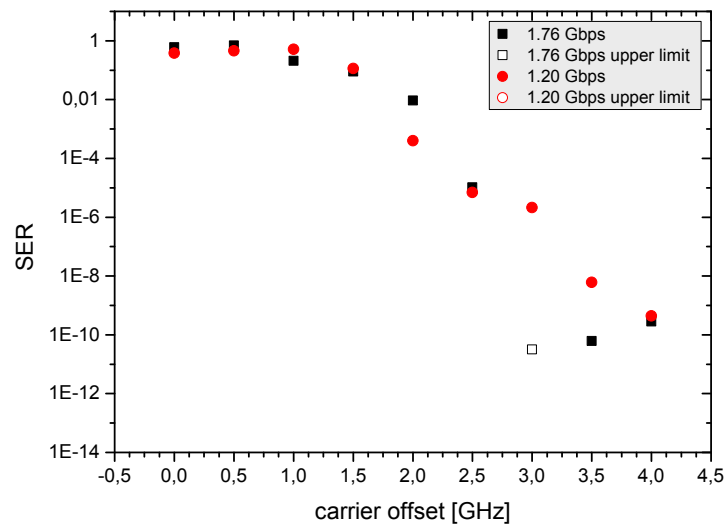


Figure 6.21: 8b/10b error rates of two cross-talking links using different frequency channels.

This measurement shows that even at high levels of crosstalk stable data transfer is possible if one can operate at different channels. But therefore one has to limit the intermediate frequency bandwidth of the transceiver and needs circuitry that allows for operating at different carrier frequencies. Limiting the bandwidth means that one has to use a more complex modulation scheme to transfer the same amount of data than with the full bandwidth at hand. A more complex modulation scheme also needs a more complex baseband circuitry. One has to take all of this into account and find a trade-off for a chip which finally can be used in the ATLAS tracker.

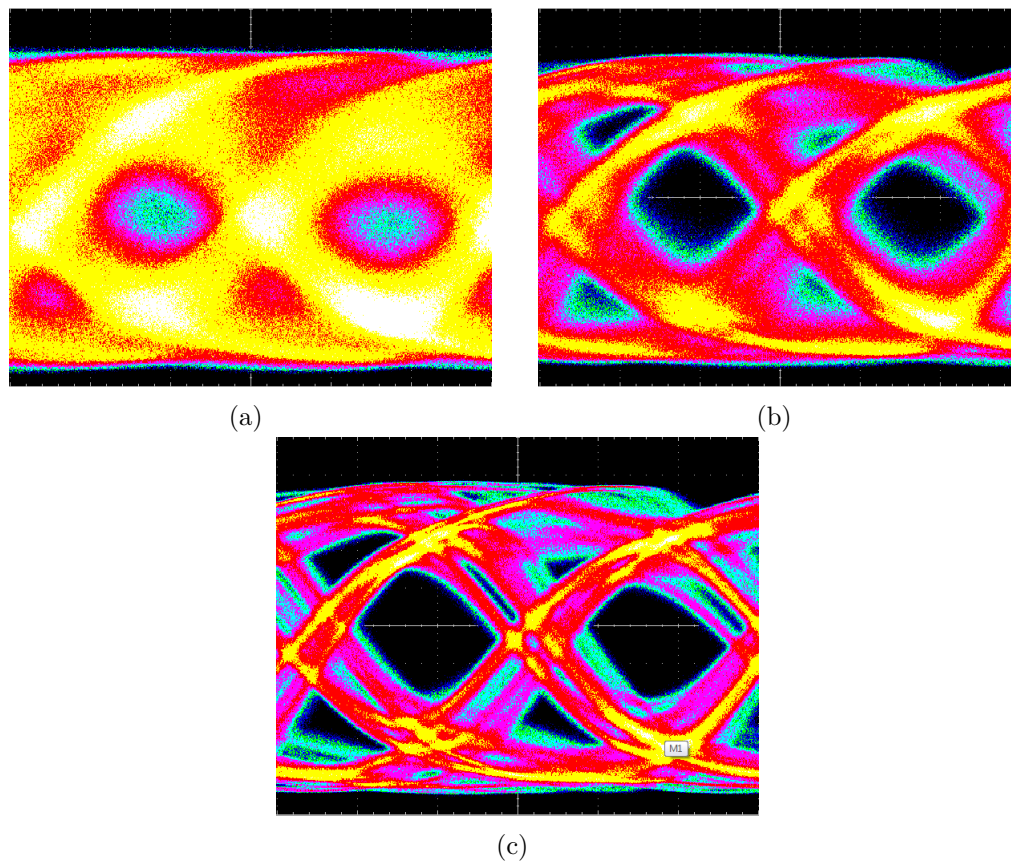


Figure 6.22: Eye diagrams of a 1.76 Gbps link with crosstalk at different channels. (a) Both links using the same carrier. (b) 2 GHz carrier difference (c) 4 GHz carrier difference

7 Discussion and Outlook

60 GHz wireless communication systems are a very promising candidate for many applications where high data rates are required. The scope of applications is very broad and ranges from wireless high definition video streaming to data kiosks all the way to multimedia systems in aircrafts. There is a lot of research in this sector going on which is boosted by the triumph of wireless communication systems during the last years.

For the High Luminosity LHC an upgrade of the ATLAS detector is demanded. The hardware trigger decision, which is currently based on calorimeter and muon spectrometer data, should include information of the tracking detector in the future to increase the trigger's selectivity. Therefore a new readout system is required which is capable of transferring several Gbps via individual links. The readout system with optical fibres that is currently used cannot handle these rates.

A wireless readout system operating at 60 GHz would allow to increase the readout bandwidth of the tracking detector. Thus, trigger decisions could be based on all hit information in the detector. This would require a total bandwidth of about 100 Tbps. About 30 000 links would be needed to transfer this amount of data assuming a possible data transfer rate of 3.5 Gbps per wireless link. Therefore the pitch between links would be of the order of a few centimetres. With directive antennas links can be placed in close proximity of each other. Using directional horn antennas with a beamwidth of about 20° parallel links can be operated at a pitch of 2 cm. The utilisation of linear polarised antennas allows for operation of neighbouring links with orthogonal polarisations which do not interfere with each other. It was found that orthogonal polarised waves can be suppressed by around 30 dB using horn antennas. Furthermore it was found that graphite foam can reduce reflections if it is mounted on the layers. Hence, a wireless readout of the ATLAS tracking detector seems feasible as crosstalk can be controlled. Besides, a wireless system would allow for a radial readout such that the transferred data follows the topology of relevant high- p_T events. This would simplify the implementation of track finding algorithms for trigger applications.

A new radiation hard 60 GHz wireless transceiver is currently under development which offers a maximum data rate of 3.5 Gbps by exploiting the full spectral bandwidth. In order to verify the correct operation and to detect weaknesses of the chip, a test bench has been built. It includes a bit error rate test to measure the quality of the wireless data transmission. It can be adapted easily to the new chip which uses On-Off-Keying (OOK) as modulation scheme. The transceiver under test did not offer OOK but Minimum Shift Keying (MSK), which is a slightly more complex but also non-coherent scheme. The developed bit error rate test worked properly at all tested data rates. Bit error rates of less than 10^{-14} could be measured using the full intermediate frequency bandwidth of

the Hittite transceiver at a rate of 1.76 Gbps. Up to 2.20 Gbps a data transfer with a bit error rate smaller than 10^{-8} was possible.

In addition a remote control software has been developed for the HAMEG HMP4040 power supplies. Supply voltages and bias currents applied to the chip can be monitored easily and their dependencies on external parameters can be analysed. This allows for comparisons to the simulated behaviour of the transceiver prototype. The power consumption of the chip can be determined as well.

This work has addressed the problem of crosstalk in a tracking detector using different approaches. Using highly directive antennas could solve the issue of crosstalk. This work pursued the idea of aluminised Kapton horn antennas from [34] by shrinking the dimensions of the antenna. The gain of the antenna is comparable to its larger predecessor whereas the beamwidth is measured to be higher. In a large frequency range it is still below 30° in both planes. Using even smaller dimensions would increase the beamwidth drastically as simulations have shown. As one would need a feed for these horn antennas anyway one might also think about a highly directive planar antenna. Crosstalk tests with the bit error rate test have been performed by applying 4.5 cm long horn antennas to links at a radio distance of 10 cm and it was found that stable communication is possible even at link pitches of only a few centimetre. Linear polarised waves offer the possibility to operate neighbouring links at orthogonal polarisations. The polarisation of different antennas has been tested in this work and it was found that the orthogonal component can be reduced by 30 dB and more. This would suffice to operate links in direct proximity even at the same carrier frequency. Moreover the operation of cross-talking transceivers at different channels has been tested. This requires a bandpass filter in the transceiver and a circuitry allowing to switch between the carrier frequencies. It was found that at very high levels of crosstalk communication is possible if operating at well separated frequency channels. Nevertheless, the trade-off in bandwidth will require more complexity in the baseband circuitry.

Graphite foam can be used to reduce reflections in the tracking detector. The reflectivity, transmittance and absorbance of graphite foam has been determined. It was found that three of four samples of graphite foam offer a high absorbance of more than 20 dB/cm, while the remaining one shows a significantly smaller reflectivity than the others. Graphite foam is therefore a material well suited for attenuating reflections and crosstalk if the antennas do not offer enough directivity. Other materials commonly used in detectors have been tested with respect to their properties of transmission and reflection. It was found that 50 μm of silicon are almost transparent to 60 GHz radiation. A 730 μm silicon wafer with test structures instead has a transmission loss of about 7 dB at small incident angles. It is strongly influenced by the orientation of the traces on the wafer which act like a polarising filter.

Tests have been conducted using hollow graphite foam cylinders to shield two links from each other. It was found that they yield a gain in the signal to noise ratio, even without directive antennas applied, though, the gain was considerably smaller than that of the antennas under test. Bit error rates have been measured using two links at the same

carrier frequency with this kind of shielding. At a wireless distance of 10 cm the foam cylinders allow for a stable transmission at low error rates at a pitch of 10 cm between the links without antennas.

The next steps on the way towards a wireless detector readout are to test the new transceiver chip and compare its functionality to the reference setup. Moreover, a small detector model could be set up which includes an implemented wireless data communication system. It would be interesting to see how some real detector piece with all its electronic components would behave regarding reflectivity and transmittance at different incident angles. Regarding antennas the production of small scale planar antennas from aluminised Kapton foil could be attempted. Both antennas and foam could be used in the detector model to investigate their benefit as well as their applicability.

Appendix A

BERT running on Stratix V FPGA

In the following the control signals and switches of the bit error rate test are explained. The FPGA is shown in Figure A.1 where the four controlling parts are highlighted.

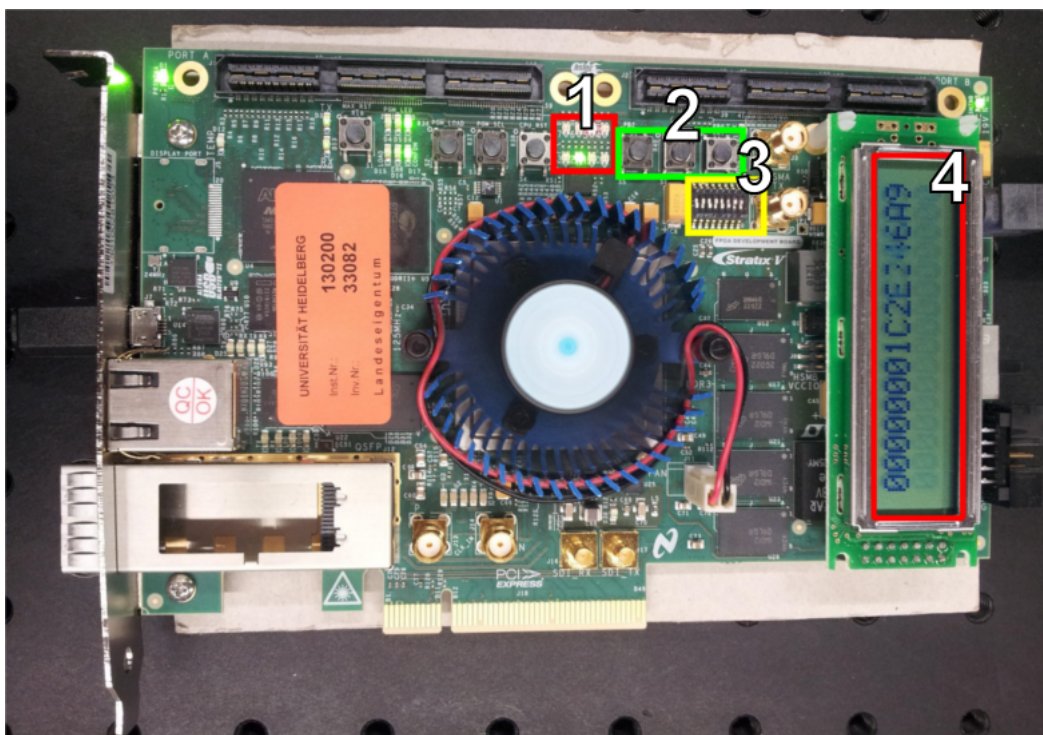


Figure A.1: Stratix V - LEDs, pushbuttons, dip switches and LCD for controlling and monitoring

1. LEDs: eight green and red LEDs display the status of the BERT. The states of the LEDs for correct operation of the BERT are summarised in Table A.1.
2. Pushbuttons: three pushbuttons are used for reset, error injection and pause of the LCD which is permanently updated otherwise.
3. Dip switches: eight dip switches are used to change settings of the firmware. Serial loopback can be activated or the MSK modulation module can be bypassed. The function of each switch is summarised in Table A.3. A detailed description is given in the following:

- DP 0: Serial loopback is for an internal loopback from the FPGA transmitter to the receiver for diagnostic purposes.
 - DP 1: Active alignment mode forces the transmitter to send the specified alignment pattern every 2^{18} clock cycles.
 - DP 2: Active PLL reset yields a reset of the whole FPGA logic including the PLLs.
 - DP 4: The MSK modulator can be bypassed with DP 4. This is used for wired transmission or can be used for On-Off-Keying.
 - DP 5: Square waves are used for diagnostics and phase alignment of the transmitter channels.
 - DP 6 & 7: Using DP 6 and DP 7 the following error counts can be displayed: '00': bit errors; '10': byte errors; '01': disparity errors; '11': 8b/10b code errors.
4. LCD: the 32-character LCD fulfills the following purpose:
The first line displays the transferred bytes, the second line the detected errors. Switching between byte errors, bit errors, 8b/10b code errors and disparity errors is possible via dip switches. The LCD is updated every clock cycle and can be paused by a pushbutton.

LED #	Signal green	running green	Signal red	running red
0	Tx PRBS [0]	1	N/C	-
1	Tx PRBS [1]	1	N/C	-
2	Tx PRBS [2]	0	Rx synchronised	1
3	Rx CHECKER [0]	1	Rx ready	1
4	Rx CHECKER [1]	1	N/C	-
5	Rx signal detected	1	N/C	-
6	Rx lock to reference	1	PLL locked	1
7	Rx lock to data	1	Rx pattern detected	1

Table A.1: Control LEDs (active low) and their state when operating correctly

PB #	Signal	Board ref.
0	error injection	S5
1	LCD pause	S6
2	reset	S7

Table A.2: Pushbuttons (active low = pushed) and their functions

DP #	Signal	Board ref.	MSK operation
0	serial loopback	SW1-1	off
1	alignment mode	SW1-2	on
2	PLL reset	SW1-3	off
3	N/C.	SW1-4	-
4	MSK bypass	SW1-5	off
5	square wave	SW1-6	off
6	error count	SW1-7	-
7	error count	SW1-8	-

Table A.3: Dip switches and their states for MSK operation

Appendix B

Monitoring of Power Supplies

The remote control software for the HAMEG HMP4040 power supplies from R&S was programmed with Microsoft Visual Studio for Windows and communicates with the power supply via a USB virtual COM-port. The graphical user interface is illustrated in Figure B.1. In the next paragraph the features of the software are explained.

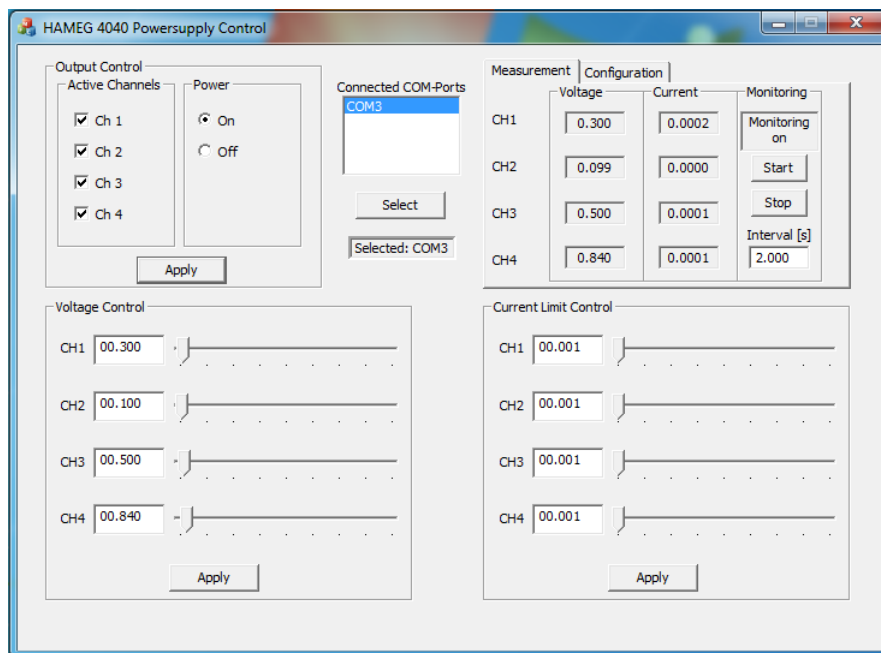


Figure B.1: GUI of HAMEG HMP4040 power supply control and monitor software

On the upper left the active channels can be selected and the output can be turned on or off. Settings are applied by clicking on the Apply-button.

In the upper middle the connected devices are listed. The device which is to be controlled can be selected in the list and is activated in the software by clicking on the Select-button. The currently selected device is displayed below. At start-up of the software all connected COM-ports are prompted and can be selected. It is possible to run several instances of the software at a time to create windows for each connected power supply or to control them all via a single window.

On the upper right the voltage and current of the individual channels of the selected power supply are displayed. One can start the monitoring which writes these values into a text file. The readout interval is shown below the start and stop buttons for the monitoring and can be modified. The readout is comparably fast, though if several devices are connected the interval should not be smaller than one second.

The second tab on the upper right (Configuration) allows for loading and saving a configuration file into the selected device.

In the lower left the voltage of the individual channels can be set either with the sliders or directly in the edit field. In the lower right the maximum current of the channels can be set analogously. The settings are adopted by clicking on the respective Apply-button.

Appendix C

Lists

C.1 List of Figures

2.1	Reflection, refraction and transmission at an interface of finite thickness. . .	6
2.2	p - and s -polarized waves	7
2.3	Polar pattern of an antenna. 3 dB beamwidth indicated.	9
2.4	E-plane and H-plane of a horn antenna	10
2.5	Principle of On-Off-Keying	12
2.6	IQ modulation	13
2.7	Principle of MSK modulation	13
3.1	A model of the ATLAS detector	15
3.2	The ATLAS inner detector	16
3.3	The unlicensed 60 GHz frequency band [30]	18
3.4	A radial readout facilitated by a wireless system operating at 60 GHz . . .	19
3.5	Block diagram of the transmitter chain	20
3.6	Block diagram of the receiver chain	20
4.1	Block diagram of the Gotmic transmitter and receiver	23
4.2	Gotmic transmitter and its bandwidth	24
4.3	Bias currents and RF output power of the Gotmic Tx	25
4.4	The Hittite HMC6451 60 GHz evaluation kit	26
4.5	Block diagram of the Hittite (a) transmitter and (b) receiver. Taken from the control software.	27
4.6	IF-bandwidth of the Hittite transceiver. (a) Radio frequency spectrum of the transmitter. (b) Baseband spectrum of the receiver.	28
4.7	Phase drift of the Hittite wireless link using baseband IQ-modulation . . .	28
5.1	Beamwidth for Gaussian intensity profiles	30
5.2	Intensity as function of the distance between transmitting and receiving horn antennas	32
5.3	Simulated radiation pattern of a 35.4 mm long horn antenna at $f = 60$ GHz	33
5.4	Simulated gain vs frequency of a 35.4 mm long horn antenna	33
5.5	Simulated beamwidth of horn antennas with different length in the (a) H-plane and (b) E-plane	34
5.6	Aluminised Kapton horn antenna and brass standard gain horn	34
5.7	Setup of directivity measurement	35
5.8	Polar patterns measured for horn and pad antennas	36

5.9	Gain of the pad antenna and the Kapton horn antennas	37
5.10	Beamwidth measurements of the (a) Kapton horn antennas and (b) pad antenna	37
5.11	Polarisation measurement's setup	38
5.12	Polarising filter and the setup in the lab	39
5.13	Polarisation measurement: rotating antenna	40
5.14	Polarisation measurement: rotating polarising filter	41
5.15	Setup for reflectivity and transmittance measurement of a sample	42
5.16	Setup in the laboratory: graphite foam sample between horn antennas	43
5.17	Baseline and reference measurement for transmission and reflection	44
5.18	Samples for reflectivity and transmittance measurements: (a) 25 μm Kapton foil with 50 nm aluminum, (b) 730 μm silicon wafer with test structures, and (c) 50 μm silicon.	45
5.19	Reflection and transmission loss of aluminised Kapton foil and 50 μm silicon	46
5.20	Orientations of the silicon wafer according to the measurements	47
5.21	Reflection and transmission loss of a 730 μm silicon wafer with test structures	48
5.22	Reflection loss of four types of graphite foam	49
5.23	Transmission loss of four types of graphite foam	50
5.24	Reflection loss by graphite foam stucked onto an aluminum plate	51
5.25	Frequency dependence of the index of refraction and absorption loss of graphite foam	52
5.26	Setup for the measurement of insertion loss of graphite foam	53
5.27	Insertion loss versus frequency of the tested foams derived from fit functions.	53
5.28	Crosstalk measurement setup #1: measuring signal to noise ratio by displacing the transmitter perpendicular to the direct line of transmission.	55
5.29	Signal to noise ratio by displacing transmitter	56
5.30	Crosstalk measurement setup #2: Two links between aluminum boards.	57
5.31	Setup for signal to noise measurement with reflections in the laboratory	58
5.32	500 MHz double sideband signals of two links	58
5.33	S/N between aluminum layers using horn antennas	59
5.34	S/N between aluminum layers using horn antennas	60
5.35	Crosstalk measurement setup #3: S/N at RX input and output.	61
5.36	Radio frequency (RF) and baseband (BB) signal to noise comparison	62
5.37	Signal to noise at receiver output vs input	62
6.1	Modules of the bit error rate test: Transmitter	66
6.2	LFSR for PRBS8	66
6.3	Standard PCS data path of Stratix V Transceiver Native PHY IP core	67
6.4	Modules of the bit error rate test: Receiver	68
6.5	Connection of FPGA and 60 GHz transceiver.	69
6.6	Phase relations between I and Q signals.	70
6.7	(a) Setup of the 60 GHz wireless data transmission in the laboratory. (b) Spectrum of the MSK modulated signal in the 60 GHz-band.	71
6.8	Generating an eye diagram	73
6.9	Measureable quantities of an eye diagram	73
6.10	Setup for eye diagram measurements	74

6.11	Eye diagrams at 1.76 Gbps	75
6.12	Eye diagrams at 2.00 Gbps	75
6.13	Probability density functions for jitter comparing wired and wireless data transfer	77
6.14	Total jitter in dependence of the bit error rate	78
6.15	Horizontal and vertical bathtub curves	79
6.16	Eye diagrams at 1.76 Gbps	79
6.17	Eye diagrams at 2.0 Gbps	80
6.18	Setup for the bit error rate measurement with crosstalk	83
6.19	8b/10b code error rates at different link pitches using horn antennas . . .	84
6.20	8b/10b code error rates at different link pitches using foam shielding . . .	85
6.21	8b/10b code error rates of two neighbouring links with channeling	86
6.22	Eye diagrams of a 1.76 Gbps link with crosstalk at different channels . . .	87
A.1	Stratix V - LEDs, pushbuttons, dip switches and LCD for controlling and monitoring	93
B.1	GUI of HAMEG HMP4040 power supply control and monitor software . . .	97

C.2 List of Tables

2.1	Summary of modulation schemes	14
5.1	Simulated gain of ideal horn antennas with different length	34
5.2	Intensity suppression by rotation of antennas	40
5.3	Intensity suppression with the help of polarising filter	41
5.4	Properties of graphite foams under test	42
5.5	Index of refraction of the 50 μm silicon wafer	46
5.6	Index of refraction of the 730 μm silicon wafer with test structures	47
5.7	Index of refraction and absorption loss per centimetre for four types of graphite foam	49
5.8	Insertion loss of graphite foam	54
5.9	Inhomogeneity of graphite foam regarding insertion loss	54
5.10	Carrier, sideband radio frequencies (RF) and baseband (BB) frequencies of signal (Tx 1) and noise (Tx 2)	61
6.1	Bit error rates of 60 GHz transmission	72
6.2	Eye diagram parameters: width	76
6.3	Eye diagram parameters: height	76
6.4	Jitter and bit error rate eye diagram parameters: wired	80
6.5	Jitter and bit error rate eye diagram parameters: wireless	81
6.6	Noise and bit error rate eye diagram parameters: wired	81
6.7	Noise and bit error rate eye diagram parameters: wireless	82
6.8	Jitter and noise added by the 60 GHz wireless	82
A.1	Control LEDs (active low) and their state when operating correctly	95
A.2	Pushbuttons (active low = pushed) and their functions	95
A.3	Dip switches and their states for MSK operation	95

Bibliography

- [1] ATLAS Experiment. *Trigger System*. 12/2012. URL: <http://www.atlas.ch/trigger.html> (visited on 11/04/2013).
- [2] ATLAS Experiment. *ATLAS Fact Sheet*. URL: http://www.atlas.ch/pdf/atlas_factsheet_all.pdf.
- [3] ATLAS Collaboration CERN. *The Performance of the ATLAS Detector*. Springer, 2011.
- [4] HL-LHC: High Luminosity Large Hadron Collider. *The HL-LHC project*. 12/2012. URL: <http://hilumilhc.web.cern.ch/HiLumiLHC/about/> (visited on 11/04/2013).
- [5] ATLAS Collaboration CERN. *Letter of Intent for the Phase-II Upgrade of the ATLAS Experiment*. Draft version for comments. 12/2012.
- [6] Duixian Liu et al. *Advanced Millimeter-wave Technologies: Antennas, Packaging and Circuits*. Wiley, 2009.
- [7] R.Brenner and S.Cheng. “Multigigabit wireless transfer of trigger data through millimetre wave technology”. In: *2010 JINST 5 c07002* (07/20/2010). DOI: [10.1088/1748-0221/5/07/C07002](https://doi.org/10.1088/1748-0221/5/07/C07002).
- [8] H.K. Soltveit et al. “Multi-Gigabit Wireless data transfer at 60 GHz”. In: *2012 JINST 7 C12016* (12/2012). DOI: [10.1088/1748-0221/7/12/C12016](https://doi.org/10.1088/1748-0221/7/12/C12016).
- [9] John David Jackson. *Classical Electrodynamics*. 3rd edition. Wiley, 1999.
- [10] Wolfgang Demtröder. *Experimentalphysik 2 - Elektrizität und Optik*. 3. Auflage. Springer Verlag, 2004.
- [11] Wikipedia. *Fresnelsche Formeln*. 04/21/2013. URL: http://de.wikipedia.org/wiki/Fresnelsche_Formeln (visited on 09/18/2013).
- [12] Jürgen Detlefsen and Uwe Siart. *Grundlagen der Hochfrequenztechnik*. 3. Auflage. Oldenburg, 2009.
- [13] Peter Joseph Bevelacqua. *Antenna Theory: Beamwidths and Sidelobes*. URL: <http://www.antenna-theory.com/basics/radPatDefs.php> (visited on 11/04/2013).
- [14] Wikipedia. *Beamwidth*. 09/10/2013. URL: <http://en.wikipedia.org/wiki/Beamwidth> (visited on 11/16/2013).
- [15] K.A.Bakshi, A.V.Bakshi, and U.A.Bakshi. *Antennas And Wave Propagation*. Technical Publications, 2009.
- [16] Wikipedia. *Decibel*. 11/03/2013. URL: <http://en.wikipedia.org/wiki/Decibel> (visited on 11/04/2013).
- [17] Wikipedia. *Baseband*. 10/20/2013. URL: <http://en.wikipedia.org/wiki/Baseband> (visited on 11/16/2013).

- [18] Wikipedia. *Passband*. 09/15/2013. URL: <http://en.wikipedia.org/wiki/Passband> (visited on 11/16/2013).
- [19] Fachhochschule Giessen - Fachbereich E II - Labor für Telekommunikation. *Digital Modulationsverfahren*. 1999.
- [20] Maxim Integrated. *I'm OOK. You're OOK?* Application Note 4439. 04/08/2009. URL: <http://www.maximintegrated.com/app-notes/index.mvp/id/4439>.
- [21] Wikipedia. *Quadraturamplitudenmodulation*. 05/11/2013. URL: <http://de.wikipedia.org/wiki/Quadraturamplitudenmodulation> (visited on 11/07/2013).
- [22] Bosco Leung. *VLSI for Wireless Communication*. 2nd edition. Springer, 2011.
- [23] Hittite Microwave Corporation. *MSK Modulation using HMC6000/HMC6001*. Application Note. 2012.
- [24] ATLAS Collaboration. "Observation of a new particle in the search for the Standard Model Higgs boson with the ATLAS detector at the LHC". In: 716.1 (2012), pp. 1–29. ISSN: 0370-2693. DOI: <http://dx.doi.org/10.1016/j.physletb.2012.08.020>. URL: <http://www.sciencedirect.com/science/article/pii/S037026931200857X>.
- [25] CMS Collaboration. "Observation of a new boson at a mass of 125 GeV with the CMS experiment at the LHC". In: 716.1 (2012), pp. 30–61. ISSN: 0370-2693. DOI: <http://dx.doi.org/10.1016/j.physletb.2012.08.021>. URL: <http://www.sciencedirect.com/science/article/pii/S0370269312008581>.
- [26] ATLAS Experiment. *Photos*. 2013. URL: <http://www.atlas.ch/photos/index.html> (visited on 11/05/2013).
- [27] ATLAS Experiment. *Detector Description*. 2013. URL: <http://www.atlas.ch/detector.html> (visited on 11/05/2013).
- [28] E. Lipeles. "L1 track triggers for ATLAS in the HL-LHC". In: *2012 JINST 7 C01087* (2012). DOI: [10.1088/1748-0221/7/01/C01087](https://doi.org/10.1088/1748-0221/7/01/C01087).
- [29] L Rossi and O Brüning. *High Luminosity Large Hadron Collider A description for the European Strategy Preparatory Group*. 08/2012.
- [30] Bob Daniels. *60 GHz Wireless Communication*. 03/13/2008. URL: <http://windowsil.org/category/wsil-publications/> (visited on 11/05/2013).
- [31] S.K. Yong, P. Xia, and A. Valdes-Garcia. *60GHz Technology for Gbps WLAN and WPAN: From Theory to Practice*. Wiley, 2011. ISBN: 9781119956747. URL: <http://books.google.de/books?id=17P6F27HR1kC>.
- [32] Mark Stevens and Grant Grafton for Sub10Systems. *The Benefits of 60 GHz Unlicensed Wireless Communications*. White Paper. URL: <http://www.sub10systems.com/wp-content/uploads/2011/03/White-Paper-Benefits-of-60GHz.pdf>.
- [33] H.K. Soltveit et al. *Multi-Gigabit Wireless data transfer at 60 GHz*. Talk at Workshop on Intelligent Trackers (WIT) 2012. 05/04/2012.
- [34] Jens Petersen. "Performance Analysis of a Transceiver Chipset and Interference Control for a Wireless Detector Readout at 60 GHz". BSc thesis. 04/2013.

- [35] Thomas Hügler. "Simulation von Datenübertragung und Beugung mit einem Ray-tracer". BSc thesis. 02/2013.
- [36] IBM Systems and Technology. *IBM SiGe BiCMOS 8HP*. 2012. URL: <http://public.dhe.ibm.com/common/ssi/ecm/en/tgd03022usen/TGD03022USEN.PDF>.
- [37] Wikipedia. *Heterojunction bipolar transistor*. 04/21/2013. URL: http://en.wikipedia.org/wiki/Heterojunction_bipolar_transistor (visited on 11/06/2013).
- [38] Wikipedia. *BiCMOS*. 05/20/2013. URL: <http://en.wikipedia.org/wiki/BiCMOS> (visited on 11/06/2013).
- [39] M. Ullan et al. *Evaluation of Two SiGe HBT Technologies for the ATLAS sLHC Upgrade*. TWEPP 2008.
- [40] Gotmic. *TXQ0A0601 60 GHz Transmitter*. Data sheet.
- [41] Gotmic. *RXQ0A0601 60 GHz Receiver*. Data sheet.
- [42] Telemeter Electronic. *Microwave Absorbing Materials*. URL: http://www.telemeter.info/documents/absorbing_materials.pdf (visited on 10/24/2013).
- [43] Y. Unno. "ATLAS silicon microstrip detector system (SCT)". In: *Nuclear Instruments and Methods in Physics Research A 511 (2003) 58–63* (2003). DOI: 10.1016/S0168-9002(03)01751-0.
- [44] S. Cheng et al. "79 GHz Slot Antennas Based on Substrate Integrated Waveguides (SIW) in a Flexible Printed Circuit Board". In: *IEEE Transactions on Antennas and Propagation* 57.1 (01/01/2009).
- [45] J. Säily, A. Lamminen, and J. Francey. *Low cost high gain antenna arrays for 60 GHz millimetre wave identification (MMID)*. URL: http://www.taconic-add.com/pdf/technicalarticles--high_gain_antenna_mmids.pdf.
- [46] Wikipedia. *Near and far field*. 10/18/2013. URL: http://en.wikipedia.org/wiki/Near_and_far_field (visited on 10/22/2013).
- [47] Eugene Hecht. *Optik*. 5. Auflage. Oldenbourg Verlag München, 2009.
- [48] PDG. *Atomic and Nuclear Properties*. 2013. URL: <http://pdg.lbl.gov/2012/AtomicNuclearProperties/> (visited on 10/24/2013).
- [49] A. Schöning et al. *Research Proposal for an Experiment to Search for the Decay $\mu \rightarrow eee$* . 12/2012.
- [50] Hittite Microwave Corporation. *HMC6001 Millimeterwave Receiver IC*. Data sheet.
- [51] Altera. *On-chip Debugging Design Examples*. URL: <http://www.altera.com/support/examples/on-chip-debugging/on-chip-debugging.html> (visited on 09/25/2013).
- [52] Wikipedia. *VHDL*. 09/10/2013. URL: <http://en.wikipedia.org/wiki/VHDL> (visited on 09/25/2013).
- [53] Altera. *Stratix V DSP Development Kit*. URL: http://www.altera.com/products/devkits/altera/kit-stratix-v-dsp.html?GSA_pos=1%5C&WT.oss%5C_r=1%5C&WT.oss=v%20gs (visited on 09/25/2013).
- [54] Peter Alfke for Xilinx. *Efficient Shift Registers, LFSR Counters, and Long Pseudo-Random Sequence Generators - XAPP 052*. Version 1.1. 07/07/1996.

- [55] Wikipedia. *Linear feedback shift register*. 09/02/2013. URL: http://en.wikipedia.org/wiki/Linear_feedback_shift_register (visited on 09/25/2013).
- [56] A. X. Widmer and P. A. Franaszek. "A DC-Balanced, Partitioned-Block, 8B/10B Transmission Code". In: *IBM Journal of research and development* 27 (09/05/1983).
- [57] Altera. *Altera Transceiver PHY IP Core User Guide*. UG-01080. 2013.
- [58] Altera. *The Evolution of High-Speed Transceiver Technology*. White Paper. URL: http://www.altera.com/literature/wp/wp_hs_transceiver.pdf.
- [59] ON Semiconductor. *Understanding Data Eye Diagram Methodology for Analyzing High Speed Digital Signals*. Application Note. AND9075/D.
- [60] Tektronix. *80SJNB - Jitter, Noise, BER and Serial Data Link Analysis Software*. Printable Online Help.
- [61] Fabrizio Lombardi Kyung Ki Kim Yong-BinKim. *Data Dependent Jitter (DDJ) Characterization Methodology*. URL: http://www.ece.neu.edu/faculty/ybk/publication/DATA_DEPENDENT_JITTER_DFT05.pdf.
- [62] Pavel Zivny for Tektronix Inc. *Tektronix CSA/TDS8200 Jitter Analysis Application: Jitter and Noise Analysis, BER Estimation Descriptions*. White Paper.

Acknowledgements

An dieser Stelle möchte ich mich bei allen bedanken, die mich beim Erstellen dieser Arbeit sowie während meines Studiums unterstützt haben.

Zuerst möchte ich mich bei Prof. André Schöning bedanken, der mir die Möglichkeit gegeben hat, an diesem spannenden Projekt teilzunehmen und mich in dieser Zeit hervorragend betreut hat.

Außerdem möchte ich mich bei Prof. Norbert Herrmann dafür bedanken, dass er sich bereit erklärt hat, die Zweitkorrektur dieser Arbeit zu übernehmen.

Für die glänzende Betreuung und Unterstützung während der Anfertigung dieser Arbeit möchte ich mich besonders bei Dr. Dirk Wiedner bedanken.

Außerdem danke ich Dr. Niklaus Berger und Hans Kristian Soltveit für die vielen hilfreichen Gespräche.

Weiterhin gilt mein Dank der gesamten Arbeitsgruppe für die tolle Arbeitsatmosphäre. Außerdem möchte ich Christian Färber dafür danken, dass ich von ihm viel über FPGA-Designs lernen konnte.

Auch bei den Kollegen des Heinrich-Hertz-Instituts in Berlin unter der Leitung von Dr. Wilhelm Keusgen möchte ich mich für die Kooperation bedanken.

Zuletzt möchte ich mich bei Tanja Ronalter, meiner Familie und meinen Freunden für ihre Unterstützung bedanken. Ohne sie wäre diese Arbeit nicht möglich gewesen.

Erklärung:

Ich versichere, dass ich diese Arbeit selbstständig verfasst habe und keine anderen als die angegebenen Quellen und Hilfsmittel benutzt habe.

Heidelberg, den 18.11.2013

.....